

THE APPLICATION OF INSTABILITY WAVE THEORY ON ACOUSTIC RADIATION
WITHIN OFF-DESIGN SUPERSONIC JETS AND ON TWO-POINT STATISTICS WITHIN
HIGH-SPEED FLOW OVER SHARP AND BLUNT CONES WITH PLASMA ACTUATION

By

JIANHUI CHENG

A DISSERTATION PRESENTED TO THE GRADUATE SCHOOL
OF THE UNIVERSITY OF FLORIDA IN PARTIAL FULFILLMENT
OF THE REQUIREMENTS FOR THE DEGREE OF
DOCTOR OF PHILOSOPHY

UNIVERSITY OF FLORIDA

2022

© 2022 Jianhui Cheng

To my family who are always supportive in my life

ACKNOWLEDGEMENTS

First of all, I want to express my gratitude to my parents and other family members for their continuous supports throughout my life.

I am grateful to my advisor, Dr. Steven A. E. Miller. He gave me a lot of directions and encouragements from the determination of the research topics to the final dissertation defense. During this process, I learned how to plan and conduct research. My writing and presentation skills are also improved with your help on revising each manuscript and presentation. I also would like to thank Dr. Sivaramakrishnan Balachandar, Dr. Lawrence Ukeiley, and Dr. Nan Jiang for serving as my committee members and their insightful comments.

I also would like to thank my colleagues: Alex Carr, Trushant Patel, Weiqi Shen, Wei Wang, and Tianshu Zhang. Their assistance and suggestions helped me overcome many problems encountered in my research and courses. It was an enjoyable experience working with them. I am also grateful for the assistance I received from James Goldschmidt in the joint SERDP program.

Finally, I am always grateful for the continuous funding from Strategic Environmental Research and Development Program (SERDP) WP19-1014: Flow control of large-scale turbulence to reduce jet noise and Space Research Initiative (SRI) OR-DRPD-SRI2020: Reduction of Rocket Vibrations via Control of Large-Scale Coherent Turbulent Structures.

TABLE OF CONTENTS

	<u>page</u>
ACKNOWLEDGEMENTS	4
LIST OF TABLES	7
LIST OF FIGURES	11
ABSTRACT	12
CHAPTER	
1 INTRODUCTION	14
1.1 Motivation and Background	14
1.2 Objective and Scope of Proposed Work	18
1.3 Flow Structures	18
1.3.1 Free Jets	19
1.3.2 Boundary Layer Flows	20
1.3.3 Coherent Motions	21
1.4 Supersonic Jet Noise	23
1.4.1 Characteristics of Jet Noise	23
1.4.2 Prediction of Jet Noise with Acoustic Analogy	26
1.4.3 Instability Wave Models within Jet Flows	29
1.4.4 Wave-Packet Method	35
1.5 Stability Analysis of Boundary Layer Flows	36
1.5.1 Stability Modes	36
1.5.2 Cross-Power Spectral Density of Pressure Fluctuations	41
1.6 Flow Control via Plasma Actuators	43
1.7 Structure of the Dissertation	46
1.7.1 Chapter 2: Methodology	46
1.7.2 Chapter 3: Jet Noise Prediction and Discussion	46
1.7.3 Chapter 4: Cone Flow and Stability Calculations of Boundary Layers	46
1.7.4 Chapter 5: Summary and Conclusion	47
2 METHODOLOGY	48
2.1 Methodology for Jet Flows	48
2.1.1 Instability Wave Theory	48
2.1.2 Detection of Instability Waves	59
2.1.3 Kirchhoff Surface Method	64
2.1.4 Correlation and Coherence	66
2.2 Methodology for Boundary Layer Flows	67
2.2.1 Linear Stability Theory	67
2.2.2 Cross-Power Spectral Density of Pressure from Instability Waves	72
2.2.3 Phenomenological Model of Plasma Actuators	73
3 JET NOISE PREDICTION AND DISCUSSION	74
3.1 Results of SHJAR Case	74
3.1.1 Flow-Field Analysis	74

3.1.2	Instability Wave Detection	77
3.1.3	Far-Field Sound	88
3.1.4	Correlation and Coherence Analysis.....	92
3.2	Results of SERDP Case	97
3.2.1	Flow-Field Analysis	97
3.2.2	Stability Analysis	98
3.2.3	Far-Field Noise Prediction	99
3.2.4	Correlation and Coherence Analysis.....	104
4	CONE FLOWS AND STABILITY CALCULATIONS OF BOUNDARY LAYERS	109
4.1	Base Flow-Fields Computation and Validation.....	109
4.1.1	Mean Flow-Field Computation and Validation	109
4.1.2	Stability Computation and Validation.....	115
4.1.3	Spatial Coherence	117
4.2	The Effects of Plasma Actuator Model	122
4.2.1	Validation and Flow Structures	122
4.2.2	Cone Flows with plasma actuator	124
5	SUMMARY AND FUTURE WORK	136
5.1	Summary of Results	136
5.1.1	Jet Flows	136
5.1.2	Boundary Layer Flows	137
5.2	Future Work	140
5.2.1	Jet Flows	140
5.2.2	Boundary Layer Flows	140
	REFERENCES	142
	BIOGRAPHICAL SKETCH	155

LIST OF TABLES

<u>Tables</u>	<u>page</u>
4-1 Flow conditions.....	111
4-2 Stability Parameters.....	115
4-3 Peak position of maximum growth rates of each case (m).....	116
5-1 Operating Conditions.....	136
5-2 Frequency range (ω^*) with high spatial coherence (kHz) of base flow.	139
5-3 Frequency range (ω^*) with high spatial coherence (kHz) of actuated flow.	139

LIST OF FIGURES

<u>Figures</u>	<u>page</u>
1-1 Aircraft noise reduction trends.....	15
1-2 Free jet flow structure.	19
1-3 Turbulent boundary layer flow structure.	21
1-4 A temporal phase of the evolution of typical eddies, where the pocket and primary hair-pin vortex are formed.....	22
1-5 Three components of an under-expanded supersonic jet noise at various radiation angles, $M_d = 1$, $M_j = 1.5$, and TTR=1.00, data from NASA Glenn Research Center courtesy of Miller.....	24
1-6 Acoustic power measurements for two heated jets at $M_j = 0.5$ and 1.5, TTR=2.7, azimuthal mode $m = 0$, and frequency $St = 0.25$	25
1-7 Wave patterns of three sets of instability waves, Kelvin-Helmholtz, supersonic, and subsonic instability waves from top to bottom.	31
1-8 The flow regions of a round jet in the radial direction. The solid line depicts the time-averaged pressure fluctuation of $m = 0$ at $x/D = 4$ from DNS, and the dotted line denotes the corresponding eigenfunction calculated from a LST.	34
1-9 The distribution of growth rates and phase speeds of different stability modes with frequency at $M_\infty = 7.99$	37
1-10 The transition positions at different M_e based on the results of flight test.	39
1-11 Effect of wall cooling on the maximum spatial growth rates of the first (dashed lines) and second (solid lines) modes along M_a for $Re = 1500$, $T_w^* = 300$ K, $T_e^* = 70 - 2000$ K, $p_e^* = 10$ kPa.	41
1-12 The contours of Joule heating distribution of flat-plate flow with a DBD plasma actuator and effects of plasma actuators on a flat-plate flow.	44
2-1 Jet flow region.	50
2-2 Box path of the contour mapping.....	58
2-3 Kirchhoff surface location.	65
2-4 Body-fitted orthogonal curvilinear coordinates.....	68
3-1 Axisymmetric view of SMC000 nozzle geometry with units in mm.	74
3-2 Comparison of mean axial velocity distribution between the LES and RANS simulation on the centerline.....	75
3-3 Instantaneous pressure contour ($p - p_\infty$) in Pa.	75
3-4 Frequency spectra of modal pressure perturbations of LES data at several axial positions in the jet shear layer at $r/D = 0.5$	76

3-5	Variation of the streamwise velocity component and density in the radial direction at different axial locations from the LES.	77
3-6	Variation of phase speed and growth rate of different azimuthal modes at $x/D = 2.5$	78
3-7	The development of phase speed and growth rate of different azimuthal modes along the streamwise direction at $St = 0.2006$	79
3-8	Comparisons of pressure and axial velocity eigenfunctions for $m = 0$ between prediction (dash line) and LES (solid line).	80
3-9	Comparisons of pressure and axial velocity eigenfunctions for $m = 1$ between prediction (dash line) and LES (solid line).	80
3-10	Comparisons of eigenfunctions of pressure perturbations between LES and prediction at $St = 0.1506$ for different azimuthal modes at $x/D = 2.5$	81
3-11	Comparisons of eigenfunctions of pressure perturbations between LES and prediction at $St = 0.1506$ for different azimuthal modes along the streamwise direction at $r/D = 3$	82
3-12	Eigenvalues as a function of St at different azimuthal modes.....	83
3-13	Eigenfunctions at $St = 0.12, 0.21, 0.4$, and 0.61 for 1 st mode and 2 nd mode for $m = 0$	84
3-14	Eigenfunctions at $St = 0.12, 0.21, 0.4$, and 0.61 for 1 st mode and 2 nd mode for $m = 1$	85
3-15	Eigenfunctions at $St = 0.12, 0.21, 0.4$, and 0.61 for 1 st mode and 2 nd mode for $m = 2$	86
3-16	Eigenfunctions at $St = 0.12, 0.21, 0.4$, and 0.61 for 1 st mode and 2 nd mode for $m = 3$	87
3-17	The comparison of eigenfunctions for different azimuthal modes at $St = 0.1506$	88
3-18	Far-field noise comparisons on a polar arc of $100D$ relative to the nozzle exit at different St	90
3-19	Far-field noise comparisons on a polar arc of $100D$ at different St at different azimuthal modes.	91
3-20	Comparison of auto-correlation between the predictions' and FWH results from $\psi = 160^\circ$ to $\psi = 50^\circ$	93
3-21	Comparison of cross-correlation between the predictions' and FWH results from $\psi = 160^\circ$ to $\psi = 50^\circ$ at far-field, where the reference microphone is at $\psi = 150^\circ$ and $R/D = 10095$	
3-22	Coherence of far-field pressure perturbations along with St for $\psi = 150^\circ$ vs $160^\circ, 90^\circ$, and 50°	96
3-23	Coherence of far-field pressure perturbations at different angles at $St = 0.1, 0.2$, and 0.4 , where the reference microphone is at $\psi = 150^\circ$	96
3-24	Isometric view of SolidWorks Nozzle (Top Left); Cut View of SolidWorks Nozzle (Top Right); Side View of Nozzle (Bottom Left); Front View of Nozzle (Bottom Right).	97

3-25	Comparisons of mean flow at the centerline and momentum thickness between LES and RANS.	98
3-26	Phase speed and growth rate at different St computed from the mean flow of LES and RANS.	99
3-27	Phase speed and growth rate along the streamwise direction computed from the mean flow of LES and RANS.	99
3-28	Comparisons of far-field sound spectra between the experiment and KS method at sideline and downstream directions.	101
3-29	Comparisons of OASPL among predictions, the KS method, and experimental measurement.	102
3-30	Comparisons of far-field sound spectra among the instability wave solutions, KS method, and experiment in the upstream, sideline, and downstream directions.	102
3-31	Comparisons of near-field sound spectrum between the instability wave solutions and experiment at upstream direction ($\psi = 50^\circ$).	103
3-32	Comparison of auto-correlation between the predictions' and experimental results from $\psi = 150^\circ$ to $\psi = 60^\circ$	105
3-33	Comparison of maximum cross-correlation among the predictions, the KS method, and experimental results from $\psi = 140^\circ$ to $\psi = 60^\circ$, where the reference microphone is at $\psi = 150^\circ$	106
3-34	Comparison of maximum cross-correlation between the near- and far-field acoustic pressure from the prediction, the KS method, and experiment. The reference microphone is in the near-field.	107
3-35	Coherence of far-field acoustic pressure at different angles for St = 0.2, 0.35, and 0.6, where the reference microphone is at $\psi = 150^\circ$	107
3-36	Coherence of near- and far-field acoustic pressure at different angles at St = 0.2, 0.35, and 0.6, where the reference microphone is at $\psi = 50^\circ$ and $R/D = 15$	108
4-1	The domain and computational grid near the nose.	109
4-2	Residual and Y plus of the CFD simulation for the coarse grid point distribution.	110
4-3	The comparison of axial velocity and temperature at different streamwise positions, where $x^*/L = 0.624, 0.76$, and 0.825	111
4-4	Mach number contours at r_1, r_7 , and r_{10} at $M_\infty = 2$	112
4-5	Mach number contours at r_1, r_7 , and r_{10} at $M_\infty = 3.5$	113
4-6	Mach number contours at r_1, r_7 , and r_{10} at $M_\infty = 5$	114

4-7	Comparison of normalized amplitudes of eigenfunctions between the LST prediction and the results from Mayer (Ref).....	116
4-8	Comparison of maximum growth rate over all frequencies and spanwise wavenumber along streamwise direction for r_1 to r_{10} at $M_\infty = 2, 3.5$ and 5	117
4-9	Spatial coherence of different nose radii from r_1 to r_{10} at $M_\infty = 2$, where the reference point of each case is at the maximum grow rate along streamwise direction.....	119
4-10	Spatial coherence of different nose radii from r_1 to r_{10} at $M_\infty = 3.5$, where the reference point of each case is at the maximum grow rate along streamwise direction.....	120
4-11	Spatial coherence of different nose radii from r_1 to r_{10} at $M_\infty = 5$, where the reference point of each case is at the maximum grow rate along streamwise direction.....	121
4-12	Grid distribution.	122
4-13	Comparison of pressure coefficient of base flow and flow with plasma actuator model. .	123
4-14	Pressure distribution at the surface z_c	124
4-15	Temperature distribution at the surface z_c	124
4-16	Temperature distribution at the surface y_c	124
4-17	Comparison of temperature and velocity between base flow and flow with plasma actuator model of r_1, r_7 , and r_{10} at $x^* = x_c$ at $M_\infty = 2$	126
4-18	Comparison of temperature and velocity between base flow and flow with plasma actuator model of r_1, r_7 , and r_{10} at $x^* = x_c$ at $M_\infty = 3.5$	127
4-19	Comparison of temperature and velocity between base flow and flow with plasma actuator model of r_1, r_7 , and r_{10} at $x^* = x_c$ at $M_\infty = 5$	128
4-20	Relative temperature difference caused by the plasma actuator at $x^* = x_c$ for r_1 to r_{10} at $M_\infty = 2, 3.5$, and 5	130
4-21	Comparison of maximum growth rate over all frequencies and spanwise wavenumber along streamwise direction of flow with plasma actuator model for r_1 to r_{10} at $M_\infty = 2, 3.5$ and 5	131
4-22	Relative difference of maximum growth rate along streamwise direction for r_1 to r_{10} at $M_\infty = 2, 3.5$ and 5	132
4-23	Spatial coherence of flow with plasma actuator model for r_1 to r_{10} at $M_\infty = 2$	133
4-24	Spatial coherence of flow with plasma actuator model for r_1 to r_{10} at $M_\infty = 3.5$	134
4-25	Spatial coherence of flow with plasma actuator model for r_1 to r_{10} at $M_\infty = 5$	135

Abstract of Dissertation Presented to the Graduate School
of the University of Florida in Partial Fulfillment of the
Requirements for the Degree of Doctor of Philosophy

THE APPLICATION OF INSTABILITY WAVE THEORY ON ACOUSTIC RADIATION
WITHIN OFF-DESIGN SUPERSONIC JETS AND ON TWO-POINT STATISTICS WITHIN
HIGH-SPEED FLOW OVER SHARP AND BLUNT CONES WITH PLASMA ACTUATION

By

Jianhui Cheng

August 2022

Chair: Steven A. E. Miller

Major: Mechanical Engineering

The intense noise generated by large-scale turbulent structures is the main component of acoustic radiation from jets, especially in the downstream direction, which is harmful to human health. Furthermore, the high-frequency waves created by boundary layer turbulence can cause intense vibrations on vehicle surface structures during rocket launch. It can be simplified as a cone flow. As instability waves are closely connected with the formation of large-scale turbulent structures, instability wave theory is applied to compute the radiated noise in the far-field for free jets and the pressure fluctuations on the cone surface. A phenomenological plasma actuator model is applied to alter the flow-fields and stability properties of the cone flows.

We compute the radiated noise from instability waves within two off-design supersonic jet flows. The directivity and azimuthal properties of jet noise from large-scale turbulent structures in the downstream direction are captured. The spectral density of noise in the downstream directions agree well with the experimental measurements, whereas they are lower at the upstream direction. The auto-correlation shows similar behavior both in the downstream and upstream directions. The cross-correlation and coherence shows higher values than the prediction from the Kirchhoff surface method and experimental measurements. The results show that the noise from instability wave models in the upstream and downstream direction are highly correlated. The results could be used for future flow control on noise reduction from large-scale turbulent structures.

We examine the effect of plasma actuation on the pressure fluctuations from the instability waves on the cone surface via theory with flow-fields predicted by computational fluid dynamics. We present predictions for a seven-degree half-angle cone at free-stream Mach 2, 3.5, and 5 with varying nose radii. Nose radii range from 0.038 to 38.1 mm and represent both sharp and large leading edge bluntness. For non-actuated flows, we observe that very small radii leading edges do not alter the maximum growth rates. Large radii cones have lower growth rates due to a thicker boundary layer. Spatial coherence of the instability waves decreases with increasing frequency. The growth rates are smaller at higher freestream Mach number. The effect of the simulated plasma actuator adds local heating to the flow-field. We find that plasma actuation stabilizes the flow-field and spatial coherence becomes smaller. The results are beneficial for future flow control to reduce the vibration from large-scale turbulent structures.

CHAPTER 1 INTRODUCTION

1.1 Motivation and Background

Turbulent motions are located everywhere, such as winds and currents in the atmosphere and ocean [1]. Turbulence is found in almost all industrial flows and remains a predominant problem within the aerospace industry. Turbulence can be found in all speed regimes - subsonic, transonic, supersonic, and hypersonic. It has been shown that turbulence can be problematic. For example, the jet noise problems found within jet engines and the vibration and cabin noise of high-speed flight vehicles caused by the aerodynamic loading from turbulence. Previous investigations illustrated that specific turbulent structures play important roles for noise radiation, such as fine- and large-scale turbulent structures. Therefore, one fundamental goal is to predict the noise from the turbulent structures and control them. Lower order models, such as theoretical modeling (instability waves method [2, 3]) and decomposition methods [2, 4, 3], can be cost less than direct computation to achieve these goals and illustrate the physical mechanisms. In this dissertation, we apply these methods to predict the noise and loading and show the possibility to control the large-scale turbulent structures.

Firstly, the study of noise from jet engines became an active area of research since the 1950s [5] and is still a major concern in military and commercial aviation due to the increasing demand in both military and commercial sectors. Jet noise causes health problems [6]. For example, long time exposure to jet noise causes cardiovascular related disease due to increasing hypertension and blood pressure [6]. For military applications, the intensity of jet noise on an aircraft carrier deck ranges from 120 to 150 dB at peak frequencies [7]. The noise is detrimental to the health and hearing of the military personnel working in close proximity to the aircraft on an aircraft carrier [7].

There is a long history of noise regulation since the first Federal Aviation Administration (FAA) regulation in 1969 [5]. Figure 1-1 shows aircraft noise reduction trends, where the noise level for high-performance military aircraft is compared to commercial aircraft [5]. The latest standards are called stage 4 and were established in 2005. The FAA stage 5 became effective in 2017 and 2020, respectively. It can be seen that Stage 5 (Chapter 14) requires newly certified

aircraft to reduce 7 effective perceived noise (EPN) dB relative to Stage 4. This requirement exerts more challenges to aircraft manufacturing and jet engine design. Recent major efforts included projects WP-1583 [8] and WP-1584 [9], which reduced noise by approximately 2 dB through fluid injection and chevron technology, respectively. The project, WP19-1014 [10], aims at reducing noise by studying and destroying the large-scale turbulent structures, which is the focus of this dissertation.

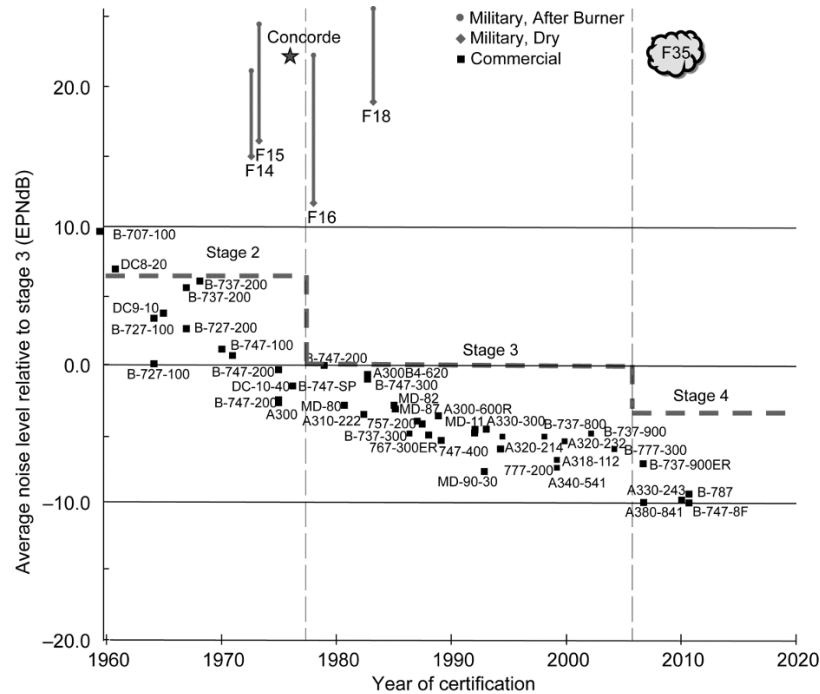


Figure 1-1. Aircraft noise reduction trends.

Lighthill published two now famous papers [11, 12] explaining how sound is generated from a turbulent flow, and a new era of aeroacoustics began. A number of researchers [13, 14, 15, 16, 17, 18] focused on explaining the noise generation mechanism, determining the noise source, propagation, and predicting the sound pressure level (SPL) numerically and theoretically. Tam [19] argued that there are three basic components of supersonic jet noise. These are turbulent mixing noise, broadband shock-associated noise (BBSAN), and screech tones. Tam et al. [20] argued that turbulent mixing noise is associated with two turbulent structures within jet flows, namely, fine- and large-scale turbulent structures. Large-scale coherent structures [21] radiate and dominate in the downstream direction relative to the nozzle exit. Noise

from large-scale turbulent structures also radiates in the upstream direction, however, it is dominated by the noise from fine-scale turbulent mixing noise and BBSAN [22]. On the other hand, formation of the turbulent structures has largely been considered a phenomenon of flow-instability due to the similarities between transitional and turbulent structures. Consequently, coherent structures may be viewed as instability modes of the basic flow. It has been shown that some of the theoretically predicted results agree well with experimental data [23, 24, 18, 16, 17].

Methods to control noise via different approaches [25, 26, 27] were also investigated. For example, an overall sound pressure level (OASPL) reduced roughly 6 dB in the peak jet noise reduction with water pressure over 2000 kPa and injection at lower pressure (roughly 1034 kPa) has resulted in a 1.6 EPN dB reduction [26]. However, reduction of noise from large-scale turbulent structures remains one of the most difficult challenges in practical jet engine development. The present research seek methods to ultimately lower the noise from this dominant noise source.

Our aim is to examine the statistical relation between downstream and upstream radiating noise from large-scale turbulent structures within jets. By understanding the statistics of large-scale radiation, we hope to create the possibility of one-day designing a feedback control system for the noise from large-scale turbulent structures within free jets. This approach will rely on the ability to extract the upstream propagating noise from the large-scale structures from within a signal that is dominated by fine-scale mixing noise. Such sensors might be mounted on the aircraft wing. Wing mounted microphones for jet noise measurement were pioneered in World War II by the Germans on the Messerschmitt Me 262 [28]. The control signal after extraction would be used to feed an actuator within the nozzle system of the aircraft.

Secondly, leading edge geometries of flight-vehicles experience intense aerodynamic loading at high-speeds. Instability waves, that lead to transition to turbulence, create large pressure fluctuations on the surface of vehicles. The action of the stochastic pressure distribution associated with instability waves and turbulence provides the driving force that excites the underlying structure [29, 30]. This excitation in turn generates intense vibrations on the payload,

personnel, or other critical flight-vehicle systems [31, 32] during rocket launching [29]. Reduction of these vibrations will increase flight-vehicle safety [33], reduce vibration induced failure of satellites [33], and reduce noise for astronauts [33, 34]. Therefore, accurate external wall-pressure predictions are necessary for leading geometries at supersonic and hypersonic speeds. This will allow designers to possess improved prediction tools so that they may lower weight of vehicles and reduce harmful vibrations.

Previous investigations [35, 36, 37, 38] have explored the effect of different semi-empirical models fitted to experimental data to describe the wall pressure fluctuations on a rigid plane wall due to a turbulent boundary layer (TBL). High-speed boundary layers are unstable and instability waves form. The existence of large-scale coherent motions within high-speed flows has been identified [39, 40] and defined via statistical means [41], instantaneous flow patterns [42], stability theory [43], and techniques from dynamical systems theory [3]. Stability theory has been applied to study the transition of the boundary layer and the effect of heat exchange on the vehicle surface (see for example Malik [44], Malik and Spall [45], Knisely and Zhong [46], Laible et al. [47]). Various parameters, including body configurations, the Mach number, wall temperature, entropy layer, and roughness, would affect the stability and transition within boundary layer flows [39]. However, there are some discrepancies between the results of experimental and numerical studies about the transition locations. Additionally, the general law of the effects of wall temperature is not obtained or unknown to our community.

Therefore, we propose to apply stability theory to compute pressure fluctuations from the instability waves on cones by changing leading edge radii and free-stream Mach numbers. These geometries are selected because they are similar to the leading edges of supersonic and hypersonic flight-vehicles and represent prototypical geometry for investigating boundary layer stability and transition [48]. In addition, we also propose to investigate the variations of stability properties by adding a plasma actuator.

1.2 Objective and Scope of Proposed Work

There are two research focuses in this dissertation, and both of them are related to the effects of large-scale turbulent structures. The main objectives and the methods to achieve them are:

- Increase understanding of physics of the dominant noise produced from turbulent structures within high-speed jet flows: To achieve this, theoretical and numerical methods will be used to compute the noise in the upstream and downstream directions for two off-design supersonic jets. The prediction approach is instability wave theory, which has been used to predict the radiated noise [16, 17]. The numerical methods is the Kirchhoff surface method [49] in conjunction with CFD.
- Provide a theoretical foundation for a control mechanism that aims to reduce the noise in the downstream direction via measuring and controlling the upstream noise: The statistics of pressure perturbations will be analyzed. The correlation and coherence analysis are applied. The foundation of this analysis is that the results of auto-correlation of different noise sources show different behavior [50, 51].
- Create a database and present a prediction methodology of excitation for vibration analysis and noise of boundary layer flows: Different cone flow conditions are investigated. The spatial coherence is an important terms of the formula of excitation within structure-acoustic problems [34] and properties of coherent structures [52].
- Provide the possibility to control the intensity exerted on the rocket surface: The phenomenological plasma actuator model is added within boundary layer flows to achieve this goal. The variation of flow-fields and stability properties affect the spatial coherence of pressure fluctuations. These results show that plasma actuation is a promising flow control methodology.

Noise and vibration are the by-products of the turbulent flow-fields, therefore, it is necessary to understand the associated flow structures and fluid dynamics. The basic descriptions and development of the flow-fields for free jets and TBLs are discussed in Section 1.2. Supersonic jet noise, including the characteristics, classification, and prediction methods are reviewed in Section 1.3. The stability modes within boundary layer flows and the parameters that can alter the stability properties will be reviewed in Section 1.4. The application, mechanism, and computation of plasma actuation for flow control are reviewed in Section 1.5. The organization of the rest of the dissertation is presented in Section 1.6.

1.3 Flow Structures

In this section, the flow development of free jets and turbulent boundary layer will be reviewed, which provides the foundation for understanding flow structures presented in this

dissertation. Additionally, a description and definition of coherent structures are presented. A general form of instability waves is shown.

1.3.1 Free Jets

A free jet is a fluid mass that discharges into an infinitely large environment of ambient fluid [53]. The structure and development of a free jet is shown in Fig. 1-2 (modified from [53]). It can be seen that there are distinct zones, which are related to the centreline velocity decay. The first important region is called the potential core of the jet, where the centreline velocity is equal to the nozzle outlet velocity. Specifically, as the fluid leaves the nozzle, the diffusion of momentum between the expelled fluid and the quiescent medium gradually decelerates the high-velocity flow through air entrainment by its surroundings [53]. The mixing layer or shear layer is generated between the moving and quiescent fluids, which spreads as the jet develops downstream. The mixing process in the shear layer near the nozzle creates Kelvin-Helmholtz instabilities that grow as they are advected by the mean flow [54]. During this process, large-eddies or large-scale turbulent structures are formed due to the large velocity difference at the surface between the jet fluid and ambient, which cause intense lateral mixing. These large-eddies will become weaker downstream from their location of formation and breakdown into fine-scale turbulent structures, and finally become fully turbulent [53]. Noise is radiated in all directions during this process [13]. Characteristics of the radiated noise will be discussed in the section on jet noise.

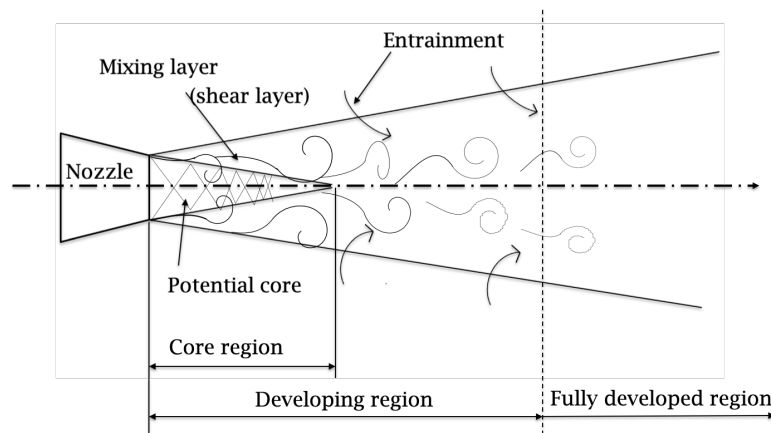


Figure 1-2. Free jet flow structure.

In order to generate a large amount of thrust, a nozzle is used in a jet engine to accelerate the fluid flow exiting the engine. The design Mach number, M_d , of the nozzle is related to the ratio of the area of the exit and throat of the nozzle, as

$$\frac{A_e}{A^*} = \frac{1}{M_d} \left[\frac{2}{\gamma+1} \left(1 + \frac{\gamma-1}{2} M_d^2 \right) \right]^{\frac{\gamma+1}{2(\gamma-1)}}, \quad (1-1)$$

where A_e is the area of the exit, A^* is the area of throat, and γ is the specific heat. The operating condition of a nozzle depends on the nozzle pressure ratio (NPR) and the total temperature ratio (TTR). The NPR is defined as the ratio of the stagnation pressure to the ambient pressure. Similarly, the TTR is defined as the ratio of the stagnation temperature to the ambient temperature. The fully-expanded jet Mach number, M_j , is defined as

$$M_j = \left[\frac{2}{\gamma-1} \left(\text{NPR}^{\frac{\gamma-1}{\gamma}} - 1 \right) \right]^{1/2}. \quad (1-2)$$

If $M_d = M_j$, the jet is said to be operating at the on-design condition. If $M_d \neq M_j$, the jet is said to be operating at an off-design condition. For the off-design condition, the pressure at the nozzle exit, p_e , is not equal to the atmospheric pressure, p_∞ . A Shock-cell structure in the jet exhaust is formed when the jet operates off-design (see the potential core of Fig. 1-2). If pressure at the exit is lower than the atmospheric pressure, the flow is said to be over-expanded.

Conversely, if the pressure at the exit is higher than the atmospheric pressure, the flow is said to be under-expanded. These pressure miss-matches creates an initial expansion wave or shock wave, respectively, that creates the semi-periodic shock-cells in the plume.

1.3.2 Boundary Layer Flows

A boundary layer is typically a thin region of fluid immediately adjacent to a solid structure, along which a fluid is moving [55]. The region outside the boundary layer is often relatively undisturbed compared to the region very near the wall. Any interactions between the fluid and the surface of the solid takes place through that layer of fluid. Boundary layers can be laminar, transitional, or turbulent, depending on the velocity, density, viscosity of the fluid, and the characteristic length of the solid surface. A TBL is characterized by high Reynolds number

($Re_x = \rho u x / \nu$, where ρ is the density, u is the velocity, and ν is the viscosity), which is the ratio of inertial force to viscous force. For flow over a flat plate, the transition from laminar to turbulent flow occurs at a Re_x of approximately 10^5 to 10^6 .

Figure 1-3 shows the development of the flow for the simplest TBL over a flat-plate [56]. Three regions are formed along the streamwise direction. The flow development for a cone configuration is similar with this figure, but with a more complex flow-field. An oblique shock for a sharp cone or bow shock for a blunt cone will appear at the front of the cone. As for a flat plate, a thin boundary layer develops resulting from the skin friction between the flow and the surface.

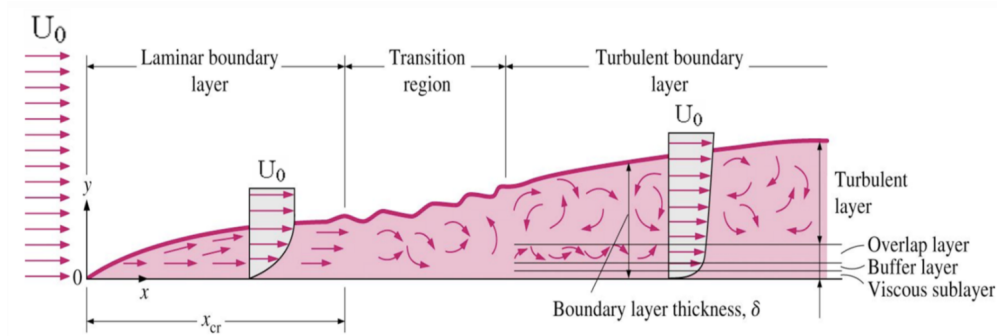


Figure 1-3. Turbulent boundary layer flow structure.

Experimental and numerical studies of wall-bounded flows reveal the different shapes and types of flow structures [39, 40], such as hairpin vortex, typical eddies, and pocket packet, etc. (see Fig. 1-4). Numerous efforts have been devoted to examining the characteristics of the structures and identifying their functions in the onset and production of turbulence [39]. In a compressible boundary layer, typical flow structures have been observed, such as three-dimensional wave packets [39]. The first and second mode instability waves play important roles in the transition process. Mach number, roughness, wall temperature, and other factors will affect the development of the flow structures.

1.3.3 Coherent Motions

The existence of coherent vortical structures in turbulent flows has been known for many decades, but the exact definition of coherent structure remains controversial, beyond the requirement that coherent motions have significant correlation in space and time [57]. Two main

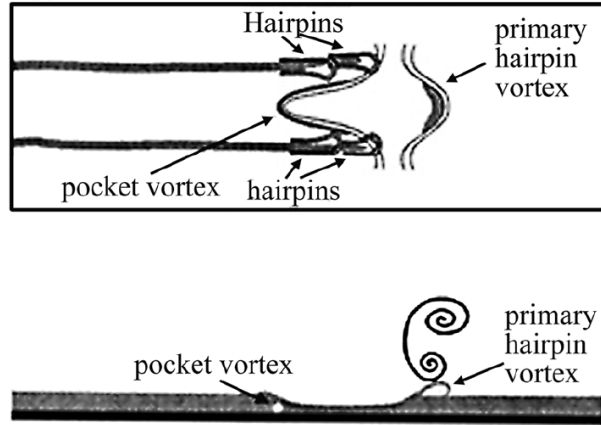


Figure 1-4. A temporal phase of the evolution of typical eddies, where the pocket and primary hairpin vortex are formed.

views are proposed to define the coherent structures summarized by Sharma and McKeon [58]. One is derived from statistical measures of the velocity field and scaling arguments based on dimensional analysis in physical and spectral space [58]. A second view focuses on the dynamics and spatial organization of coherent structure [58]. For example, Robinson [40] defined coherent motion as a three-dimensional region of the flow over which at least one fundamental flow variable, such as velocity component, density, temperature, etc., exhibits significant correlation with itself or with another variable over a range of space and/or time that is significantly larger than the smallest local scales of the flow. This definition has been used as the criteria to determine the jet noise at the downstream direction is from large-scale turbulent structures based on the correlation analysis of far-field noise of experimental measurements [50, 59].

In the second view point, coherent structures are loosely defined as regions of concentrated vorticity, which has recurrence, appreciable lifetime, and scales (see Fiedler [52]). It is also shown that the coherent turbulent structures in a turbulent flow are regions or motions of apparent order as observed from flow visualization that show considerable similarity to the instability waves observed in the range of laminar-turbulent transition [58]. This observation provides the possibility to apply instability wave theory to investigate the effects of coherent structures. In addition, coherent structures can be reduced to (combination of) a small number of elements, namely line vortex, ring vortex, hairpin vortex, and helical vortex [52].

One of the existing theoretical models of coherent structures are linearised Navier-Stokes equations, which may be classified as physically derived models. The spatially growing instability wave within the flow-fields are used to describe the flow-fields or fluctuation flow-fields governed by the linearised Navier-Stokes equations. It can be used to predict the transition of boundary layer flow or acoustic radiation. The LST is based on the normal mode analysis under a local parallel-flow assumption. Specifically, the linear fluctuations of flow variables are decomposed into the following normal mode form as

$$q'(x, y, z, t) = \hat{q}(y) \exp(i(\alpha x + \beta z - \omega t)), \quad (1-3)$$

where q' stands for any of the independent flow variables u, v, w, p, ρ (or T), \hat{q} is the complex amplitude of the disturbances or shape function, α and β are the wavenumber, and ω is the radial frequency. Equation (1-3) will be modified for jet flows and boundary flows attached to cone. The specific form of the instability waves will be given for different flow type in the later Chapters.

1.4 Supersonic Jet Noise

1.4.1 Characteristics of Jet Noise

Figure 1-5 shows the typical noise spectra of a high-speed off-design supersonic jet at various radiation angles (Ψ) [60]. The y-axis is SPL and the x-axis is non-dimensional frequency, $St = fD/u_j$, where D is the diameter of the nozzle, f is frequency, and u_j is the jet velocity. The mixing noise, BBSAN, and screech of jet noise are labeled with arrows and different colors. It can be seen that turbulent mixing noise is broadband in nature and is the most dominant noise in the downstream direction. Screech tones and BBSAN are most dominant in the upstream and sideline directions. Furthermore, mixing noise is dominant at mid- to low-frequencies. The BBSAN generation is associated with the interaction between the large turbulent structures and the quasi-periodically oscillating shock-cell structures.

1.4.1.1 Turbulent Mixing Noise

Tam et al. [20] argued that turbulent mixing noise is associated with fine- and large-scale turbulent structures from high-speed jets. The noise from large-scale turbulent structures

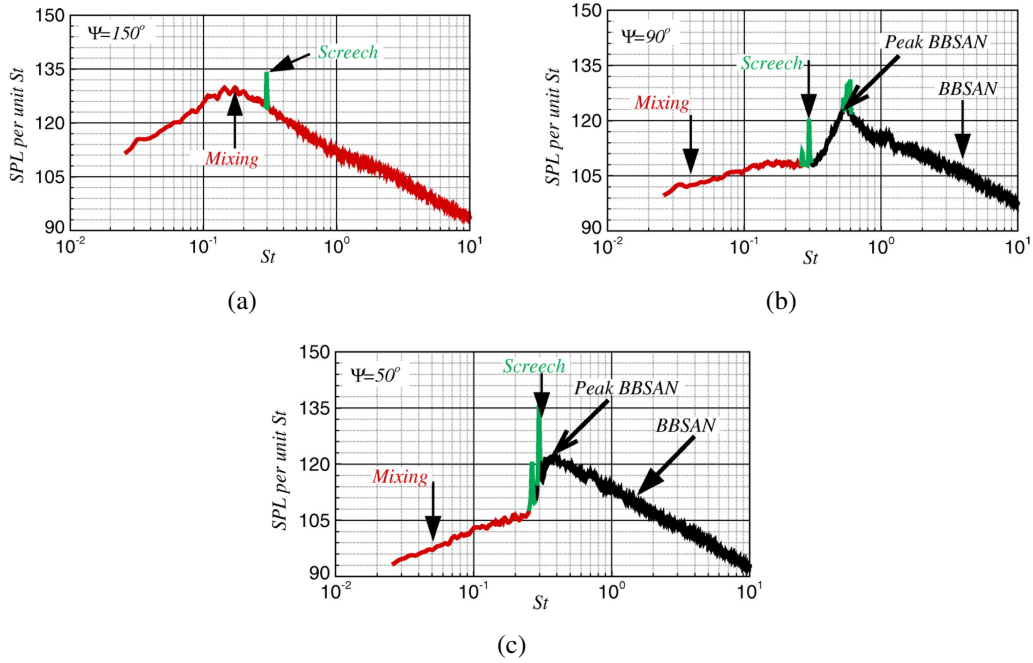


Figure 1-5. Three components of an under-expanded supersonic jet noise at various radiation angles, $M_d = 1$, $M_j = 1.5$, and TTR=1.00, data from NASA Glenn Research Center courtesy of Miller.

dominates in the downstream direction, while the fine-scale turbulent noise is less directional and dominates in the sideline and upstream directions [4].

Figure 1-6 is the SPL for two heated jets at $St = 0.25$ at azimuthal mode $m = 0$ [54]. It can be seen that the dominant noise is at the angular sector between 30 to 60 degrees measured relative to the jet downstream direction, which is the turbulent mixing noise. In the upstream direction, the noise intensity is low and nearly uniform with respect to frequency [13]. This noise is believed to be generated by the fine-scale turbulence of the jet flows. In addition, the intensity, the directivity, and spectral characteristics of the turbulent mixing noise of supersonic jets depend on the velocity of jet exhausts [13]. It can be seen that the difference between the maximum and minimum power is approximately 25 dB for high-speed jets, $M_\infty = 1.5$, whereas it is approximately 13 dB for low-speed jets, $M_\infty = 0.5$ [4]. Furthermore, the higher jet temperature can broaden the dominant noise lobe in the downstream direction and increase the overall noise radiation [19].

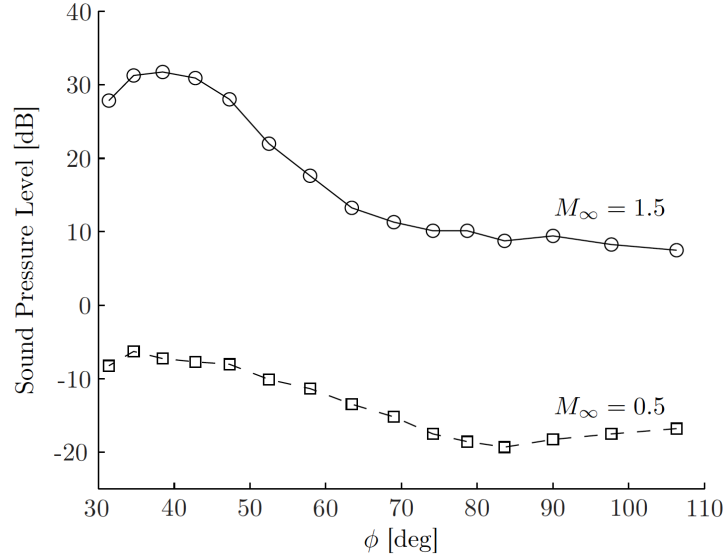


Figure 1-6. Acoustic power measurements for two heated jets at $M_j = 0.5$ and 1.5 , TTR=2.7, azimuthal mode $m = 0$, and frequency $St = 0.25$.

An early attempt to represent sound sources (large-scale turbulent structures) as instability waves was from Liu [61]. He found that some of these instability waves travel supersonically with their peak amplitude inside the shear layer and decay in the radial direction away from the jet. The wavy wall analogy can be used to explain the sound generation mechanism from instability waves. The large-scale turbulent structures and instability waves of the jet are statistically equivalent [13]. Near the nozzle exit, the large velocity gradient across the shear layer causes the instability wave to have a very large growth rate. As the instability wave propagates downstream the shear layer thickness increases, which leads to a reduction of growth rate. Eventually the wave becomes damped (growth rate less than zero) as they propagate further downstream. The growth and decay of the instability wave amplitude leads to a broadband wavenumber spectrum. The large-scale turbulent structures of the jet flow may not be the most important noise generators for low speed subsonic jets.

1.4.1.2 Screech Tones

Screech is a form of aeroacoustic resonance observed in shock-containing supersonic jets [62]. The mechanism and prediction of the screech tone frequencies are examined, see Powell [63, 64], Norum [65], and Tam and Tanna [66], as examples. It is found that the fundamental

screech tone radiates primarily in the upstream direction. The appearance of a screech tone is usually accompanied by its harmonics.

The screech tone generation process involves a feedback loop rendering the flow periodic with accompanying emission of a sharp tone [22]. Specifically, acoustic disturbances impinging on the jet mixing layer near the nozzle lip excite the intrinsic instability waves of the jet flow. The instability wave propagates downstream, extracts energy from the mean flow and grows rapidly in amplitude. The instability wave having acquired a large enough amplitude interacts with the quasi-periodic shock cells in the jet plume after propagating four to five shock cells distance. The unsteady interaction generates acoustic radiation in the upstream direction. Upon reaching the nozzle lip region, the acoustic disturbances excite the shear layer of the jet, which leads to the generation of new instability waves. In this way, the feedback loop is closed.

The dominant screech tone exhibits a mode-switching phenomenon as the jet Mach number increases [22]. At low Mach number, the screech tones are associated with the toroidal mode (axisymmetric mode, azimuthal mode $m = 0$). As Mach number increases, there is a switch over to the flapping/helical mode ($m = \pm 1$). Furthermore, the intensity of screech tones generally decreases with an increase in jet temperature. This is because the instability wave is the energy source of the feedback phenomenon.

1.4.2 Prediction of Jet Noise with Acoustic Analogy

There are many review articles on the aeroacoustics of jets and the methodologies to compute jet noise [67, 68, 69]. One very prominent method is called the acoustic analogy, which in theory can be used to predict noise from both large- and fine-scale turbulent motions. However, this requires complete knowledge of the source terms which in practice are not available, particularly for the fine-scale turbulent structures. It also implies that the complete solution of the Navier-Stokes equations is already known, and therefore the acoustic analogy would not be needed to predict the radiated field.

The acoustic analogy is a method to predict noise based on the equations of motion and to relate radiated noise to equivalent analogous sources. Lighthill [11] rearranged the Navier-Stokes

equations into a wave operator and equivalent source shown as

$$\frac{\partial^2 \rho}{\partial t^2} - c_\infty^2 \nabla^2 \rho = \frac{\partial^2 T_{ij}}{\partial x_i \partial x_j}, \quad (1-4)$$

where $T_{ij} = \rho u_i u_j + (p_{ij} - c_\infty^2 \rho \delta_{ij})$ is the Lighthill's stress tensor, c_∞ is the sound speed, ρ is the density, p_{ij} is the compressive tensor, δ_{ij} is Kronecker delta function, and u_i and u_j are the velocity components.

Equation (1-4) describes the sound generated by turbulence. This equation was solved with the method of the Green's function convolved with the right hand side of Eqn. (1-4). Dimensional analysis shows the far-field acoustic intensity is proportional to the predicted eighth power of the jet velocity, u_j^8 . The jet noise directivity is validated theoretically [12]. The angle of maximum noise radiation is $\sec^{-1} M_c$, where M_c is the convective Mach number. The noise produced by large-scale turbulent structures can be evaluated by separating the flow fluctuations are decomposed into coherent and random components [70]. Freund and Colonius [71] proposed that the reconstructed flow-fields with selected proper orthogonal decomposition (POD) modes may be a valuable component of a reduced model for predicting the sound radiated by the large-scale turbulent structures if the reconstructed structures are well-correlated with the radiating portion of the Lighthill source [71].

Ffowcs Williams [72] investigated the effects of convection of turbulent structures within jets and showed that the radiation dependence is proportional to u_j^3 at supersonic convection speeds. Ffowcs Williams and Hawkings [14] derived the FWH equation

$$\left(\frac{\partial^2}{\partial t^2} - c_\infty^2 \frac{\partial^2}{\partial x_i^2} \right) (\rho - \rho_\infty) = \frac{\partial^2 T_{ij}}{\partial x_i \partial x_j} + \frac{\partial}{\partial t} \left(\rho_\infty u_i \delta(f) \frac{\partial f}{\partial x_i} \right) - \frac{\partial}{\partial x_i} \left(p_{ij} \delta(f) \frac{\partial f}{\partial x_i} \right), \quad (1-5)$$

where f is the generalized function defined the surface introduced, which is negative inside the surface, positive outside, and exactly zero on the surface. The first term is the quadrapole source distributed everywhere outside the enclosing surface, and the strength density is T_{ij} , consistent with the Lighthill's stress tensor. The second and third term are known as monopole and dipole

sources, respectively. The wave equation with the second or third source term is called the thickness noise equation or loading noise equation [73].

Ffowcs Williams also proposed to use a penetrable (porous or permeable) data surface to account for nonlinearities in the vicinity of a moving surface. The FWH equation for penetrable (permeable, porous) data surface is

$$\left(\frac{\partial^2}{\partial t^2} - c_\infty^2 \nabla^2 \right) [(\rho - \rho_\infty)H(f)] = \frac{\partial^2}{\partial x_i \partial x_j} [T_{ij}H(f)] + \frac{\partial}{\partial t} [Q\delta(f)] - \frac{\partial}{\partial x_i} [F_i\delta(f)], \quad (1-6)$$

where $F_i = -[p\delta_{ij} + \rho u_i(u_n - v_n)] \frac{\partial f}{\partial x_j}$, $Q = [\rho_\infty v_n + \rho(u_n - v_n)] \frac{\partial f}{\partial x_i}$, u_n is the fluid velocity in the direction normal to the surface $f = 0$, v_n is the surface velocity in the direction normal to the surface, and $H(f)$ is the Heaviside function, which is unity in the entire region and zero outside the region.

Di Francescantonio [74] derived the FWH equation (Eqn. (1-5)) and the Kirchhoff governing equation

$$\square^2 p' = - \left(\frac{\partial p'}{\partial t} \frac{M_n}{c_\infty} + \frac{\partial p'}{\partial n} \right) \delta(f) - \frac{\partial}{\partial t} \left[p' \frac{M_n}{c_\infty} \delta(f) \right] - \frac{\partial}{\partial x_i} \left[p' \frac{\partial f}{\partial x_i} \delta(f) \right], \quad (1-7)$$

where \square is the wave operator and $M_n = v_n/c_\infty$.

Farassat [73] solved Eqn. (1-5) with the free-space Green's function in the time-domain without considering the quadrupoles, which is more suitable for computation. It is also more efficient if one uses the porous approach, as they are automatically accounted for if a surface encloses the sources. The porous surface approach means that a surface integral is performed in the flow-field about the sources. Brentner and Farassat [75] compared the source terms and the acoustic results of Eqns. (1-5) and (1-7) based on the two methods of Ffowcs Williams and Hawkings [14]. They pointed out that the FWH equation is based on the conservation laws of fluid mechanics, while the Kirchhoff formulation is based on the wave equation [75]. The FWH equation is equivalent to the Kirchhoff governing equation when the integration is located in the linear flow region.

Another important modification based on the Lighthill's acoustic analogy is from Lilley [76], which took into account the refraction of the mean flow and was called the modified acoustic analogy. Goldstein [77] achieved the same result as Lilley by linearizing the equation with the known mean flow. Goldstein [78] later proposed the generalized acoustic analogy, which decomposed the flow-field into the base- and perturbation- flow. The linearized Navier-Stokes equation (LNS) are solved with the vector Green's function. The solution of homogeneous LNS equations for the steady non-parallel base flow can be assumed as the valid instability waves, which is usually associated with the large-scale coherent structures. The acoustic analogies are also applied to the prediction of BBSAN and two-phase flow. For example, Miller [60] proposed a comprehensive model using an acoustic analogy that has been used to compute the BBSAN. Balachandar et al. [79] pointed out the mechanism of sound generation mechanism in the particle-laden jets.

1.4.3 Instability Wave Models within Jet Flows

There are strong similarities between transitional and turbulent structures. Therefore, formation of the turbulent structures has largely been considered a phenomenon of flow-instability. Consequently, coherent structures may be viewed as instability modes of the basic flow, where classes of coherent structure can be described with representative mode superpositions [58]. Instability waves have been used to predict the far-field noise directly or indirectly. It has been shown that some of the theoretically predicted results agree well with experimental data [23, 24, 18, 16, 17]. The near-field results of instability wave models combined with the acoustic analogy [70, 80, 81] or KS integral method [2, 49, 82] are applied to compute the far-field noise, which is the indirect way. Also, wavepacket methods, that are empirical in nature, can predict the far-field noise if tuned to instability waves.

Liu [70, 83] attempted to model and validate the sound sources as instability waves based on shadowgraphic evidence and near-field acoustic measurements. He separated the flow quantities in the compressible equations of fluid motions into mean, large-scale, and fine-scale components to develop integral equations representing energy transfer between these

components. A single azimuthal-frequency component of the large-scale turbulent structure with the wavelike pattern as the instability wave model was proposed as

$$p(x, r, \theta, t) = A(x)\hat{p}(x, r)\exp\left(i\int_0^x \alpha_r(\xi)d\xi\right)\exp(im\theta - i\omega t) + c.c., \quad (1-8)$$

where $A(x)$ is an amplitude function that varies along the jet, α_r is the wavenumber corresponding to the real frequency ω , and $c.c.$ denotes complex conjugate of the first term.

The global amplitude of the instability wave within Eqn. (1-8) along with the streamwise direction was found through the energy integral. The amplitude of the instability wave obtains a peak within the shear layer and decays with distance perpendicular to the shear layer. The near-field fluctuations resulting from instability wave analysis were used in the Lighthill integral to represent the source terms for far-field noise calculations.

The experiment was conducted at a low Re conditions [84, 42] and later extended to measurements at moderate Re [85] to establish the link between large-scale coherent structures and the noise radiation from supersonic shock free jets. The results show that the rapid growth of instability waves and their decay near the end of the potential core contributed to the major portion the sound radiated (see the work from McLaughlin et al. [84]). Initial instability wave growth rates and phase velocities agreed with linear stability theory. Additionally, the peak St numbers of the measured jet noise spectra appropriately agreed with that of predicted from instability wave source [84].

Oertel [86] observed three families of instability waves in their supersonic jet experiments as shown in Fig. 1-7: the Kelvin-Helmholtz, the supersonic, and the subsonic instability wave [43]. Tam and Hu [43] showed the properties of instability waves in the near-field and the corresponding effects on the radiated noise. The results showed that the Kelvin-Helmholtz instability waves (labeled w' in Fig. 1-7) are responsible for the formation of large-scale turbulent structures and showed parallel pattern. The supersonic instability waves (labeled w in Fig. 1-7) also radiated noise to the far-field only at a very high Mach number. The subsonic instability waves (labeled w'' in Fig. 1-7) decay in a small region and do not radiate the sounds in the

far-field. In this dissertation, the jet Mach number did not reach the region where the supersonic instability waves appear. Therefore, we focus on the Kelvin-Helmholtz instability waves in the following sections.

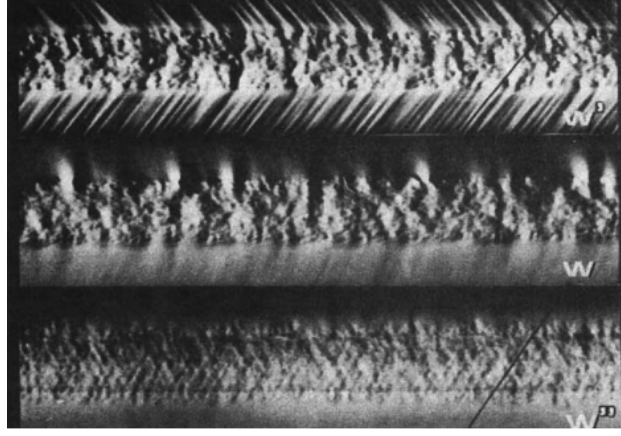


Figure 1-7. Wave patterns of three sets of instability waves, Kelvin-Helmholtz, supersonic, and subsonic instability waves from top to bottom.

Other researchers, however, have found discrepancies between the measurements and theoretical analysis for the dominant St [87]. Crighton and Gaster [87] suggested that growth rates and wave lengths depend significantly on the radial, as well as the axial location at which they are measured. Another cause of discrepancies lies in the fact that nonlinear effects are actually significant. Quasi-parallel flow theory is unable to predict variation of a mode characteristics with radial position nor with axial position. Crighton and Gaster [87] believed that an obvious step to take to overcome these difficulties is to incorporate the effect of axial variation of the mean flow into the analysis. These treatments involve a WKB (Wentzel–Kramers–Brillouin) or slowly varying type of approximation which is readily formalized by a multiple-scales as

$$p(x, r, \theta, t) = \sum_{n=0}^{\infty} \epsilon^n \hat{p}_n(s, r) \exp\left(i \int^x \alpha(\epsilon \xi') d\xi'\right) \exp(im\theta - i\omega t), \quad (1-9)$$

where $s = \epsilon x$ denotes the slow variable, ϵ is a small constant, n is the order, and $\alpha = \alpha_r + i\alpha_i$. The growth rate is $-\alpha_i$, and the phase speed is $u_p = \omega/\alpha_r$.

Equation (1-9) models a wave that propagates through a slightly inhomogeneous medium formed by the turbulent mean flow. Such a wave is represented analytically in the form of an

asymptotic expansion with ϵ , the rate of spread of the mixing layer. The growth rate and phase speed are two important factors that determine the sound radiation and intensity. The phase speed of instability waves is responsible for the efficiency and directionality of the radiated noise [22]. When the phase speed of the instability wave is supersonic relative to the ambient speed of sound, the jet flow has an intensive Mach wave radiation and the direction is normal to the Mach wave front [22]. When the propagation velocity of the instability wave is subsonic, the amplification and dampening of the wave will also radiate noise to far-field [22]. The reduction of the growth rate and phase speed of disturbances in the Kelvin-Helmholtz instability has the potential to reduce the sound radiated from wavepackets in the jet [88]. The noise-reduction devices cause changes in the turbulent mean flow of a jet, which reduce the growth rates of modes predicted according to a linear stability analysis [25].

Mohseni [89] compared the near-field pressure perturbations from DNS, LNS, and instability wave solutions to verify the instability wave models. The amplitude of the instability wave was scaled with the simulation results. Kopiev et al. [23] computed the near-field pressure fluctuations via the instability wave models and compared with the experiment at a lower frequency range. The comparison showed that eliminating the amplitude function of the instability wave will cause the peak of radiation to move upstream.

The parabolized stability equations (PSE), initially developed by Herbert and Bertolotti [90, 91], takes into account the non-parallelism of the flow compared with LST. The derivation process includes separating the perturbation quantities into a function varying in the streamwise direction at a similar rate with the mean flow and a rapidly wave-like part as

$$p(x, r, \theta, t) = \hat{p}(x, r) \exp\left(i \int^x \alpha(\xi) d\xi\right) \exp(im\theta - i\omega t). \quad (1-10)$$

PSE have been used to analyze the streamwise growth and decay of linear and nonlinear disturbances in slowly varying shear flows such as boundary layers, jets, and far wakes. Malik and Chang [92] computed the growth rate of instability wave evolution in the streamwise direction with PSE for a supersonic jet. Piot et al. [93] and Cheung et al. [80] applied the PSE

methods to subsonic and supersonic jets. The comparison of spatial growth rate of the disturbances among the PSE prediction, DNS, and large-eddy simulation (LES) shows good agreement. The maximum pressure disturbance amplitude is reached near the end of the jet potential core. The PSE stability approach is very efficient for predicting the spatial development of jet large-scale instabilities in both subsonic and supersonic case.

Furthermore, the complex amplitude of the instability wave must be determined to complete the expression of instability waves and investigate their contribution in the near- and far-field regions. The matching process are always used to determined the amplitude by calibrated with the database of DNS, LES, or experimental measurement.

One method is an adjoint formulation, which is used to solve the receptivity problem in boundary layer and shear flows. Ryu et al. [2, 49, 94] applied the method to estimate amplitudes for the instability waves based on bi-orthogonality between the solution of the adjoint linearized Euler equations (LEE) and eigenfunctions of adjoint PSE. The amplitudes are computed with two projection of DNS results for a subsonic jet ($M_j = 0.9$) and LES results for supersonic jets ($M_j = 1.95$). The contribution of instability waves in the noise generation are well evaluated with this method. However, this method shows limited success for turbulent flow.

Two alternative methods uses least square. One is kinetic energy matching [2, 94], and the other is modulus and phase matching [95, 49, 82]. For both approaches, the cost function needs to be determined between the simulation/experiment and the LST/PSE results. The absolute value of amplitude can be obtained by minimizing the cost function of kinetic energy. During this process, the assumption that the kinetic energy in a turbulent jet is dominant by large-scale turbulent structures, which can be well represented by instability waves are valid. Therefore, the amplitudes of instability waves can be calibrated with kinetic energy matching.

An appropriate flow region needs to determine the modulus and phase of the amplitudes of instability wave. The flow region in the radial direction can be divided into linear and non-linear regimes [95] as shown in the Fig. 1-8. The amplitude of eigenfunction of $m = 0$ along the radial direction is shown, where the different regimes are labeled. It can be seen that the

linear-hydrodynamic regime is dominated by the instability wave. Suzuki and Colonius [95] placed a conical array in this region and effectively extracted the instability waves. They showed that a phased-microphone array placed in this region is capable of detecting instability waves based on the beam-forming theory. Ryu et al. [94, 2, 49] applied this method by using the results from PSE and the results of LES or DNS for both subsonic and supersonic jets and good agreement was achieved when substituting the results to compute the far-field noise.

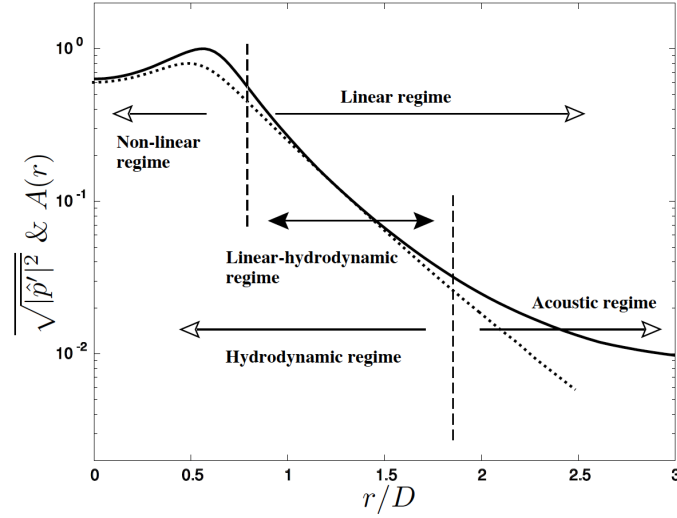


Figure 1-8. The flow regions of a round jet in the radial direction. The solid line depicts the time-averaged pressure fluctuation of $m = 0$ at $x/D = 4$ from DNS, and the dotted line denotes the corresponding eigenfunction calculated from a LST.

The results of least-square matching method can be improved by extracting the large-scale turbulent structures from a numerical simulation or experimental result. The POD, dynamical mode decomposition (DMD), resolvent analysis, momentum potential theory (MPT) [96] and wavelet transforms [97] are usually used to extract the most energetic part to represent the large-scale turbulent structures. Gudmundsson and Colonius [4] used PSE to compute pressure fluctuations associated with large-scale structures and filtered out the uncorrelated fluctuation via POD. A better agreement between theory and experimental data are achieved. Sinha [98] applied the POD to LES results and extracted the most energetic coherent component and matched with the PSE to compute the amplitudes. It shows that the acoustic field is well predicted via the Kirchhoff method [98], where the data on the Kirchhoff surface is the results of PSE.

Even though the instability wave models are generally regarded as a local model, they can be extended to a global solution and compute the far-field noise. Tam and Morris [24] explained the boundness of the instability wave solution obtained from multiple-scales analysis and computed the noise radiated from the large-scale turbulent structures in a plane turbulent shear layer. Tam and Burton [17, 16] extended this method by separating the flow-field into the inner and outer region, applied the matched asymptotic expansion to combine the inner and outer solutions, and constructed the far-field noise by using the stationary phase approximation method to the outer solution. The far-field pressure was predicted and validated for a round jet at $M_j = 2$. Dahl [99] adopted this method for supersonic coaxial jets, and the directivity pattern agreed well with the measurements. The effect of jet heating was taken into account through a modification of an amplitude function of the instability wave. Dahl's results [99] were validated for the single frequency and azimuthal modes of instability wave. However, the far-field sound from large-scale turbulent structures is a broadband spectrum, which means the effects of all instability waves must be included. Tam and Chen [18] solved this problems and quantified the effects of the whole instability wave by applying a stochastic turbulence theory [100]. This dissertation provides a review of the solution in Chapter 2 with an accompanying numerical implementation.

1.4.4 Wave-Packet Method

The wave-packet method is a semi-empirical approach [69] inspired by the instability wave theory, which can be used to connect the turbulent structures and radiated noise. One approach is to use a wave-packet ansatz of Papamoschou [101, 102] in a fixed surface at the flow region, as

$$p_w(r_0, x, \theta, t; \omega, m) = p_0(x) \exp(im\theta - i\omega t), \quad (1-11)$$

where $p_0 = A(x) \exp(i\alpha x)$ is the shape function with $A(x)$ an amplification-decay envelope containing several unknown parameters that represents the axial coherence length scale, and α is the instability wavenumber.

The radiated far-field pressure can then be computed via the wave equation with the superposition of a self-similar wave-packet at spectrum of frequencies as the sound sources. The

parameters of the wave-packet ansatz are found via calibration with measurement data.

Wavepacket results show that the broadening of the spectrum with increasing polar angle can be explained on the basis of a single noise source (wave-packet). On the other hand, the filtered far-field results are also used to determine the parameters of wave packets. Knig et al. [103] applied wavelet transform to the far-field acoustic data and obtained the noise from large-scale turbulent structures and then obtain the parameters of wave packets.

Another way is to express the near-field pressure statistics by a wave-packet model from Reba [104, 105], as

$$R_m(x, x', \omega) \equiv \int_{-\infty}^{\infty} \langle p_m^*(r_1, t) p_m(r_2, t + \tau) \rangle \exp(i\omega\tau) d\tau$$

$$= A(\bar{x}/L_1) \exp[-(\Delta x/L_2)^2] \exp(ik(\bar{x})\Delta x), \quad (1-12)$$

where $\bar{x} = (x + x')/2$ is the mean microphone location, $\Delta x = (x - x')/2$ is the microphone half-separation, length scale L_1 characterizes the streamwise extent of the source region, and L_2 characterizes the streamwise correlation scale. The far-field pressure distribution is computed via a Green's function of the wave equation. The unknown parameters are obtained by comparing with the statistics of near-field measurements.

1.5 Stability Analysis of Boundary Layer Flows

There are different stable and unstable modes with corresponding effects within boundary layer flows [106, 107, 108]. The properties and applications of the typical stability modes and the effects of nose bluntness and wall temperature on the stability and transition are reviewed.

1.5.1 Stability Modes

Mack modes, that include the first and the second mode, are most discussed among the unstable and stable modes within boundary layer flows. The first mode (Mack's first mode), which is an extension of the Tollmien-Schlichting (TS) instability wave present in incompressible flows [45]. This wave is most amplified when it is an oblique wave at supersonic Mach numbers and represents viscous instability at low Mach numbers [45]. Additionally, there exist an infinite

number of modes when the wave speed is supersonic within boundary layer flows (Mode I, Mode II, etc. [107]), and the second mode (Mack's second mode) forms. The second mode is significant at boundary layer edge Mach numbers (M_e) approximately above 4, has growth rates much higher than the first mode, and is most amplified when the wave angle is zero or is a two-dimensional wave. In fact, studies also showed that the Mack modes are slightly unstable in different regions of frequencies [107, 39]. Figure 1-9 shows the distribution of growth rates and phase speeds with non-dimensional frequency at $M_\infty = 7.99$ (adopted from Zhong and Ma [107]). It can be seen that the first- and second modes are continuous with frequency but within different regions. The first mode are slightly unstable in the range of lower frequencies $0.0485 < \omega < 0.126$ or $33.1 < f^* < 86.1$ kHz, and the second mode are unstable in the range of $0.171 < \omega < 0.243$ or $116.7 < f^* < 165.9$ kHz. The first mode is responsible for transition when the wall is adiabatic for freestream Mach number (M_∞) up to approximately 7 [109].

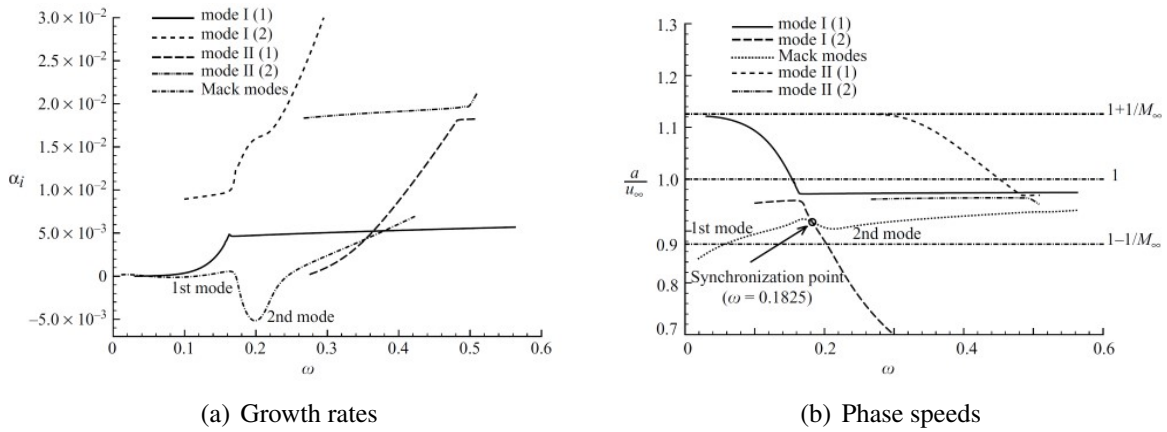


Figure 1-9. The distribution of growth rates and phase speeds of different stability modes with frequency at $M_\infty = 7.99$.

The stability analysis of the compressible boundary layer has been applied to study the transition of the boundary layer and the effect of heat exchange on the vehicle surface [44, 45, 46, 47]. It is believed that the mechanism of transition from laminar to turbulent flow is consequence of instability of laminar boundary layer [110]. The first and second mode instability waves play important roles in the transition process [39, 110]. In this dissertation, the effects of nose bluntness [111, 112, 113, 110, 114, 108] and wall temperature [115, 116, 117, 118, 119] are

reviewed due to the importance of these two factors in altering the stability properties and the transition process.

Nose bluntness has been used to mitigate the heat transfer rates and stabilizes hypersonic boundary layers. For the mean flow-field of the blunt-nosed body, a detached shock (bow shock) is formed at the leading edge. A strong entropy layer forms across the bow shock. The entropy layer persists for a long distance before it merges with the developing boundary layer along the wall in the downstream direction [120].

It is found that the transition Reynolds number is very sensitive to the bluntness ratio of the body [110]. The instability properties of the axisymmetric flow along sharp and blunt cones of different nose radii at Mach 8 are studied [113]. This numerical analysis computes first and second-mode boundary-layer disturbances and covers the regions of small and large bluntness. A monotonic downstream shift of second-mode critical Reynolds number is found in both regions. A sudden upstream shift of first-mode critical Reynolds number in the region of large bluntness could be identified [113].

Transition has been studied experimentally and numerically relative to nose bluntness. However, the boundary layer transition mechanisms in such geometries are not yet well understood. There are discrepancies for transition locations (x_T) between experimental measurement and numerically prediction. In the experimental measurement, cones with nose radii ranging from 0.7937 to 38.1 mm, were tested, and transition locations were measured [121]. Several experiments have noted a delay in the onset of transition with increasing nose bluntness. However, the transition reversal phenomenon was reported, which means the transition point moves upstream after certain critical values of nose radii [121, 122]. LST studies combined with an empirical method (e^N) is used to predict the transition position for such geometries. According to the results, no reversal phenomenon of transition position based on the prediction from the second-mode instability waves [111]. In addition, disagreements are found between the transition locations of LST-predicted and these of experimentally observed. For example, the predicted transition position from LST is much larger than the experimental measurements at Mach 5.43 for

nose radii 12.7 mm and 38.1 mm [111]. The value of x_T is larger than 3.2 m (maximum length for numerical simulation) from numerical calculations, whereas the transition position is 0.24 m from experimental measurement with nose radius 38.1 mm [111]. The hypothesis caused the disagreement between the experimental measurement and numerically prediction are the experiments were conducted in a noisy tunnel environment, there is a likelihood that the reversal is caused by some uncontrollable noises with the amplitude large enough that the growths of disturbances bypass the linear region and force the transition to occur earlier [111].

On the other hand, flight test data about transition positions at different conditions are summarized [112]. Figure 1-10 shows the value of x_T at different edge Mach number (M_e) with different nose radii and cone angle based on the results of flight test [112], where the nose bluntness are different. Therefore, there is no obvious trend from this result. However, it can be seen that the value of x_T are less than 0.7 m.

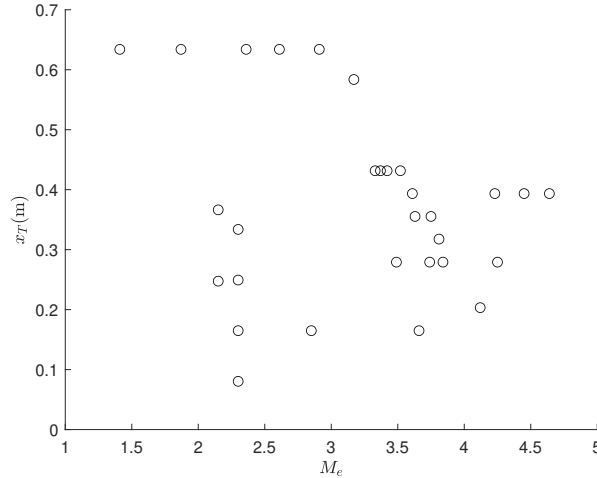


Figure 1-10. The transition positions at different M_e based on the results of flight test.

It is also well known that the linear stability within compressible boundary layer flows is very sensitive to the wall temperature [116, 119]. The influence of wall temperature on receptivity and transition depends on several factors, such as the competition between the first- and second-modes, the position of cooling or heating, and the method of heating or cooling way (local or global). However, there is no general law governing the effect of wall temperature on the

transition process [39]. The physical and dynamical processes that affect aerodynamic heating are yet to be explored. The relevant experimental studies are of great significance for engineering guidance.

The known effects of uniform temperature of surface can be found from Masad et al. [115], where the surface cooling can stabilize the first-mode disturbances and destabilizes second-mode disturbances. It explains that the surface cooling generates the generalized inflection point near the wall which results in the boundary layer becomes stable with inviscid perturbations. The local heating/cooling surface shows different effects compared with the uniform heating/cooling. Polivanov et al. [118] studied the effects of cooling/heating elements with different lengths, temperature, and positions on the stability of a hypersonic boundary layer via LST and direct numerical simulation. They found that heating elements increase the growth rate of the first and second mode around the heating source region and downstream region. The transition positions are also altered, which moves upstream with heating and delayed with cooling. The results show that the position of the cooling source should not be too far downstream so that the cooling elements can be effective on the stability and transition positions. Sidorenko et al. [117] studied hypersonic boundary layer stability and transition experimentally and numerically for a 7 degree half-angle cone ($M_\infty = 6$) equipped with a part of wall heating or cooling elements. The results showed that heating of the surface section accelerates the transition and cooling of the surface element delays the transition. These results are similar with Polivanov et al. [118]. The results of numerical simulation also agree with the experimental results.

Additionally, Masad et al. [115] investigated the effects of heat transfer on the spatial stability of compressible boundary layer. It is found that heat transfer is more effective in stabilizing or destabilizing flows at low freestream Mach numbers than high freestream Mach numbers. A sequence of simulations was conducted to study the effects of a cool wall on the flow-fields with thermal non-equilibrium at different frozen Mach number (M_a , flow with chemical reaction during small amount of time) at freestream conditions [119]. Bitter and Shepherd [119] fixed the wall temperature at 300 K and raised the free-stream temperature from

70 K to 2000 K. It is assumed that raising the freestream temperature is nearly equivalent to cooling the wall. The results are presented in Fig. 1-11 in terms of T_w^*/T_e^* and showed a monotonic increase in growth rate of the second mode as T_w^*/T_e^* become smaller. For the first mode, the growth rate decrease as T_w^*/T_e^* decrease except when T_w^*/T_e^* is less than 1, there is no instability.

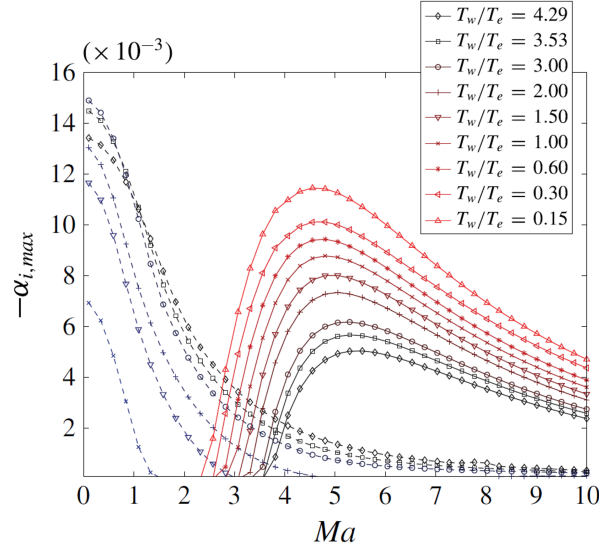


Figure 1-11. Effect of wall cooling on the maximum spatial growth rates of the first (dashed lines) and second (solid lines) modes along Ma for $Re = 1500$, $T_w^* = 300$ K, $T_e^* = 70 - 2000$ K, $p_e^* = 10$ kPa.

1.5.2 Cross-Power Spectral Density of Pressure Fluctuations

A turbulent boundary layer (TBL) is characterized by the development of large-scale structures from instabilities and turbulent eddies ranging through the entire cascade. High-speed boundary layers are unstable and instability waves form. The wall pressure fluctuations induced by instability waves and turbulent flow are broadband in nature. Thus, the wall pressure statistics are difficult to calculate, predict, or measure [34] as they are an imprint of instability waves or turbulence at the wall. The fluctuating pressures at the wall are usually described via statistics as the turbulent flow is random in nature. A large number of empirical and theoretical models [35, 36, 37, 38] have been developed to describe these random wall-pressure fluctuations, and the parameters of these models are fitted with experimental measurement.

One of the models for power spectral density (PSD) of the TBL wall pressure fluctuations was introduced by Corcos [37]. Corcos [37] developed a statistical empirical model that fit a large number of measurements of the pressure field from an attached flow, and provided the cross-power spectral density (CSD) of the wall pressure fluctuations. The expression of CSD is in a separable form along the spanwise and streamwise directions as

$$S(\xi_x, \xi_y, \omega) = S_{\text{ref}}(\omega) f_1\left(\frac{\omega|\xi_x|}{U_c}\right) f_2\left(\frac{\omega|\xi_y|}{U_c}\right) e^{\frac{-i\omega|\xi_x|}{U_c}}, \quad (1-13)$$

where $S_{\text{ref}}(\omega)$ is the reference auto-power spectrum, ξ_x and ξ_y are the spatial separations in the streamwise and spanwise directions of the plate, respectively, U_c is the convective speed of turbulence within the TBL, and functions f_1 and f_2 represents the particular form of the cross-spectral density $S(\xi_x, 0, \omega)$ and $S(0, \xi_y, \omega)$.

In practice, functions f_1 and f_2 are frequently approximated by exponential decay functions, such as,

$$S(\xi_x, \xi_y, \omega) = S_{\text{ref}}(\omega) e^{\frac{-\alpha_x \omega |\xi_x|}{U_c}} e^{\frac{-\alpha_y \omega |\xi_y|}{U_c}} e^{\frac{-i\omega|\xi_x|}{U_c}}, \quad (1-14)$$

where α_x and α_y are empirical parameters that denote the loss of coherence in the longitudinal and transverse direction, and are chosen to yield the best agreement with the experiment or flight-test.

The Corcos [37] model is well suited to describe the statistics of wall-pressure fluctuations induced by high-speed subsonic flows. Palumbo [123] has also applied the Corcos [37] model and others to high-speed supersonic flows using flight-test data, where it was shown that wind-tunnel measurements and calibrated coefficients did not match flight-test data. Graham [124] summarized different forms of empirical models for surface correlations, such as the Efimtsov model [38], the Ffowcs Williams model [36], or the Chase models [35]. These empirical models and corresponding experiments indicate a need for more first-principle based prediction approaches, as often the empirical models must be re-calibrated for particular flight-vehicles.

1.6 Flow Control via Plasma Actuators

The history of flow control over the 20th century has been well summarized by el Hak [125]. Flow control involves passive or active devices to change boundary layer or free-shear layer flows. The objectives of flow control are to delay or advance transition, to suppress or enhance turbulence, and to prevent or provoke separation. The final results achieved include drag reduction, lift enhancement, mixing augmentation, and flow-induced noise suppression, etc. [125].

It is well known that mixing and combustion, heat transfer, noise production and emission (pressure fluctuations), and wall-shear (frictional drag) are essentially determined by coherent (large-scale) turbulent structures [52]. Therefore, it is helpful to manipulate these process via altering the coherence of large-scale turbulent structures. Multiple methods to achieve this include but are not limited to fluid injection [57], filament or particulate injection [126], speakers, or plasma actuation. For example, Prasad and Morris [27] found the use of a single fluid injector helps break up the large-scale structures of the flows and hence reduce the jet noise based on the direct cross-correlations of the near-field data with the far-field microphone signals.

Additionally, the use of plasma-based devices has gained popularity in recent years, and attracted more and more attention [127]. The advantages of plasma actuators include fast time response, high frequency bandwidth, low mass, the absence of complicated mechanical or pneumatic systems, and adaption to different applications [127, 128]. Several reviews about plasma based flow control are available and in detail [127, 129, 130, 131].

The mechanism of plasma flow control [127, 132, 133] includes three main aspects. The first one is rapid gas heating of the flow achieved by volumetric heating (dilatation effect), as shown in Fig. 1-12(a). The contours of Joule heating distribution are shown. It can be seen that the high heat intensity is close to the electrodes and sustained to a distance over 1 cm above the plate. The second one is electro-hydrodynamic (EHD) forcing by imparting directed momentum to the bulk flow using electrostatic force generated by interaction of charge particles with an external electric field. The third one is magneto-hydrodynamic (MHD) forcing relying on the

Lorentz force on the bulk flow owing to the interaction of electrical currents with externally imposed magnetic field. Several experiments have been used to explained the mechanism and effects of plasma-based control on the flow-field [134, 135, 136, 137, 138, 139, 140]. For example, the shock angle in front of the body and the temperature distribution along the body surface can both be changed [129]. Figure 1-12(b) shows the image of the flow-field over flat-plate at $M_\infty = 2$ modified by the plasma actuator ($V_{HV} = -1.57$ kV and $I_{HV} = 74$ mA) [129], where the solid line represents the shock wave shape of the base flow-field. It can be seen that the shock angle increases with the electrodes in the leading edge of flat-plate.

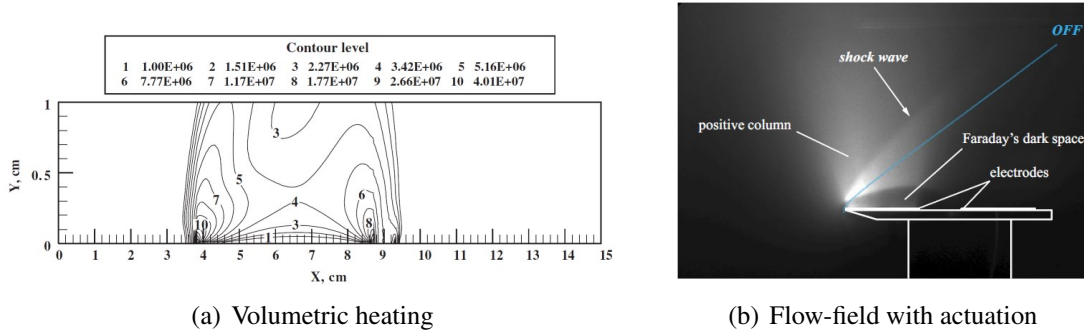


Figure 1-12. The contours of Joule heating distribution of flat-plate flow with a DBD plasma actuator and effects of plasma actuators on a flat-plate flow.

Furthermore, numerical methods are also applied to investigate the effects of plasma actuator. The effects of electromagnetic force on the aerospace vehicles introduced by the plasma actuator forms an interdisciplinary phenomenon. Therefore, in order to simulate this problem, the NS, energy, and Maxwell equations in the time domain must be integrated on a common frame of reference [141]. Additionally, a high-fidelity three-dimensional viscous methodology is required because the flow-fields of interest are typically characterized by transition and turbulence. This high-fidelity flow simulation technique is computationally intensive [128]. On the other hand, the magnetic Reynolds number is much less than unity in most aerospace applications [141]. Therefore, the fully coupled NS, energy, and Maxwell equations can be separated into two coupled groups under this conditions, the aerodynamic and electrodynamic formulation, by representing the Lorentz force and/or Joule heating as source terms. This is loosely coupled

first-principles approach, which can reduce computational complexity. Furthermore, the plasma-induced body force or heating source can be represented using a phenomenological model [134, 135, 142, 137, 138] as a right hand side source in the equations of motions, and are implemented in CFD solvers. This method is much simpler without solving Maxwell equations. For examples, Eqns. (1-15) and (1-16) are examples of the phenomenological models of plasma actuator to represent the body force with exponential distribution.

$$f_x = \frac{F_{x,0}}{\sqrt{F_{x,0}^2 + F_{y,0}^2}} \exp \left(- \left(\frac{(x-x_0) - (y-y_0)}{y-y_0+y_b} \right)^2 - \beta_x (y-y_0)^2 \right), \quad (1-15)$$

and

$$f_y = \frac{F_{y,0}}{\sqrt{F_{x,0}^2 + F_{y,0}^2}} \exp \left(- \left(\frac{(x-x_0)}{y-y_0+y_b} \right)^2 - \beta_y (y-y_0)^2 \right), \quad (1-16)$$

where $F_{x,0}$, $F_{y,0}$, β_x , β_y and y_b are constants, and x_0 and y_0 are the edge location of the electrodes.

This simplified method provides the primary control mechanism introduced by the actuator which consists of momentum or/and heating effects. Recent computations, comparing the phenomenological model with a first-principles approach, demonstrates that the same qualitative flow control behavior is captured with both methodologies.

The placement of the plasma actuator on the surface has a significant effect on the control of the flow-field [143, 139, 144]. For example, Updike et al. [144] demonstrated that a relatively large-scale MHD device applied at the corner could eliminate separation completely if a sufficiently strong accelerating force were applied. The dielectric barrier discharge (DBD) plasma actuator is most effective when applied at bifurcation points of the flow-field and successful applications are noted at the point of flow separation on the airfoil or near the dynamic stall of wings [132]. In addition, a phase array plasma actuators is used to alter the instability modes of jet, flat plate, and cone experimentally [139, 136, 145]. The design of plasma actuators based on the linear stability calculations to identify the range of unstable frequencies and wave angles, as well as the location of the lower neutral growth branch [136] so that the input power is lower.

1.7 Structure of the Dissertation

1.7.1 Chapter 2: Methodology

This chapter describes the instability wave methods used for noise predictions of free jets and pressure perturbation computations of boundary layer flows and other methods for analysis, such as POD and KS methods. For jet flows, the instability wave equations are derived from the compressible and inviscid equations of motions. The solutions in the inner and outer region are solved and combined with the matched asymptotic expansion method. The POD method is reviewed to refine the calibration process of amplitudes of instability wave solutions. The calibration method is based on the least-square principle. The KS method used to compute far-field noise is reviewed. For boundary layer flows, the governing equations of instability waves are derived from the viscous NS and energy equations. The pressure fluctuations from instability waves are constructed. The phenomenological plasma actuator model for flow control is shown.

1.7.2 Chapter 3: Jet Noise Prediction and Discussion

This chapter shows predictions from two separate jet flows: 1) a round convergent nozzle operating at under-expanded conditions, and 2) a bi-conic nozzle operating at over-expanded conditions. The flow-field, stability analysis, and correlation/coherence are discussed for each case. In particular, for case 1), the comparisons of shape functions in the near-field between the LES results and instability wave solutions are presented. The far-field SPL at different St for each azimuthal modes are compared among instability wave models prediction and FWH. For case 2), the far-field noise via the KS method is computed and validated. The SPL at near- and far-field noise from instability wave models are shown, where the amplitudes of instability waves are calibrated with the KS results.

1.7.3 Chapter 4: Cone Flow and Stability Calculations of Boundary Layers

This chapter shows the results that we obtained for flows over cone configurations. The flow-field via SU2 and stability properties of cone flow are computed and validated via CFD and the linear instability prediction code. The spatial coherence of pressure fluctuations from instability waves are shown. The parametric study is considered, where the different freestream

Mach numbers and nose radii are selected based on the base conditions. The flow structures with phenomenological plasma actuator model are shown and validated for a test case (ramp flow). Finally, the effects of the plasma actuator on the flow-field, stability properties, and spatial coherence are shown and compared.

1.7.4 Chapter 5: Summary and Conclusion

The final chapter presents a summary of the research effort. Major conclusions and outcomes are shown. Future research is proposed.

CHAPTER 2 METHODOLOGY

This chapter presents the analysis techniques for jet and boundary layer flows. The common method is the instability wave theory, which is used to predict the jet noise and the excitation to induce vibration within boundary layer flows. The similarity includes linearity the governing equations and expressing the perturbation fields with instability wave formula under different coordinate systems. However, the instability modes within jet flows is inviscid, whereas the viscous stability modes are investigated due to the high speed of boundary layer flows.

2.1 Methodology for Jet Flows

2.1.1 Instability Wave Theory

2.1.1.1 Governing Equations

The small perturbation equations that govern the instability waves for jet flows are derived from the linearized compressible, inviscid equations of motion in dimensionless form. The length, velocity, time, density, and pressure scales are the radius of the nozzle R_j , u_j (jet velocity), R_j/u_j , the jet fully-expanded density at the nozzle exit ρ_j , and $\rho_j u_j^2$, respectively. The governing equations are

$$\frac{\partial \rho'}{\partial t} + \bar{\mathbf{V}} \cdot \nabla \rho' + \mathbf{V}' \cdot \nabla \bar{\rho} + \bar{\rho} \nabla \cdot \mathbf{V}' + \rho' \nabla \cdot \bar{\mathbf{V}} = 0, \quad (2-1)$$

$$\frac{\partial \mathbf{V}'}{\partial t} + \bar{\mathbf{V}} \cdot \nabla \mathbf{V}' + \mathbf{V}' \cdot \nabla \bar{\mathbf{V}} + \frac{\rho'}{\bar{\rho}} (\bar{\mathbf{V}} \nabla \cdot \bar{\mathbf{V}}) = -\frac{1}{\bar{\rho}} \nabla p', \quad (2-2)$$

and

$$\frac{\partial p'}{\partial t} + \bar{\mathbf{V}} \cdot \nabla p' + \gamma \bar{p} \nabla \cdot \mathbf{V}' + \gamma p' \nabla \cdot \bar{\mathbf{V}} = 0, \quad (2-3)$$

where the prime denotes the perturbation or a small-amplitude instability wave, $\bar{\mathbf{V}} = (\bar{u}, \bar{v}, \bar{w})$ is the mean velocity vector, and $\mathbf{V}' = (u', v', w')$ is the velocity perturbation vector. Equation (2-1) is the linearized dimensionless continuity equation, Eqn. (2-2) is the linearized dimensionless momentum equation, and Eqn. (2-3) is the linearized dimensionless equation in terms of pressure combined the state and energy equations, and including the thermodynamic relation $h = c_p T$, where c_p is the specific heat, h is the enthalpy, and T is temperature.

The cylindrical coordinate system, (x, r, θ) , with its origin at the center of the nozzle exit is used. The term $\exp(im\theta - i\omega t)$ is separated from the solution because of the symmetry of the mean flow (azimuthal harmonics within round jets), and the assumption that the instability waves are generated by an external harmonic in time [23]. Therefore, all the physical variables are represented in a form such as $p'(x, r, \theta, t) = \text{Re}[p(x, r)\exp(im\theta - i\omega t)]$, where Re represents the real part. Equations (2-1) through (2-3) are now

$$-i\omega\rho + \bar{v}\frac{\partial\rho}{\partial r} + \bar{u}\frac{\partial\rho}{\partial x} + v\frac{\partial\bar{\rho}}{\partial r} + u\frac{\partial\bar{\rho}}{\partial x} + \bar{\rho}\left(\frac{1}{r}\frac{\partial vr}{\partial r} + \frac{im}{r}w + \frac{\partial u}{\partial x}\right) + \rho\left(\frac{1}{r}\frac{\partial\bar{v}r}{\partial r} + \frac{\partial\bar{u}}{\partial x}\right) = 0, \quad (2-4)$$

$$-i\omega u + \bar{v}\frac{\partial u}{\partial r} + \bar{u}\frac{\partial u}{\partial x} + v\frac{\partial\bar{u}}{\partial r} + u\frac{\partial\bar{u}}{\partial x} = -\frac{1}{\bar{\rho}}\frac{\partial p}{\partial x}, \quad (2-5)$$

$$-i\omega v + \bar{v}\frac{\partial v}{\partial r} + \bar{u}\frac{\partial v}{\partial x} + v\frac{\partial\bar{v}}{\partial r} + u\frac{\partial\bar{v}}{\partial x} = -\frac{1}{\bar{\rho}}\frac{\partial\bar{p}}{\partial r}, \quad (2-6)$$

$$-i\omega w + \bar{v}\frac{\partial w}{\partial r} + \bar{u}\frac{\partial w}{\partial x} + 2\frac{\bar{v}w}{r} = -\frac{1}{r^2}\frac{im}{\bar{\rho}}p, \quad (2-7)$$

and

$$-i\omega p + \bar{v}\frac{\partial p}{\partial r} + \bar{u}\frac{\partial p}{\partial x} + \gamma\bar{p}\left(\frac{1}{r}\frac{\partial vr}{\partial r} + \frac{im}{r}w + \frac{\partial u}{\partial x}\right) + \gamma p\left(\frac{1}{r}\frac{\partial\bar{v}r}{\partial r} + \frac{\partial\bar{u}}{\partial x}\right) = 0. \quad (2-8)$$

2.1.1.2 Instability Wave Solution

Inner Solution

Traditionally, Eqns. (2-4) to (2-8) are solved via multiple scales analysis. Tam and Morris [100] showed that the multiple scales analysis is not valid when the observer computational region is far from the shear layer. Tam and Burton [16, 17] separated the jet flow into an inner and outer region to solve Eqns. (2-4) to (2-8). The jet flow region is shown in Fig. 2-1.

The corresponding mean flow is represented as

$$\bar{\mathbf{V}} = (\bar{u}(x, r), \bar{v}(s, r), 0), \quad r < r_m \quad (2-9)$$

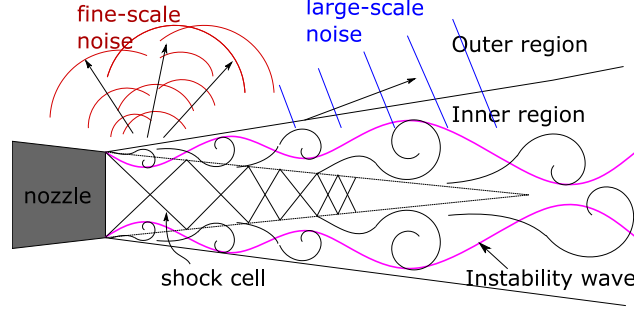


Figure 2-1. Jet flow region.

and

$$\bar{\mathbf{V}} = (0, \epsilon \bar{v}_\infty / r, 0), \quad r \geq r_m, \quad (2-10)$$

where r_m is the boundary between the inner and outer region and ϵ is the rate of spreading of the mixing layer, which is a small parameter.

The solution of Eqns. (2-4) to (2-8) can be expressed as an asymptotic series of waves traveling through a non-uniform medium, such as

$$p(s, r) = \sum_{n=0}^{\infty} \delta_n(\epsilon) \hat{p}_n(s, r) \exp(\phi(s)), \quad (2-11)$$

where $\delta_n(\epsilon)$ is the gauge function of the asymptotic expansion, the subscript n is the order of the flow properties, $\hat{p}_n(s, r)$ is the shape function, and $\phi(s) = i \int_0^s \alpha(s) ds$, where α is the local wavenumber.

The multiple scales analysis is applied in the inner region, and a slow variable $s = \epsilon x$ is introduced. Eqns. (2-4) through (2-8) can be simplified into an ordinary differential equation (ODE) by using ρ, u, v, w , and p in the form of Eqn. (2-11), combining the mean flow in the inner region (Eqn. (2-9)), transforming the coordinate system (s, r) , eliminating the term of $\exp(\phi(s))$, rearranging equations according to the order n , and eliminating other dependent variables. The final ODE in terms of \hat{p}_n is

$$\frac{\partial^2 \hat{p}_n}{\partial r^2} + \left[\frac{1}{r} + \frac{2}{\bar{\omega}} \frac{\partial \bar{u}}{\partial r} - \frac{1}{\bar{\rho}} \frac{\partial \bar{\rho}}{\partial r} \right] \frac{\partial \hat{p}_n}{\partial r} + \left[\bar{\rho} M_j^2 \bar{\omega}^2 - \frac{m^2}{r^2} - \alpha^2 \right] \hat{p}_n = G_n(r, s), \quad (2-12)$$

where $\bar{\omega} = \omega - \alpha \bar{u}$. The term G_n at the right side is only related to the lower order terms. When $n = 0$, the term G_n at the right side equals zero, namely, the equation becomes homogeneous and is called the Rayleigh equation, which is a simple differential equation in terms of the pressure perturbation.

Two types of stability analysis, temporal stability and spatial stability, can be formed by setting α as a real number or ω as a real number [54]. We focus on the spatial stability analysis. In this analysis, ω is a real number and fixed, the eigenvalue is $\alpha = \alpha_r + i\alpha_i$, and the corresponding eigenfunction is \hat{p} . The real part of the complex wave number, α_r , represents the number of axial oscillations per unit of space (axial wave number), and the phase speed is obtained from $u_p = \omega \alpha_r^{-1} = \pi St \alpha_r^{-1}$ [25]. The phase speed provides a measure of the convection speed of the instability wave. The growth rate is given by the negative imaginary part of the complex wavenumber, $-\alpha_i$. If the growth rate is positive, then the instability wave is amplified, whereas, the instability wave becomes damped if the growth rate is negative. In general, the growth rate of the instability wave will decrease as the jet shear layer becomes thicker, and further downstream, it becomes damped.

The solution of the Rayleigh equation can be expressed via the sum of two independent linear solutions, $\zeta_1^p(s, r)$ and $\zeta_2^p(s, r)$, as

$$\hat{p}_0(s, r) = A_0(s)\zeta_1^p(s, r) + B_0(s)\zeta_2^p(s, r), \quad (2-13)$$

where $A_0(s)$ and $B_0(s)$ are the amplitude functions varying in the streamwise direction. When r is close to r_m , the mean velocity is approximately zero. Thus, it requires $\zeta_1^p(s, r) \rightarrow H_m^{(1)}(i\lambda r)$. Here, $H_m^{(1)}(i\lambda r)$ is the m^{th} order of the first kind of the Hankel function and $\lambda(\alpha) = (\alpha^2 - \bar{\rho}_\infty M_j^2 \omega^2)^{1/2}$. The boundary condition for the jet centerline requires the solution to be finite as $r \rightarrow 0$. The amplitude functions will be determined later via the method of matched asymptotic expansions after finding the outer solution.

Outer Solution

In the outer region, multiple scales analysis is not valid because the perturbations have the same scale in each direction due to the assumption of zero mean velocity. An outer variable, $\bar{r} = \epsilon r$, is selected to ensure the same scale is obtained with the variable, s . We repeat the procedure for solving the inner solution except combine the mean flow in the outer region (Eqn. (2-10)), and perform the Fourier transform on the variable s . The final equation is

$$\left[1 - \epsilon^4 \bar{\rho}_\infty M_j^2 \frac{\bar{v}_\infty^2}{\bar{r}^2} \right] \frac{\partial^2 \tilde{u}}{\partial \bar{r}^2} + \left[\frac{1}{\bar{r}} + i \epsilon 2 \bar{\rho}_\infty M_j^2 \bar{\omega}_k \frac{\bar{v}_\infty}{\bar{r}} + \epsilon^4 \bar{\rho}_\infty M_j^2 \frac{\bar{v}_\infty^2}{\bar{r}^3} \right] \frac{\partial \tilde{u}}{\partial \bar{r}} + \left[\bar{\rho}_\infty M_j^2 \frac{\bar{\omega}_\infty^2}{\epsilon^2} - \frac{m^2}{\bar{r}^2} - k^2 \right] \tilde{u} = 0, \quad (2-14)$$

where \tilde{u} is the Fourier transform of u . Based on the relations between the dependent variables and inverse Fourier transform [18], the solution in terms of pressure at the outer region is

$$p(\bar{r}, s) = \int_{-\infty}^{\infty} g(k, \epsilon) \left[1 + i \frac{\epsilon^3}{\bar{\omega}_k} \frac{\bar{v}_\infty}{\bar{r}} \frac{\partial}{\partial \bar{r}} \right] \left\{ \left(\bar{r}^2 - \epsilon^4 \bar{\rho}_\infty^2 M^2 \omega^2 \bar{v}_\infty^2 \right)^{-1/2 i \epsilon^2 \bar{\rho}_\infty M_j^2 \bar{\omega}_k \bar{v}_\infty} \times H_q^1 \left(\frac{1}{i \epsilon} (\epsilon^2 k^2 - \bar{\rho}_\infty M_j^2 \bar{\omega}_k^2)^{1/2} \right) \left(\bar{r}^2 - \epsilon^4 \bar{\rho}_\infty^2 M_j^2 \bar{v}_\infty^2 \right) \right\} e^{i k s} dk, \quad (2-15)$$

where $g(k, \epsilon) = \frac{1}{2\pi} \int_{-\infty}^{\infty} \tilde{A}(s) e^{\int_0^x \phi(x) dx - i k s} ds$ and $\tilde{A}(s)$ is the amplitude function.

Matched Asymptotic Expansion

Based on the above analysis, there are three unknown amplitude functions in the inner and outer solutions. The method of matched asymptotic expansions is applied [99, 17] to find the relation between the amplitude functions. Van Dyke's principle [99] to match asymptotic expansions is used. Firstly, there is an overlapping region where the inner and outer solution are both valid. We can introduce an intermediate variables $\bar{r} = r \epsilon^{1/N}$ (N is a large positive number) in the overlapping region. Based on Van Dyke's principle, the limit of expansion of the inner solution and outer solution in terms of the intermediate variables should be equal [99].

The intermediate limit of the outer solution is obtained by letting $\eta = \epsilon k$, transforming Eqn. (2-15) from the (s, \bar{r}) to the (s, \tilde{r}) coordinates and asymptotically evaluating the transforming equation. The expression is

$$p^o(s, \tilde{r}) \sim e^{i\phi(s)\epsilon} \left\{ \tilde{A}_0(s) (1 - \epsilon \ln \epsilon \bar{\rho}_\infty M_j^2 \bar{\omega}_\infty \bar{v}_\infty) H_m^{(1)}(i\lambda(\alpha) \epsilon^{-1/N} \tilde{r}) \right. \\ \left. + \epsilon \left[\frac{1}{2} \pi \delta_{n0} \bar{\rho}_\infty M_j^2 \bar{\omega}_\infty \bar{v}_\infty \tilde{A}_0 + \tilde{A}_1 + E(\epsilon^{-1/N} \tilde{r}) \right. \right. \\ \left. \left. + D(\epsilon^{-1/N} \tilde{r}) \frac{\partial}{\partial(\epsilon^{-1/N} \tilde{r})} H_m^{(1)}(i\lambda(\alpha) \epsilon^{-1/N} \tilde{r}) \right] \right\} + O(\epsilon^2 \ln \epsilon), \quad (2-16)$$

where $\tilde{A}_0(s)$ is the first term of the asymptotic expansion of $\tilde{A}(s)$ in the outer solution, and E and D are functions in terms of intermediate variables (see [99]).

Similarly, the intermediate limit of the inner solution is obtained by transforming Eqn. (2-18) to an intermediate coordinate. With the relation \bar{r} fixed and ϵ closing to zero, the relation $\zeta_1^p(s, \bar{r} \epsilon^{-1/N}) \rightarrow H_m^{(1)}(i\lambda \bar{r} \epsilon^{-1/N})$ and $\zeta_2^p(\bar{r} \epsilon^{-1/N}, s) \rightarrow H_m^{(2)}(i\lambda \bar{r} \epsilon^{-1/N})$ can be obtained. Therefore, the intermediate limit of inner solution (Eqn. (2-18)) is expressed as

$$p_0^i(s, \tilde{r}) \sim e^{i\phi(s)/\epsilon} \left[A_0(s) H_n^{(1)}(i\lambda(\alpha) \epsilon^{-1/N} \tilde{r}) + B_0(s) H_n^{(2)}(i\lambda(\alpha) \epsilon^{-1/N} \tilde{r}) \right] + O(\epsilon \ln(\epsilon)), \quad (2-17)$$

Hence, by comparing the intermediate limit of the inner and outer solution, we can see that $\tilde{A}_0(s) = A_0(s)$ and $B_0(s) = 0$.

Therefore, only one unknown parameter is retained. Furthermore, if higher order are matched, $A_0(s) = \hat{A}_0 \exp[-\beta(s)]$ can be obtained, where $\beta(s) = \int_0^s I_2/I_1 ds$ is the non-parallel flow correction factor, I_1 and I_2 are two complex integral terms, and \hat{A}_0 is the amplitude of the instability wave at the nozzle exit plane.

To summarize, the inner solution and outer solution of zeroth order, in terms of pressure p , at the given radial frequency and azimuthal mode number are

$$p_0^{\text{inner}}(x, r, \theta, t; \omega, m) = A_0(x; \omega, m) \zeta_1^p(r, x; \omega, m) \exp \left[i \int_0^x \alpha(x; \omega, m) dx + m\theta - \omega t + (\pi/2) \right], \quad (2-18)$$

$$p_0^{\text{outer}}(x, r, \theta, t; \omega, m) = \int_{-\infty}^{\infty} \hat{A}_0(\omega, m) \hat{g}(\eta; \omega, m) H_m^{(1)}[i\lambda(\eta)r] \exp \{i[\eta x + m\theta - \omega t + (\pi/2)]\} d\eta, \quad (2-19)$$

and

$$\hat{g}(\eta; \omega, m) = \frac{1}{2\pi} \int_{-\infty}^{\infty} \exp \left\{ \left[i \int_0^x \alpha(x; \omega, m) dx - \eta x \right] - \beta(x; \omega, m) \right\} dx, \quad (2-20)$$

where $\hat{g}(\eta; \omega, m)$ is the wavenumber spectrum.

Formation of the Stochastic Instability Wave

In a high Reynolds number fully turbulent supersonic jet, there is a wide spectrum of instability waves. To be able to predict the supersonic jet noise, the entire instability wave spectrum must be considered [18]. Therefore, the stochastic theory is applied to instability wave theory to model the effect of all instability waves. The model contains an unknown initial wave amplitude $\hat{A}_0(\omega, m)$ from the previous section. It is set as a stochastic random function to represent the random character of large-scale turbulent structures. The normalized amplitude $a(\omega, m)$ of $\hat{A}_0(\omega, m)$ is defined as

$$\hat{A}_0(\omega, m) = \frac{a(\omega, m)}{|\zeta_1^p(0, r_{1/2}; \omega, m)|}, \quad (2-21)$$

where $|\zeta_1^p(0, r_{1/2}; \omega, m)|$ is the amplitude of the pressure eigenfunction at the half-velocity of the nozzle exit plane.

The auto-correlation function $|\zeta_1^p(0, r_{1/2}; \omega, m)|$ has the form of a product of the Dirac delta function because we assume that the instability wave spectrum is initiated by the white noise due to the lack of intrinsic length and time scales near the nozzle exit of a high Reynolds number

supersonic jet [18]. That is, the total pressure associated with instability waves can be represented by the form of the product of the delta function. The total inner pressure perturbations $p(x, r, \theta, t)$ are obtained by summing all the instability waves at each radial frequency and azimuthal mode. The ensemble average is [18]

$$\begin{aligned} \langle p(0, r_{1/2}, \theta, t), p(0, r_{1/2}, \theta + \Theta, t + \tau) \rangle = \\ \sum_{n=-\infty}^{\infty} \sum_{n'=-\infty}^{\infty} \int_{-\infty}^{\infty} \int_{-\infty}^{\infty} \frac{\langle a(\omega, m), a(\omega', m') \rangle \zeta_1^p(0, r_{1/2}; \omega, m) \zeta_1^p(0, r_{1/2}; \omega', m')}{|\zeta_1^p(0, r_{1/2}; \omega, m)| |\zeta_1^p(0, r_{1/2}; \omega', m')|} \\ \exp\{i[(m + m')\phi - (\omega + \omega')t + m\theta - \omega\tau + \pi]\} d\omega d\omega' = 2\pi^2 \tilde{D} \delta(\Theta) \delta(\tau), \end{aligned} \quad (2-22)$$

where $\langle \rangle$ denotes ensemble average, Θ is phase lag, τ is retarded time, and \tilde{D} is the area of the auto-correlation function, which is the only unknown parameter.

The ensemble average of the normalized amplitude function is

$$\langle a(\omega, m), a(\omega', m') \rangle = (\tilde{D}/2) \delta(\omega + \omega') \delta_{m, -m'}, \quad (2-23)$$

where $\delta_{m, -m'}$ is Kronecker delta function and defined as

$$\delta_{m, -m'} = \begin{cases} 1 & \text{for } m + m' = 0 \\ 0 & \text{for } m + m' \neq 0. \end{cases} \quad (2-24)$$

Similarly, the total pressure perturbation outside the jet is obtained by summing Eqn. (2-19) at each radial frequency and azimuthal mode. The power spectra density $S(x, r, \theta, \omega)$ of the acoustic pressure is the Fourier transform of the autocorrelation of the total outer pressure perturbation. The result is [18]

$$S(x, r, \theta, \omega) = \frac{1}{2\pi} \int_{-\infty}^{\infty} \langle p(x, r, \theta, t), p(x, r, \theta, t + \tau) \rangle \exp(-i\omega\tau) d\tau = (\tilde{D}/2) \sum_{m=-\infty}^{\infty} \frac{|G(x, r; \omega, m)|^2}{|\zeta_1^p(0, r_{1/2}; \omega, m)|^2}, \quad (2-25)$$

and

$$G(x, r; \omega, m) = \int_{-\infty}^{\infty} \hat{g}(\eta; \omega, m) H_m^{(1)}[i\lambda(\eta)r] \exp(-i\eta x) d\eta. \quad (2-26)$$

By transforming the cylindrical coordinate system to a spherical coordinate system (R, ψ, θ) , $x = R \cos \psi$ and $r = R \sin \psi$, and applying the stationary phase approximation method to evaluate G at large R [18], Eqn. (2-25) is simplified to

$$\tilde{S}(R, \psi, \theta, f) = 10 \log_{10} \left[\frac{\rho_j^2 u_j^3 R_j^3}{p_{\text{ref}}^2 R^2} \sum_{m=-\infty}^{\infty} \frac{8\pi \tilde{D} |\hat{g}(\bar{\eta}; \omega, m)|^2}{|\zeta_1^P(0, r_{1/2}; \omega, m)|} \right], \quad (2-27)$$

and

$$\bar{\eta} = \frac{\bar{\rho}_{\infty}^{0.5} M_j \omega \psi}{(1 - M_{\infty}^2)(1 - M_{\infty}^2 \sin^2 \psi)^{0.5}} - \frac{\bar{\rho}_{\infty} M_j^2 \bar{u}_{\infty} \omega}{1 - M_{\infty}^2},$$

where \tilde{S} is the noise power spectrum in decibels, $f(\omega = 2\pi f)$ is frequency, $p_{\text{ref}} = 2 \times 10^{-5}$ Pa is the reference pressure, $\bar{\eta} = \bar{\eta}(\psi)$ is the stationary phase where limiting $0^\circ \leq \psi \leq 180^\circ$ denotes the direction from the upstream nozzle centerline axis, and $M_{\infty} = \bar{\rho}_{\infty} M_j^2 \bar{u}_{\infty}^2$.

Numerical Implementation

To compute the broadband spectrum of jet noise (Eqn. (2-27)) from instability waves, three unknowns, α , $|\zeta_1^P(0, r_{1/2}; \omega, m)|$, and \hat{g} , should be determined firstly. Equation (2-12) can be used to obtain the wavenumber α and $|\zeta_1^P(0, r_{1/2}; \omega, m)|$. The term \hat{g} (Eqn. (2-20)) is computed via the fast Fourier transform (FFT) method if the term β is neglected.

Firstly, we solve Eqn. (2-12) numerically due to the finite thickness of the shear layer [146]. We rewrite Eqn. (2-12) and change the eigenvalue from α to a new variable $c = c_r + ic_i = \omega/\alpha$ to confine the range of eigenvalue in the complex c plane

$$\frac{\partial^2 \hat{p}_0}{\partial r^2} + \left[\frac{1}{r} + \frac{2}{\bar{c}} \frac{\partial \bar{u}}{\partial r} - \frac{1}{\bar{\rho}} \frac{\partial \bar{\rho}}{\partial r} \right] \frac{\partial \hat{p}_0}{\partial r} + \left[\bar{\rho} M_j^2 \left(\frac{\omega}{\alpha} \right)^2 \bar{c}^2 - \frac{m^2}{r^2} - \left(\frac{\omega}{\alpha} \right)^2 \right] \hat{p}_0 = 0, \quad (2-28)$$

where $c = \omega/\alpha$, $c = c_r + ic_i$, and $\bar{c} = c - \bar{u}$. Given any real ω , the real part, c_r is within or nears the bounds set by the real mean velocity \bar{u} , which makes c is easily obtained due to its boundedness.

In this study, the global method via central finite difference method to discretize the Eqn. (2-12)

by Dahl [99] is adopted. The discrete equation can be rearranged in a tridiagonal form as

$$\left[1 - \frac{1}{2}Z_{1k}\Delta r\right]\hat{p}_{k-1} + [Z_{0k}\Delta r^2 - 2]\hat{p}_k + \left[1 + \frac{1}{2}Z_{1k}\Delta r\right]\hat{p}_{k+1} = 0, \quad (2-29)$$

where

$$Z_{1k} = \left[\frac{1}{r} + \frac{2}{c - \bar{u}} \frac{\partial \bar{u}}{\partial r} - \frac{1}{\bar{\rho}} \frac{\partial \bar{\rho}}{\partial r}\right]_k, \quad (2-30)$$

and

$$Z_{0k} = \left[\bar{\rho} M_j^2 \left(\frac{\omega}{c}\right)^2 (c - \bar{u})^2 - \frac{n^2}{r^2} - \left(\frac{\omega}{c}\right)^2\right]_k, \quad (2-31)$$

where the subscript k is the grid point of the flow-field.

The inner boundary condition is expressed in axisymmetric or non-axisymmetric form, as

$$\begin{aligned} \frac{\partial \hat{p}}{\partial r} &= 0 \quad \text{for } m = 0 \\ \hat{p} &= 0 \quad \text{for } m \neq 0. \end{aligned} \quad (2-32)$$

The outer boundary condition is

$$\hat{p}_{N+1} = \frac{H_m^{(1)}(i\lambda r_{N+1})}{H_m^{(1)}(i\lambda r_N)} \hat{p}_N. \quad (2-33)$$

The above Eqns. (2-28), (2-32), and (2-33) create a tridiagonal system of equations that can be written in the form

$$A(c)\hat{p} = 0. \quad (2-34)$$

The non-trivial solution only exists when the determinant of A is not equal to zero. The eigenvalue must be found at each axial location for a given frequency ω . The grid searching method is used to find the eigenvalue. Specifically, the value of $\det(A)$ can be expressed in a matrix form by setting up the grid matrix with the range of real and imaginary part of c . Contours of $\det(A)$ defining the zeros of imaginary and real part of $\det(A)$ cross at the position of the

eigenvalue. We chose the maximum growth rate if there are too many cross positions because the instability wave mode (Kelvin-Helmholtz mode) is most unstable and dominant [99]. The procedure to solve the corresponding solution implies that the solution is actually located in the amplifying region, where the imaginary part of eigenvalue, $c_i > 0$. However, the critical effect, critical layer or point (r_c), must be taken into account for the damped region where the imaginary part of eigenvalue is negative, $c_i < 0$.

The critical point is defined where $\bar{c}(\bar{r}_c) = 0$. The contour deformation method is applied to solve the problem. Body [147] demonstrates a number of complex mapping techniques to solve the hydrodynamic problems with small or zero decay rates. In this proposal, a simple box path around r_c , as shown in Fig. 2-2, is used [99]. The parameters \bar{u} and $\bar{\rho}$ in Eqn. (2-28) can be determined easier along the path for using simulation results directly.

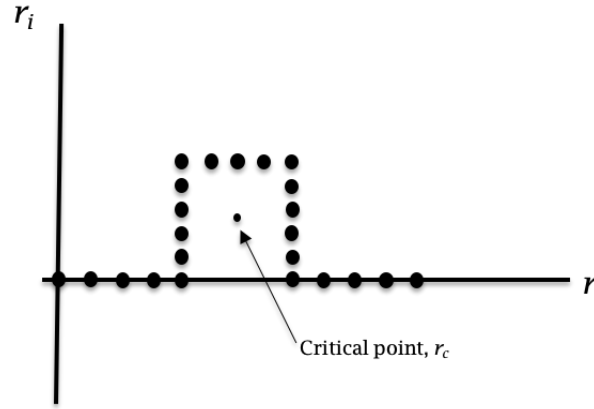


Figure 2-2. Box path of the contour mapping.

The direction of the contour into the complex r -plane is determined by the derivative of the mean velocity profile. For $\partial \bar{u} / \partial r \geq 0$, the critical point of the damping mode lies in the upper half plane, therefore, the contour for damped waves must go into the upper half plane and around the critical point to prevent the solution going to infinity [99, 147] and vice versa. The matrix form of $\det(A)$ is reconstructed via the rule from Dahl [99]. Then the eigenvalue that implies the damped wave is obtained with the grid searching method. After obtaining the eigenvalue, the eigenfunction of Eqn. (2-12) is computed via the Runge-Kutta method.

Next, the term \hat{g} will be computed. We neglect the non-parallel effect when calculating the sound spectrum of Eqn. (2-27). Then the wavenumber spectrum is

$$\hat{g}(\eta; \omega, m) = \frac{1}{2\pi} \int_{-\infty}^{\infty} \exp \left\{ \left[i \int_0^x \alpha(x; \omega, m) dx - \eta x \right] \right\} dx, \quad (2-35)$$

which can be regarded as the Fourier transform of instability waves. The FFT is used to calculate the Eqn. (2-35). The trapezoidal rule is applied to compute the term $\phi(x) = \int_0^x \alpha(x; \omega, m) dx$

$$\phi_j = \phi_{j-1} + \frac{1}{2}(\alpha_j + \alpha_{j+1})(x_{j+1} - x_j), \quad (2-36)$$

where $\phi_0 = 0$ and the subscript j is the node number in the streamwise direction.

The wavenumber spectrum of the instability wave is given by

$$\hat{g}(\eta_n; \omega, m) = \sum_{j=0}^{N-1} \exp(i\phi_j) e^{-i2\pi n j/N} = \frac{\Delta x}{2\pi} \text{FFT}\{\exp(i\phi_j)\}, \quad (2-37)$$

where

$$\eta_n = \begin{cases} n\Delta\eta & \text{for } 0 \leq n \leq N/2 - 1 \\ (n - N)\Delta\eta & \text{for } N/2 \leq n \leq N - 1 \end{cases} \quad (2-38)$$

and

$$\Delta\eta = \frac{\Delta x}{2\pi}. \quad (2-39)$$

2.1.2 Detection of Instability Waves

2.1.2.1 Least-Square Matching

In the previous analysis of instability wave theory, the rate of growth or decay and phase dynamics of instability waves for a slowly varying mean flow-field have been predicted, however, the complex amplitude $\hat{A}_0(m, \omega)$ is still unknown. The value of \hat{A}_0 should be properly determined due to its importance on analyzing the actual contributions of the instability wave modes to the real jet noise intensity.

Suzuki and Colonius [82] detected the instability waves via a modified beam forming method to match the results of linear stability analysis with the measurements of a conic array of microphones, where the modified beam forming method is applied to find the amplitudes of instability waves. Ryu [2] showed the kinetic energy matching method to find the amplitude of PSE predictions at two different probes. Sinha [98] showed that the amplitude of PSE predictions can be estimated by comparing with the first mode of POD results. We will apply the method from Sinha [98] to find \hat{A}_0 by matching the instability wave solution with the results from LES and the reconstructed flow-field with POD modes.

Firstly, we have to decompose the results from LES. The flow-field variables, $\mathbf{q} = [\rho, u, v, w, p]$, from the simulation results can be decomposed as

$$\mathbf{q}(x, r, \theta, t) = \bar{\mathbf{q}}(x, r) + \mathbf{q}'(x, r, \theta, t), \quad (2-40)$$

where $\bar{\mathbf{q}}(x, r)$ is the mean value defined as an average over the azimuthal direction and time, and \mathbf{q}' is the flow variables perturbations.

We introduce the Fourier decomposition of flow perturbation variables to obtain the modulus and phase at each at each frequency ω_n and azimuthal mode number m , as

$$\mathbf{q}'(x, r, \theta, t) = \sum_{n=-N_t/2}^{N_t/2-1} \sum_{m=-N_\theta/2}^{N_\theta/2-1} \hat{\mathbf{q}}_{mn}(x, r) \exp(i(m\theta - \omega_n t)), \quad (2-41)$$

where N_t is the total number of frequencies, N_θ is the total number of azimuthal modes, and $\hat{\mathbf{q}}_{mn}(x, r)$ is the Fourier coefficients.

As previous stated, a probe needs to be selected for the matching process. We can express the decomposed pressure from LES (Π_l^L) and instability waves (Π_l^P) at the probe location as

$$\Pi_l^L = \hat{p}_{mn}(x_l, r_l), \quad (2-42)$$

and

$$\Pi_l^P = \zeta_1^P(x_l, r_l) e^{i \int_{x'=x_o}^{x'=x_l} \alpha_{mn}(x') dx'}, \quad (2-43)$$

where the subscript is the l^{th} point in the probe location.

We consider the square norm of the difference between Π_l^P and Π_l^L and define the following cost function,

$$J(\hat{A}_0) = \sum_{l=1}^N |\hat{A}_0 \Pi_l^P - \Pi_l^L|^2, \quad (2-44)$$

where N is the number of points of the probe where LES data collected.

With the LES data at the probe locations as the target solution and eigenfunction from the instability wave theory as a reference solution, the phase matched complex amplitude for the instability wave models can be computed. Optimal complex amplitude coefficients \hat{A}_0 , which minimizes J satisfies $\frac{\partial J}{\partial \hat{A}_0} = 0$ and expressed as

$$\hat{A}_0 = \frac{\sum_{l=1}^N \Pi_l^{P*} \Pi_l^L}{\sum_{l=1}^N \Pi_l^{P*} \Pi_l^P}, \quad (2-45)$$

where the asterisk represents the complex conjugate.

2.1.2.2 Proper Orthogonal Decomposition

The POD method uses data to generate a set of basis functions that optimally represent the flow's energy based on a user-selected norm. The POD is a promising and widely applied method used to identify coherent structures and characterize flow structures in turbulence. The selected POD modes can be used in modeling by either providing for phenomenological models or generating a reduced-order model via projection onto the governing equations [71].

This procedure is equivalent to solve the following eigenvalue problem

$$\int \int C(\mathbf{x}, \mathbf{x}'; t, t') W(\mathbf{x}') \phi(\mathbf{x}', t') d\mathbf{x}' dt' = \lambda \phi(\mathbf{x}', t'), \quad (2-46)$$

where

$$C(\mathbf{x}, \mathbf{x}'; t, t') = E\{\mathbf{q}(\mathbf{x}, t)\mathbf{q}^*(\mathbf{x}', t')\}, \quad (2-47)$$

is the cross-correlation tensor of input vector data $\mathbf{q}(\mathbf{x}, t)$, W is weight function, $E\{\cdot\}$ represents the ensemble average over different realizations of the flow and λ is the eigenvalue, which represents the average amount of energy captured by the corresponding mode $\phi(\mathbf{x}, t)$ or the eigenvector.

It has proven that Eqn. (2-46) can be expressed based on frequency component and azimuthal mode as

$$\int \int S(\mathbf{x}, \mathbf{x}'; f, m) W(\mathbf{x}') \psi(\mathbf{x}', f') d\mathbf{x}' = \lambda(f, m) \psi(\mathbf{x}', f', m'), \quad (2-48)$$

where

$$S(\mathbf{x}, \mathbf{x}'; f, m) = E\{\hat{\mathbf{q}}(\mathbf{x}, f, m) \hat{\mathbf{q}}^*(\mathbf{x}', f', m')\}, \quad (2-49)$$

where S is cross-spectrum tensor, and $\hat{\mathbf{q}}$ is the Fourier transform of \mathbf{q} on time and azimuthal direction.

We follow the method of Towne et al. [148], which has a similar procedure used by Citriniti [149] but with an additional simplification that reduces the computational cost in most cases. Firstly, the input data are expressed in matrix form as

$$\mathbf{Q} = [\mathbf{q}_1 \quad \mathbf{q}_2 \quad \dots \quad \mathbf{q}_N] \in R^{M \times N}, \quad (2-50)$$

where each column represents a snapshot of the flow-field and N snapshots are sampled with step size Δt . The data is then segmented into partially overlapping blocks.

Next, the DFT is computed for each block

$$\hat{\mathbf{Q}} = [\hat{\mathbf{q}}_1 \quad \hat{\mathbf{q}}_2 \quad \dots \quad \hat{\mathbf{q}}_N]. \quad (2-51)$$

The cross-spectral density matrix at frequency f_k is calculated using

$$S_{f_k} = \frac{1}{(\sum_{j=1}^{N_f} w_j^2) N_f N_b} \sum_{l=1}^{N_b} \hat{\mathbf{q}}_k^{(l)} \hat{\mathbf{q}}_k^{(l)*}, \quad (2-52)$$

where N_b is the total number of blocks and w_j is the window function added in each block which can be used to reduce spectral leakage due to the non-periodicity of the data.

Then, Eqn. (2-51) can be rewritten as a new data matrix

$$\hat{\mathbf{Q}} = \sqrt{\frac{1}{N_f \sum_{j=1}^{N_f} w_j^2}} [\hat{\mathbf{q}}_k^{(1)} \quad \hat{\mathbf{q}}_k^{(2)} \quad \dots \quad \hat{\mathbf{q}}_k^{(N_b)}] \in R^{M \times N_b}. \quad (2-53)$$

The spectral density, Eqn. (2-52), becomes

$$S_{f_k} = \frac{1}{N_b} \hat{\mathbf{Q}}_{f_k} \hat{\mathbf{Q}}_{f_k}^*. \quad (2-54)$$

Finally, the infinite-dimensional eigenvalue problem reduces to an matrix ($N \times N$) eigenvalue problems

$$S_{f_k} W \Psi_{f_k} = \Psi_{f_k} \Lambda_{f_k}, \quad (2-55)$$

where W accounts for both the weight $W(x)$ and the numerical quadrature of the integral on the discrete grid, Ψ_{f_k} is unitary matrix, of which the columns are POD modes, and Λ_{f_k} is a diagonal matrix with eigenvalues corresponding to the extracted modes ranked in descending order. In practice, the number of blocks N_b is typically much smaller than the discretized problem size N .

The flow-field can be reconstructed by the summation of eigenfunctions multiplied by the corresponding coefficients a_{f_k}

$$q(x, r, \theta, t) = \sum_m \sum_{j=1}^{N_f} \sum_n a_{f_k}^n \Psi_{f_k}^n \exp(i(m\theta - 2\pi f_k^{(j)} t)), \quad (2-56)$$

and

$$a_{f_k}^* = (\sqrt{W} \hat{\mathbf{Q}}_{f_k})^H (\Psi_{f_k} \sqrt{W}). \quad (2-57)$$

Furthermore, the POD results will depend on the selected norm [71]. The POD results for a 3D turbulent flow based on five norms are compared, which shows that the different number of POD modes are needed for reconstructing the same flow-fields [71]. Some POD modes based on pressure perturbations norm that look like a wave packet, similar to a growing and decaying instability wave [150]. The POD results of a streamwise velocity norm show that there are also other higher azimuthal modes ($m = 5$) having higher energy than the axisymmetric mode [149].

2.1.3 Kirchhoff Surface Method

In this section, the derivation and solution of the Kirchhoff surface method by Freund [151] will be reviewed. The acoustic disturbances can be described by the linearized, inviscid wave equation when the viscous attenuation and non-linear effects are minimal and can be neglected due to the mean velocity and its gradients are sufficiently small. The wave equation for pressure fluctuation for within a quiescent medium is

$$\left[\frac{1}{c_\infty^2} \frac{\partial^2}{\partial t^2} - \nabla^2 \right] p' = 0. \quad (2-58)$$

Bodony and Lele [68] indicated there are two equivalent methods that have been employed for jet noise computation. The first is to apply the Green's function. The solution for stationary and moving surfaces are given by Farassat and Myers [15]. Brentner and Farassat [75] also gave the solution and showed that the noise components terms of the Kirchhoff equations are equivalent with the FWH equation. The other is from Freund [151] via transforming coordinates for a Kirchhoff surface S of radius R_s along the jet axis. The Kirchhoff surface as in Fig. 2-3 (modified from [152]) should be far away enough from the hydrodynamic region of the jet and enclose all the nonlinear effects so that the generating noise can be described by Eqn. (2-58).

The partially transformed form of Eqn. (2-58) outside of the surface S is

$$\left(\frac{d^2}{dr^2} + \frac{1}{r} \frac{d^2}{dr^2} + \frac{\omega_n^2}{c_\infty^2} - k_x^2 - \frac{m^2}{r^2} \right) \hat{p}_{mn}(k_x, r) = 0, \quad (2-59)$$

where k_x is the wavenumber along the streamwise direction, and $\hat{p}_{mn}(k_x, r)$ is the fluctuating pressure with Fourier transform in x , θ and t .

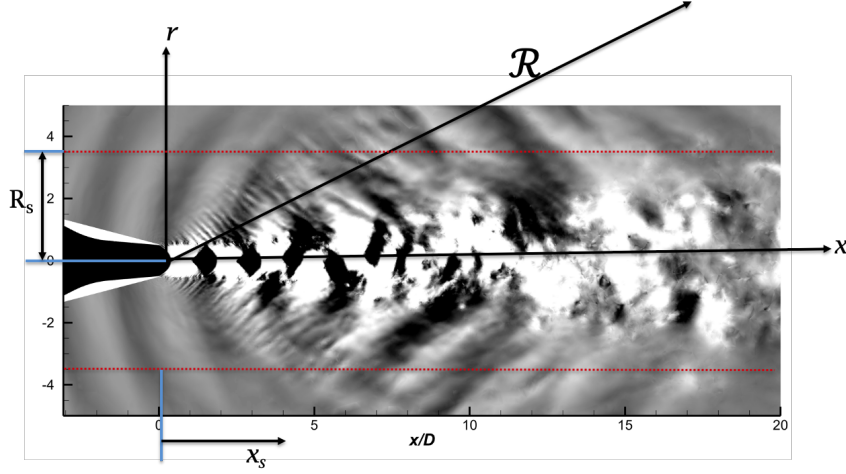


Figure 2-3. Kirchhoff surface location.

The exact solution [153] in cylindrical coordinates is

$$p'(x, r, \theta, t) = \frac{1}{2\pi} \int_{-\infty}^{\infty} \sum_{n=-N_t/2}^{N_t/2-1} \sum_{m=-N_\theta/2}^{N_\theta/2-1} \hat{p}_{mn}(k_x, R_s) T_m^{(j)} \exp(i(k_x x + m\theta - \omega_n t)) dk_x, \quad (2-60)$$

where $T_m^{(j)}$ depends on the value of $\omega_n^2/c_\infty^2 - k_x^2$ and m . $T_m^{(j)}$ can be expressed as

$$T_m^{(j)} = \begin{cases} \frac{H_m^{(j)}(r\sqrt{\omega_n^2/c_\infty^2 - k_x^2})}{H_m^{(j)}(R_s\sqrt{\omega_n^2/c_\infty^2 - k_x^2})} & \omega_n^2/c_\infty^2 - k_x^2 > 0 \\ \frac{R_s^{|m|}}{r^{|m|}} & \omega_n^2/c_\infty^2 - k_x^2 = 0 \quad \text{and} \quad m \neq 0 \\ 1 & \omega_n^2/c_\infty^2 - k_x^2 = 0 \quad \text{and} \quad m = 0 \\ \frac{K_m(r\sqrt{\omega_n^2/c_\infty^2 - k_x^2})}{K_m(R_s\sqrt{\omega_n^2/c_\infty^2 - k_x^2})} & \omega_n^2/c_\infty^2 - k_x^2 < 0, \end{cases} \quad (2-61)$$

where $j = 1$ for $\omega_n > 0$ and $j = 2$ for $\omega_n < 0$ to enforce the outgoing acoustic wave the term $H_m^{(j)}$.

Near $r = R_s$, the non-radiating components may affect the pressure field. For the far-field, only those waves that satisfy $\omega_n^2/c_\infty^2 - k_x^2 > 0$ radiate as sound. Therefore, the stationary phase method [154] is applied to compute Eqn. (2-60). Finally, the solution in the spherical coordinate system is

$$p'(R, \psi, \theta, t) = \sum_{m=-N}^N \left(\sum_{n=0}^{N_t/2-1} \hat{p}_{mn}(k_n \cos \psi, R_s) \frac{\exp(ik_n R (-i)^{m+1})}{\pi R H_m^{(1)}(R_s k_n \sin \psi)} \exp(i(m\theta - \omega_n t)) + \sum_{n=-N_t/2}^0 \hat{p}_{mn}(k_n \cos \psi, R_s) \frac{\exp(ik_n R (i)^{m+1})}{\pi R H_m^{(2)}(-k_n R_s \sin \psi)} \exp(i(m\theta - \omega_n t)) \right), \quad (2-62)$$

where the stationary phase is $k_x = \omega_n / c_\infty \cos \psi$, $k_n = \omega_n / c_\infty$, and $N \approx k_x R_s \sin \psi$. Only selected wavenumbers can propagate to the far-field, and they are dependent on the radial frequency, radiation angle from the jet exit, and azimuthal number. The conditions are $k_x = \omega_n / c_\infty \cos \psi$ and $m \leq k_x R_s \sin \psi$.

2.1.4 Correlation and Coherence

Correlation analysis have been applied and proven to be a useful tool in jet noise sources and characteristics studies [50, 155, 59, 27]. The results of correlation studies based on experimental results indicate that pressure-field measurements characteristics can provide insights into source characteristics, such as for the two sources theory of jet noise: fine- and large-scale noise sources and the spatio-temporal relation of acoustic field.

Correlation can be used more easily to identify waveform periodicity and to obtain spatiotemporal length scales and phase speeds. On the other hand, coherence [156, 59] is useful for extracting the spatial phase relations of the field as a function of frequency, which can be used to illustrate the features seen in the broadband cross-correlation analysis.

The correlation between two waveforms is defined as

$$R_{mn}(\tau) = \frac{\langle p_m(t) p_n(t + \tau) \rangle}{\langle p_m^2(t) \rangle^{1/2} \langle p_n^2(t) \rangle^{1/2}}, \quad (2-63)$$

where $p_m(t)$ is the pressure time signal of the m^{th} microphone, $p_n(t)$ is the pressure time signal of the n^{th} microphone, and $\langle \rangle$ denotes the time-averaged quantity.

The coherence is defined as

$$\gamma_{mn}^2(f) = \frac{|G_{mn}(f)|^2}{G_{mm}(f) G_{nn}(f)}, \quad (2-64)$$

where $G_{mn}(f)$ is the cross-spectra density between the m^{th} and n^{th} microphones, and $G_{mm}(f)$ and $G_{nn}(f)$ is the auto-spectra density of the m^{th} and n^{th} microphone.

2.2 Methodology for Boundary Layer Flows

2.2.1 Linear Stability Theory

We use LST to predict the unstable modes within the boundary layer that develops within supersonic flows. We assume that the flow is governed by the Navier-Stokes equations, energy equation, and ideal gas law. These equations and overall method are discussed in Malik and Spall [45]. The equations governing the flow of a viscous compressible ideal gas include the continuity equation

$$\frac{\partial \rho}{\partial t} + \nabla \cdot (\rho \mathbf{V}) = 0, \quad (2-65)$$

the momentum equation

$$\rho \left[\frac{\partial \mathbf{V}}{\partial t} + (\mathbf{u} \cdot \nabla) \mathbf{V} \right] = -\nabla p + \nabla \cdot [\lambda (\nabla \cdot \mathbf{V}) \mathbf{I}] + \nabla \cdot [\mu (\nabla \mathbf{V} + \nabla \mathbf{V}^{tr})], \quad (2-66)$$

the energy equation

$$\rho c_p \left[\frac{\partial T}{\partial t} + (\mathbf{V} \cdot \nabla) T \right] = \nabla \cdot (k \nabla T) + \frac{\partial p}{\partial t} + (\mathbf{V} \cdot \nabla) p + \Phi, \quad (2-67)$$

and the ideal gas law

$$p = \rho RT. \quad (2-68)$$

Here, $\mathbf{V} = (u, v, w)$ is the velocity vector, k is the thermal conductivity, μ is the first coefficient of viscosity, $\Phi = \lambda (\nabla \cdot \mathbf{V}) + \mu [\nabla \mathbf{V} + \nabla \mathbf{V}^{tr}]^2 / 2$ is the viscous dissipation, and λ is the second coefficient of viscosity. The perturbation equations that govern the instability waves are derived from the linearized Eqs. (2-66) to (2-68) in non-dimensional form. All lengths are scaled by viscous length $l = (\nu_e^* x^* / u_e^*)^{1/2}$. Here, ν_e^* is the dimensional viscosity at the boundary layer edge, where the definition of boundary layer edge values depends on the specific flow conditions.

Velocities are scaled by u_e^* , density by ρ_e^* , pressure by $\rho_e^* u_e^{*2}$, time by l/u_e^* , and other variables by their corresponding values at the boundary layer edge position. The instantaneous values of the field variables and parameters in Eqs. (2-66) to (2-68) can be expressed as the sum of a mean and a fluctuation quantity

$$\begin{aligned} u &= \bar{u} + u', & v &= \bar{v} + v', & w &= \bar{w} + w', \\ p &= \bar{p} + p', & T &= \bar{T} + T', & \rho &= \bar{\rho} + \rho', \\ \mu &= \bar{\mu} + \mu', & \lambda &= \bar{\lambda} + \lambda', & k &= \bar{k} + k'. \end{aligned} \quad (2-69)$$

In this study, we consider the flow over a cone, which is an axisymmetric body at zero incidence. The body-fitted orthogonal curvilinear coordinates x , y , and z are used, where x is the streamwise coordinate along the cone surface, y is the coordinate normal to the surface, and z is the azimuthal direction, as shown in Fig. 2-4.

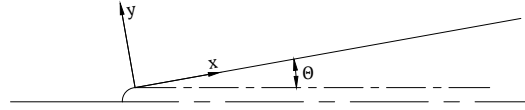


Figure 2-4. Body-fitted orthogonal curvilinear coordinates.

The scale factors are determined via coordinate transformations and are defined as

$$h_1 = 1 + \kappa(x)y; \quad h_2 = 1; \quad h_3 = r_0(x) + y \cos(\theta), \quad (2-70)$$

where $\kappa = -\frac{d\theta}{dx}$ is local body curvature, θ is the half-angle of the cone, and $r_0(x) = x \cos(\theta)$.

The curvature coefficients are

$$m_{13} = \frac{1}{h_1} \frac{\partial h_1}{\partial y}; \quad m_{21} = \frac{1}{h_1 h_2} \frac{\partial h_2}{\partial x}; \quad m_{23} = \frac{1}{h_2} \frac{\partial h_2}{\partial y}. \quad (2-71)$$

Here, $m_{13} = 0$ is the streamwise curvature for cone cases, m_{21} is related to body divergence due to increase in the body radius, and m_{23} represents transverse curvature effect.

For cone geometries, m_{21} and m_{23} are

$$m_{21} = \frac{d(\ln r)/dx}{1 + \epsilon y} = \frac{l \sin \theta}{r(1 + \epsilon y)} \quad (2-72)$$

and

$$m_{23} = \frac{\epsilon}{1 + \epsilon y}, \quad (2-73)$$

where $\epsilon = l \cos(\theta)/r$.

We assume that the flow is locally parallel within the boundary layer on the cone surface to simplify the LST prediction. Specifically, we assume that the gradients of the mean flow in the streamwise direction and the mean vertical velocity are negligible. However, the numerical prediction of the mean flow-field does not make this assumption. Under these assumptions we set

$$\bar{u} = \bar{u}(y); \quad \bar{v} = 0; \quad \bar{T} = \bar{T}(y); \quad \bar{p} = \bar{p}(y); \quad \bar{\rho} = \bar{\rho}(y), \quad (2-74)$$

and

$$\bar{w}(y) = 0, \quad (2-75)$$

because of the axisymmetric nature of the time-averaged flow.

We also make a number of other minor simplifying assumptions. Firstly, due to the boundary layer assumption, pressure (\bar{p}) is constant across the layer and is equal to $1/(\gamma M_e^2)$, where $M_e = u_e^*/\sqrt{\gamma R T_e^*}$. The viscosity $\bar{\mu}$ is calculated using Sutherland's law. Sutherland's law is

$$\bar{\mu} = \bar{T}^{\frac{3}{2}} \frac{1 + C/T_\infty^*}{\bar{T} + C/T_\infty^*}, \quad (2-76)$$

where $C = 110.4$ K is a constant or effective temperature and T_∞^* represents the dimensional free-stream temperature. Moreover, $\tilde{\mu}$, $\tilde{\lambda}$, and \tilde{k} are related to temperature as

$$\mu' = \frac{d\bar{\mu}}{d\bar{T}} T', \quad \lambda' = \frac{d\bar{\lambda}}{d\bar{T}} T', \quad \text{and} \quad k' = \frac{d\bar{k}}{d\bar{T}} T'. \quad (2-77)$$

The disturbance amplitudes are assumed to be small enough so that they do not interact in a nonlinear fashion to avoid nonlinear effects. We assume that the solution of the instability waves can be expressed in the following form

$$\boldsymbol{\phi}'(x, y, z, t) = \hat{\boldsymbol{\phi}}'(y) \exp[i(\alpha x + \beta z - \omega t)], \quad (2-78)$$

which consists of a spatially varying function and an exponentially varying spatial periodic function. Here, $\boldsymbol{\phi}'$ is a five-element vector defined by $\{u', v', p', T', w'\}$, $\hat{\boldsymbol{\phi}}(y)$ is the shape function of each element vector, α and $\beta = nl/r$ (n is the azimuthal mode number) are the wavenumbers in the streamwise and spanwise directions, and $\omega = 2\pi f^* l / u_e^*$ is non-dimensional frequency. In general, α , β , and ω are complex numbers. In this paper, we focus on spatial stability and set ω and β as real numbers.

The compressible linear instability equations combining the above assumptions for boundary layer flow over a cone are

$$\begin{aligned} & \frac{d^2 \hat{u}}{dy^2} + (c_1 \bar{T}' + m_{23}) \frac{d \hat{u}}{dy} + i \alpha_0 l_1 \frac{d \hat{v}}{dy} + c_1 \bar{u}' \frac{d \hat{T}}{dy} \\ & + \left[\frac{i c_3 R_e}{\bar{\mu} \bar{T}} - l_2 \alpha_0^2 - \beta_0^2 + i \alpha_0 l_2 m_{21} - l_2 m_{21}^2 \right] \hat{u} + \left[i \alpha_0 (c_1 \bar{T}' + l_1 m_{23}) - \frac{R_e \bar{u}'}{\bar{\mu} \bar{T}} - l_2 m_{21}^2 \right] \hat{v} - \frac{i \alpha_0 R_e}{\bar{\mu}} \hat{p} \\ & + [c_1 (\bar{u}'' + m_{23} \bar{u}' + i \alpha_0 l_0 \bar{u} m_{21} - l_2 \bar{u} m_{21}^2) + c_2 \bar{u}' \bar{T}'] \hat{T} - [\alpha_0 \beta_0 l_1 + i \beta_0 l_3 m_{21}] \hat{w} = 0, \quad (2-79) \end{aligned}$$

$$\begin{aligned} & \frac{d^2 \hat{v}}{dy^2} + \frac{(i \alpha_0 + m_{21}) l_1}{l_2} \frac{d \hat{u}}{dy} + (c_1 \bar{T}' + m_{23}) \frac{d \hat{v}}{dy} - \frac{R_e}{l_2 \bar{\mu}} \frac{d \hat{p}}{dy} + \frac{c_1 \bar{u} m_{21} l_0}{l_2} \frac{d \hat{T}}{dy} + \frac{i \beta_0 (c_1 \bar{T}' l_0 - m_{23} l_3)}{l_2} \hat{w} \\ & + \frac{i \beta_0 l_1}{l_2} \frac{d \hat{w}}{dy} + [c_1 \bar{T}' (l_0 i \alpha_0 / l_2 + m_{21}) m_{21} m_{23}] \hat{u} + \left[\frac{1}{l_2} \left\{ \frac{i c_3 R_e}{\bar{\mu} \bar{T}} - \beta_0^2 + i \alpha_0 m_{21} + c_1 \bar{T}' m_{23} l_0 \right\} - m_{23}^2 \right] \hat{v} \\ & + \left[\frac{1}{l_2} \left\{ i \alpha_0 c_1 \bar{u}' + c_1 (\bar{u}' m_{21} l_1 - \bar{u} m_{21} m_{23}) + c_2 \bar{u}' \bar{T}' m_{21} l_0 \right\} - c_1 \bar{u} m_{21} m_{23} \right] \hat{T} = 0, \quad (2-80) \end{aligned}$$

$$\frac{d\hat{v}}{dy} + (i\alpha_0 + m_{21})\hat{u} + \left[m_{23} - \frac{\bar{T}'}{\bar{T}} \right] \hat{v} + \gamma M_e^2 (m_{21}\bar{u} - ic_3)\hat{p} - \left[\frac{m_{21}\bar{u} - ic_3}{\bar{T}} \right] \hat{T} + i\beta_0\hat{w} = 0, \quad (2-81)$$

$$\begin{aligned} & \frac{d^2\hat{T}}{dy^2} + c_4\bar{u}'\frac{d\hat{u}}{dy} + c_4\bar{u}m_{21}l_0\frac{d\hat{v}}{dy} + \left(2\frac{\bar{k}'}{\bar{k}} + m_{23} \right) \frac{d\hat{T}}{dy} \\ & + c_4[i\alpha_0\bar{u}m_{21}l_0 + \bar{u}m_{21}^2l_2]\hat{u} + \left[c_4(i\alpha_0\bar{u}' + \bar{u}m_{21}m_{23}l_0) - \frac{\sigma R_e\bar{T}'}{\bar{\mu}\bar{T}} \right] \hat{v} - \frac{ic_3c_4R_e}{2\bar{\mu}}\hat{p} \\ & + \left[\frac{ic_3R_e\sigma}{\bar{\mu}\bar{T}} - \beta_0^2 + i\alpha_0m_{21} + \frac{c_1c_4}{2}(\bar{u}'^2 + \bar{u}^2m_{21}^2l_2) + m_{23}\frac{\bar{k}'}{\bar{k}} + \frac{\bar{k}''}{\bar{k}} \right] \hat{T} + i\beta_0c_4\bar{u}m_{21}l_2\hat{w} = 0. \end{aligned} \quad (2-82)$$

and

$$\begin{aligned} & \frac{d^2\hat{w}}{dy^2} + i\beta_0l_1\frac{d\hat{v}}{dy} + (c_1\bar{T}' + m_{23})\frac{d\hat{w}}{dy} + (i\beta_0m_{21}l_3 - \alpha_0\beta_0l_1)\hat{u} + i\beta_0(c_1\bar{T}' + l_3m_{23})\hat{v} - \frac{i\beta_0R_e}{\bar{\mu}}\hat{p} \\ & + i\beta_0c_1\bar{u}m_{21}l_2\hat{T} + \left[\frac{R_e}{\bar{\mu}\bar{T}}(ic_3 - m_{21}\bar{u}) - l_2\beta_0^2 + i\alpha_0m_{21} - m_{21}^2 - m_{23}(c_1\bar{T}' + m_{23}) \right] \hat{w} = 0, \end{aligned} \quad (2-83)$$

where $()' \equiv d/dy$, $()'' \equiv d^2/dy^2$, $l_q = q + \lambda/\mu$, $\alpha_0 = \alpha/h_1$, $\beta_0 = \beta/h_2$, $R_e = \rho_e u_e l / \mu_e$ is Reynolds number, $\sigma = \mu c_p / k = 0.7$ is Prandtl number for this computation, and

$$c_1 = \frac{1}{\bar{\mu}} \frac{d\bar{\mu}}{d\bar{T}}, \quad c_2 = \frac{1}{d\bar{\mu}} \frac{d^2\bar{\mu}}{d\bar{T}^2}, \quad c_3 = -(\alpha\bar{u} - \omega), \text{ and } c_4 = 2(\gamma - 1)M_e^2\sigma. \quad (2-84)$$

The linear stability equations can be written as a system of equations as

$$\left(\mathbf{A} \frac{d^2}{dy^2} + \mathbf{B} \frac{d}{dy} + \mathbf{C} \right) \hat{\boldsymbol{\phi}} = 0, \quad (2-85)$$

where \mathbf{A} is a diagonal matrix and \mathbf{B} and \mathbf{C} are 5×5 matrices.

The boundary conditions at the wall and in the far-field are

$$\begin{aligned} y = 0; \quad \hat{\boldsymbol{\phi}}_1 = \hat{\boldsymbol{\phi}}_2 = \hat{\boldsymbol{\phi}}_4 = \hat{\boldsymbol{\phi}}_5 = 0, \\ y \rightarrow \infty; \quad \hat{\boldsymbol{\phi}}_1, \hat{\boldsymbol{\phi}}_2, \hat{\boldsymbol{\phi}}_4, \hat{\boldsymbol{\phi}}_5 \rightarrow 0. \end{aligned} \quad (2-86)$$

We seek to ascertain the instability wave solution represented by $\hat{\phi}$. First, we calculate the local wavenumber by solving the eigenvalue problem defined by Eqs. (2-85) through (2-86). There are two main methods to solve the discretized system. The first is the local method, and the second is the global method [45]. The global method yields all the eigenvalues of the discretized system. Both methods require that the equations be discretized by the finite difference method [44, 45] or a spectral approach [45]. The problem is then reduced to a linear algebraic system. Four different schemes and detailed analyses were introduced to discretize the system of equations [45]. In this study, the global method via finite difference is adapted.

2.2.2 Cross-Power Spectral Density of Pressure from Instability Waves

We can directly predict the wall pressure field from the instability waves based on the solution of Eq. (2-85) at multiple axial positions on the cone surface. We choose the most amplified instability waves in the azimuthal direction as the source of the driving force [157]. Equation (2-78) represents the form of a single instability wave. However, in high Reynolds number high-speed flow, there is a wide spectrum of instability waves [18]. As a linear theory is adapted, we superimpose solutions to obtain contributions from multiple waves. The pressure fluctuations field from instability waves can be constructed via integration over ω as

$$p'(\mathbf{x}, t) = \int_{-\infty}^{\infty} \hat{p}(y) \exp[i(\alpha x + \beta z - \omega t)] d\omega. \quad (2-87)$$

Here, the instability wave solution with angular frequency $-\omega$ and azimuthal wavenumber $-\beta$ is related to the solution with positive frequency ω and wavenumber β (see [100, 18]). For example, the relation for eigenvalue (α) is $\alpha(\mathbf{x}, -\omega, -\beta) = -\alpha^*(\mathbf{x}, \omega, \beta)$, where the asterisk denotes the complex conjugate. We do not focus on the overall amplitudes of the predicted instability waves. Scaling the solution results in another solution.

The spatial coherence of pressure fluctuations from instability waves is calculated via

$$\Gamma_{pp}(\boldsymbol{\xi}, \omega) = \frac{1}{2\pi} \int_{-\infty}^{\infty} \langle p'(\mathbf{x}, t) p'(\mathbf{x} + \boldsymbol{\xi}, t + \tau) \rangle \exp(-i\omega\tau) d\tau, \quad (2-88)$$

where $\boldsymbol{\xi}$ is the spatial separation vector.

Furthermore, in a typical vibration-acoustic problem of TBL flows, the semi-empirical models, such as the Corcos model [37] and modified Corcos model [29], have been proposed to express the excitation from pressure fluctuations within TBL flows. Such models can be modeled in terms of a point pressure spectrum term multiplied by a spatial expression [34] as

$$\Psi_{pp}(\xi, \omega) = \phi(\omega)\Gamma_{pp}(\xi, \omega), \quad (2-89)$$

where $\phi(\omega)$ is the single-point wall pressure fluctuation spectrum.

2.2.3 Phenomenological Model of Plasma Actuators

The Navier-Stokes equations can be expressed in differential form [158] as

$$\mathcal{R}(U) = \frac{\partial U}{\partial t} + \nabla \cdot \bar{F}^c(U) - \nabla \cdot \bar{F}^v(U, \nabla U) - S = 0, \quad (2-90)$$

where the conservation variables are $U = \{\rho, \rho \bar{V}, \rho E\}$, \bar{F}^c and \bar{F}^v are the convective and viscous fluxes, respectively, and S is a generic source term. Under the plasma actuator conditions, $S = \{0, \bar{F}, \bar{F} \cdot \bar{V} + S_v\}$, where $\bar{F} = (f_x, f_y, f_z)$ is the body force vector and S_v is the volume heating source term generated by plasma actuators.

Phenomenological models of dissipative heating was considered, and the effect on the flow was evaluated [137]. The volumetric heating model had the form

$$S_v = \frac{Q}{\pi^{3/2}a^3} \exp\left(-\frac{d^2}{a^2}\right), \quad (2-91)$$

where $d = \sqrt{(x - x_c)^2 + (y - y_c)^2 + (z - z_c)^2}$ is the distance from the center (x_c, y_c, z_c) of the heating source, Q is the total energy exerted by the source term, and a is the radius of the source.

CHAPTER 3

JET NOISE PREDICTION AND DISCUSSION

In this chapter, jet aeroacoustics in two different configurations will be discussed and the focus will be on the noise generated from instability waves. The first configuration is a round convergent nozzle. The second configuration is a bi-conic nozzle. The two nozzles are with representative configurations and widely used in the industry area.

3.1 Results of SHJAR Case

3.1.1 Flow-Field Analysis

We first focus on the under-expanded hot supersonic jet from the SHJAR database [159]. The nozzle is the circular convergent small metal chevron number 000 (SMC000) designed by NASA Glenn Research Center. The geometry of the nozzle is shown in Fig. 3-1. The nozzle exit diameter is 0.0508 m with lip thickness of approximately 2.5% of the nozzle diameter. The fully-expanded Mach number is $M_j = 1.47$. The corresponding NPR and TTR are 3.514 and 3.2, respectively. The u_j is 762.39 m/s, and the Reynold number at the nozzle exit, Re_D , is 6.26×10^5 , respectively.

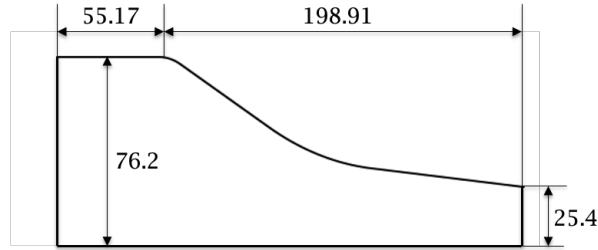


Figure 3-1. Axisymmetric view of SMC000 nozzle geometry with units in mm.

Figure 3-2 shows the results of mean axial velocity. The LES results [160] are compared with an axisymmetric Reynolds-averaged Navier-Stokes (RANS) equation simulation with the above jet operating conditions. The non-dimensional mean axial velocity from LES only has a small difference compared to RANS from the nozzle exit to $x/D = 7$. The mean axial velocity decays at same rate in RANS relative to the LES after $x/D = 7$. Similar decay between LES and RANS are observed by Georgiadis et al. [161]. The potential core length of LES is approximately $7.5D$, and that of RANS is approximately $10D$.

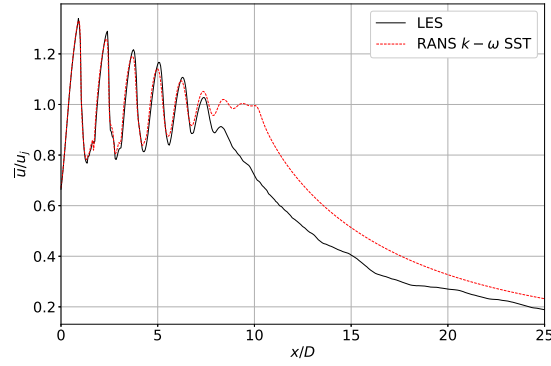


Figure 3-2. Comparison of mean axial velocity distribution between the LES and RANS simulation on the centerline.

An instantaneous pressure field of the LES [152] is shown in Fig. 3-3. At the nozzle exit, semi-periodic shock-cells are formed due to the pressure mismatch between the nozzle exhaust and ambient gas. It is observed that there are acoustic waves that propagate in the downstream and upstream directions in the near-field region. The parallel patterns in the downstream direction are the Mach wave radiation [22] caused by the large-scale turbulent structures, whereas the acoustic waves in the upstream direction are BBSAN [22].

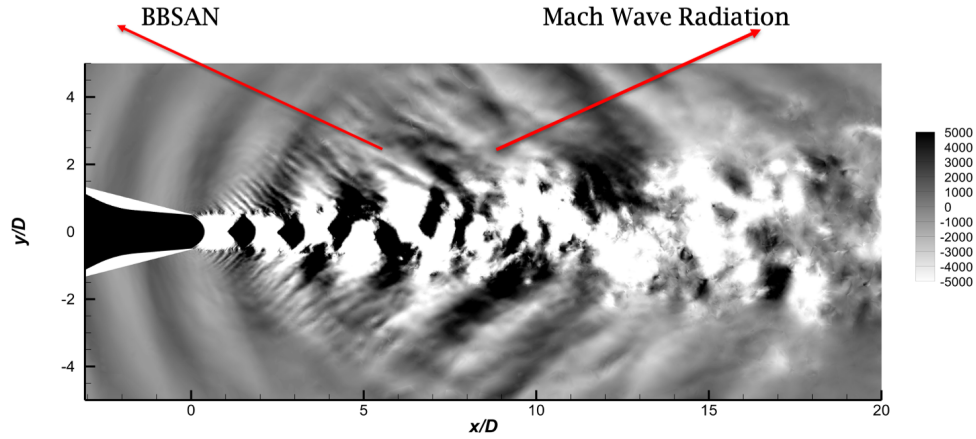


Figure 3-3. Instantaneous pressure contour ($p - p_\infty$) in Pa.

Frequency spectra of pressure perturbations of the LES data inside the shear layer at $r/D = 0.5$ and axial locations $x/D = 1, 4, 7$, and 10 for azimuthal modes $m = 0$ to 3 are shown in Fig. 3-4. These azimuthal modes are selected because they capture large amount of energy. These

locations correspond to the near jet exit, the middle of core region, the end of potential core region, and the fully developed region, which are representative.

The frequency spectra is dominated by the frequency near $St = 0.2$ at $m = 1$ for different axial locations, which are apparent at $x/D = 1$. The feed-back mechanism instigates strong instability waves at this particular frequency and corresponding harmonics [19]. These frequencies are most amplified in the jet by the instability waves [89] and are also captured by the LES. These instability modes correlate with noise radiated from the shear layer in the direction of the dominant radiation direction (see Mohseni [89]), which will provide more understanding and directions to examine specific frequencies for following linear instability modes.

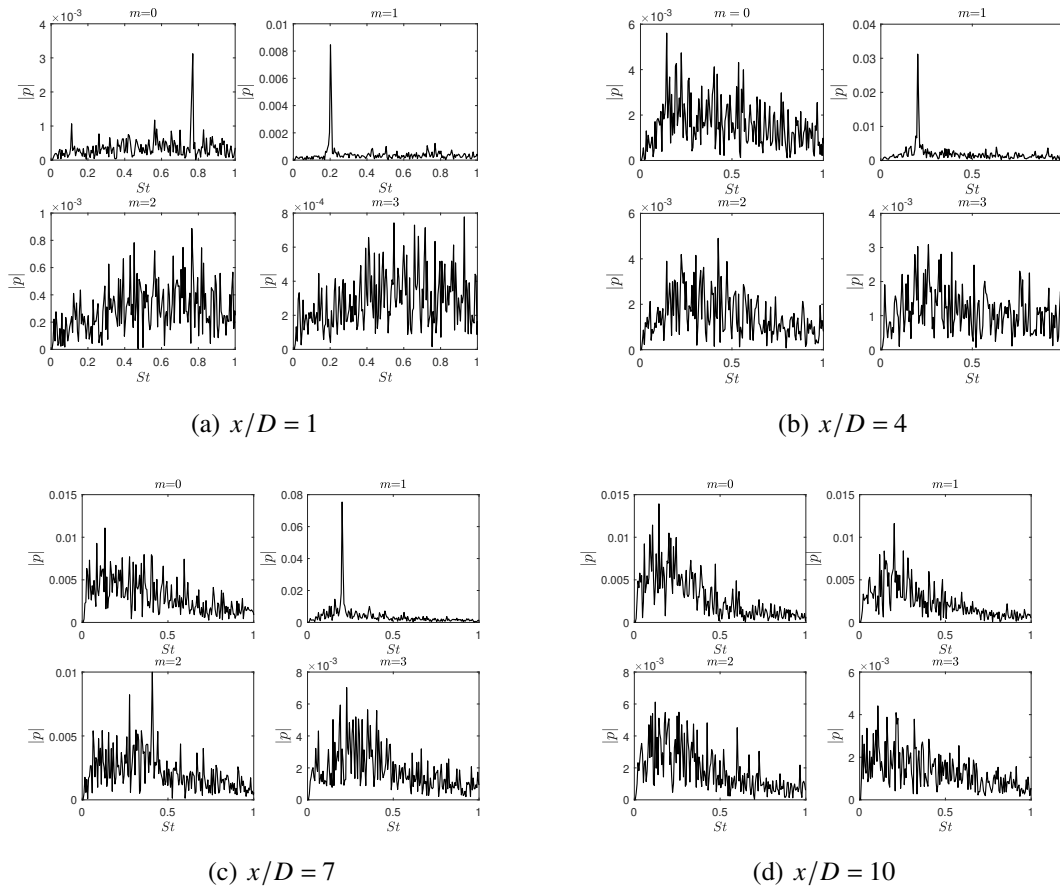


Figure 3-4. Frequency spectra of modal pressure perturbations of LES data at several axial positions in the jet shear layer at $r/D = 0.5$.

3.1.2 Instability Wave Detection

In this section, the properties of the instability waves are shown. The growth rate and phase speed at distinct St and streamwise direction are obtained firstly. The shape functions associated with instability waves in the radial and streamwise directions are presented. Finally, the amplitudes of the instability waves are determined via matching with the LES dataset. The pressure field is constructed from particular POD modes.

3.1.2.1 Stability Analysis

The mean velocity and density are required to evaluate the Rayleigh equation (Eqn. 2-12 with $n = 0$). Figure 3-5 shows the velocity and density component along the radial direction at different axial positions. It can be seen that the velocity will decay sharply outside the jet in the core region. At the end of the core and the transitional regions where $x/D > 7$, it is observed that the mean streamwise velocity starts to spread slowly. Similar trends are also observed for density, which is expected. The normalized velocity and density of $x/D = 1$ and 4 are above and below the fully expanded values within the results near the centerline. This is because the existence of shock cell structure in the potential region.

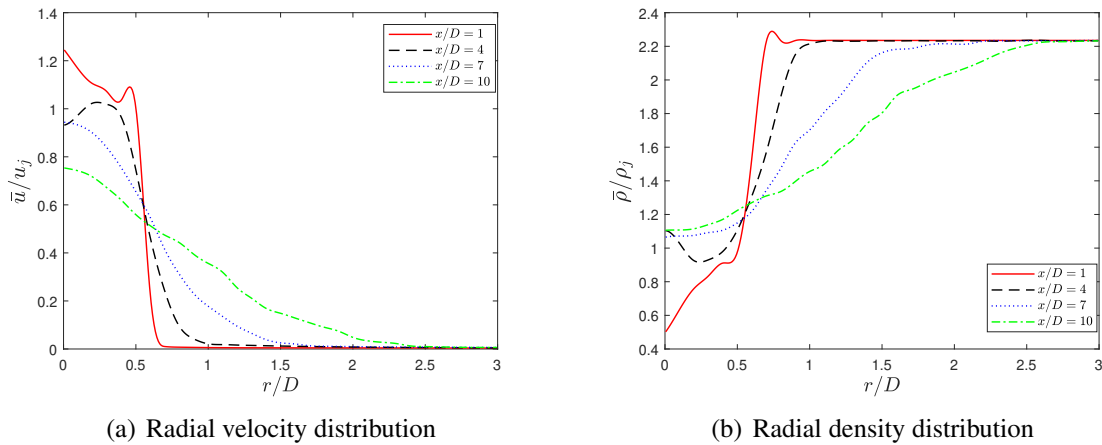


Figure 3-5. Variation of the streamwise velocity component and density in the radial direction at different axial locations from the LES.

Figure 3-6 presents the phase speed and growth rate for $0 < St < 0.6$ with $\Delta St = 0.05$ for different azimuthal modes at $x/D = 2.5$. For different azimuthal modes, the phase speeds have

similar trend which decreases firstly and then start to increase. Generally, the growth rate is relatively small at lower and higher St . The peak value of growth rate is near $St \sim 0.2$. This phenomenon is consistent with the changes of spectra of pressure perturbations (Fig. 3-4), where the largest amount of energy are at around $St \sim 0.2$ and the energy at the higher St are relatively low. Also, it is very close to the peak magnitude of large scale structure jet noise radiation.

Figure 3-7 shows the phase speed and growth rate in the streamwise direction at $St = 0.2006$ for $m = 0, 1$, and 2 . The analysis is initiated from $x/D = 0.1$, which is the left boundary of the sampling region of the LES. The phase speeds exhibit strong oscillations inside the potential core region and begin to decay sharply behind the potential core region. This phenomenon reflects that the instability wave extracts the energy from the mean flow and is similar to the mean flow variation in the core region. The phase speed of $m = 0$ is larger than other modes inside the potential core region. The initial growth rates for all modes peak on the initial axial plane and then decay with axial distance. However, the growth rates appear to contain a local increase near $x/D = 2$.

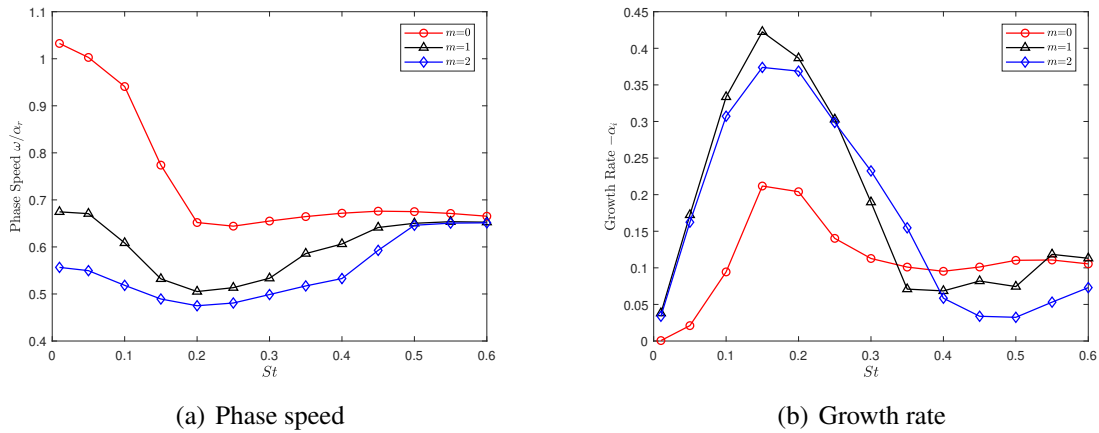


Figure 3-6. Variation of phase speed and growth rate of different azimuthal modes at $x/D = 2.5$.

3.1.2.2 Eigenfunction Comparison

The shape function \hat{q} of the instability wave solution, Eqn. (2-11), is important for determining the spatial distribution of perturbations. Figures 3-8 and 3-9 show comparisons of the shape functions of pressure and axial velocity perturbations at different axial locations for $m = 0$

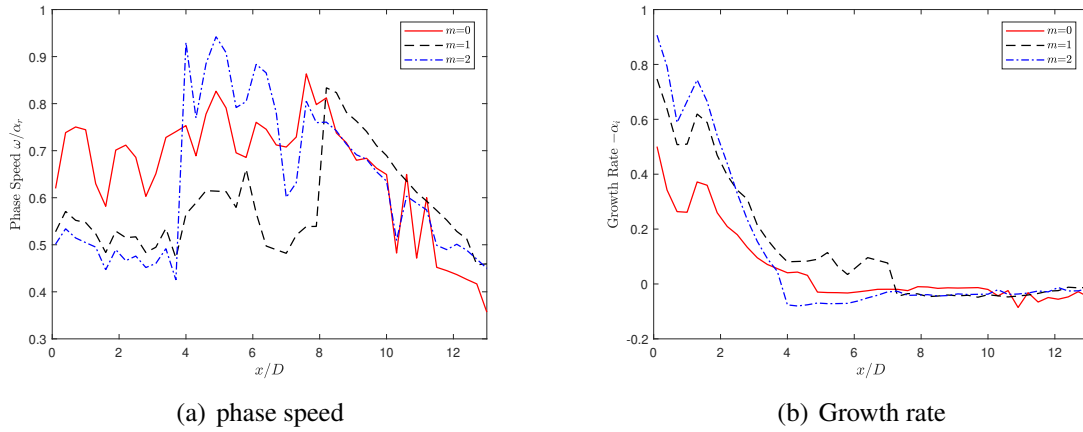
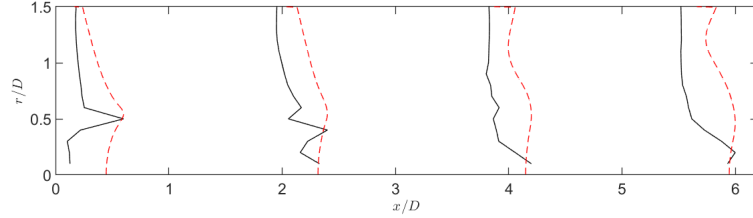
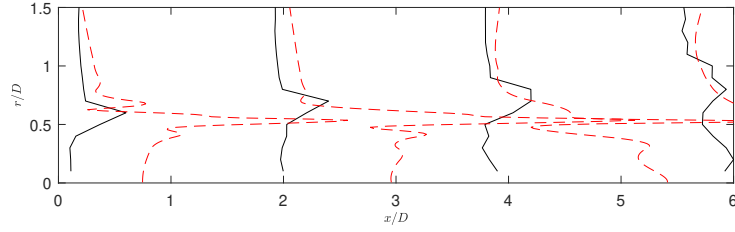


Figure 3-7. The development of phase speed and growth rate of different azimuthal modes along the streamwise direction at $St = 0.2006$.

and 1 between the LES and instability wave prediction. The corresponding St is 0.2006. The eigenfunctions are not valid at larger r because solutions of the compressible Rayleigh equation are not valid in that region and must be asymptotically matched with the outer solution [89]. The shape functions at specified axial locations are scaled with the maximum value obtained from LES at equivalent axial locations. For $m = 0$, the eigenfunction can be matched at the lip-line when $x/D < 2.5$, while the agreement is poor in the region $2.5 < x/D < 6$. This is because the instability wave excited by the screech tone in the jet exit region becomes amplified in the downstream and interacts with the shock cell structure. This is a nonlinear interaction.. The instability wave theory cannot capture the nonlinear effects due to the formulation based on the linearization of Navier-Stokes equations. The amplitudes of corresponding eigenfunctions of velocities in the radial direction are near infinity as shown in Figs. 3-8(b) and 3-9(b) due to the existence of a critical layer [89].

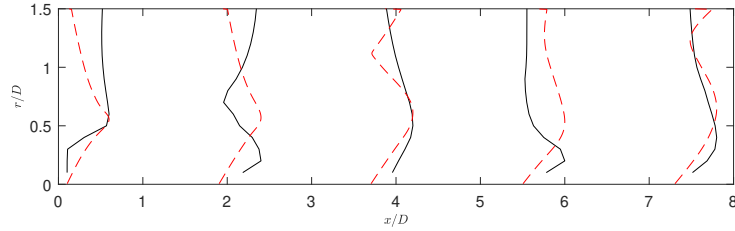


(a) Pressure eigenfunctions

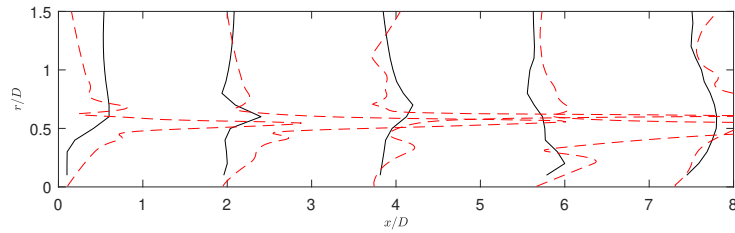


(b) Axial velocity eigenfunctions

Figure 3-8. Comparisons of pressure and axial velocity eigenfunctions for $m = 0$ between prediction (dash line) and LES (solid line).



(a) Pressure eigenfunctions



(b) Axial velocity eigenfunctions

Figure 3-9. Comparisons of pressure and axial velocity eigenfunctions for $m = 1$ between prediction (dash line) and LES (solid line).

We apply the matched asymptotic expansion method [17] to combine the inner and outer solution so that the eigenfunction can be extended to larger radial distances. The amplitudes of instability wave solutions are obtained by matching with the LES database (Eqn. (2-45)). The

comparisons of eigenfunctions of pressure perturbations between the LES and instability wave solutions are shown in Fig. 3-10 and 3-11. It can be seen that the eigenfunctions have a very similar decay rate at $m = 1, 2$, and 3 along the radial direction within the linear-hydrodynamic regime, where the region is approximately located at $0.5 < r/D < 2.5$ [54, 82]. However, the comparison of decay rate at $m = 0$ is poor. For the comparisons in the streamwise direction, the amplitudes of instability wave modes increase from the nozzle exit, and then reach a higher value around $x/D = 4$ to 6 , and finally decrease. These trends agree with Liu's observations [70, 83] of variation of amplitudes of instability waves, which have a maximum value near the end of potential core. The position of peak amplitude is close to the nozzle exit as the azimuthal mode increases, as observed in the Fig. 3-11, which is similar with the previous results of Liu [70, 83]. The amplitudes of LES increase from the nozzle exit along the streamwise direction.

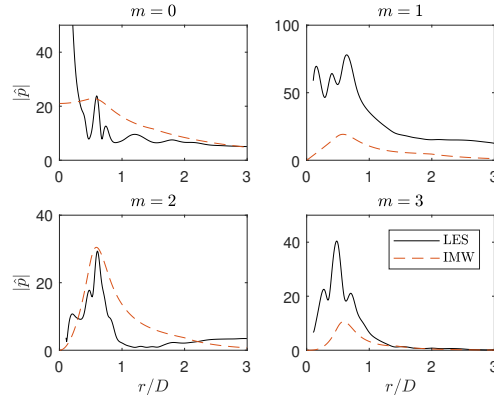


Figure 3-10. Comparisons of eigenfunctions of pressure perturbations between LES and prediction at $St = 0.1506$ for different azimuthal modes at $x/D = 2.5$.

We next apply the POD method to the LES database to decompose the mean flow-field. The extracted modes which represent the energy they captured. In general, the energetic modes can be used to construct the flow-field and represent the effects of the coherent structures. The reconstructed flow-field dataset is substituted into Eqn. (2-45) to compute amplitudes of instability wave models.

The POD modes are obtained in the space (x, r) domain corresponding each azimuthal mode. Figure 3-12 shows the eigenvalues of the POD results with increasing St . The dimension

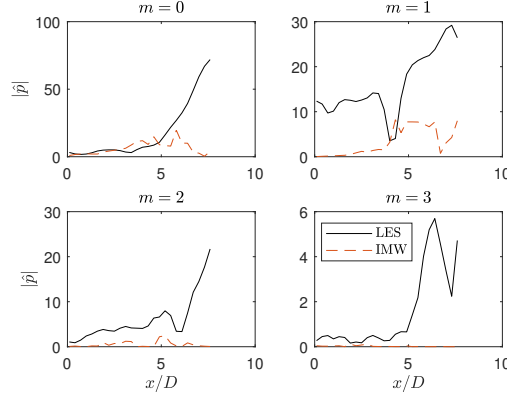
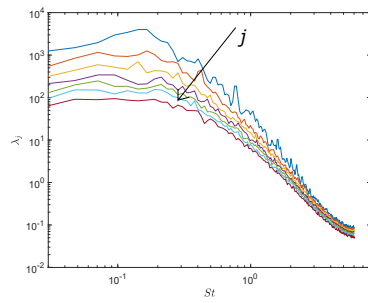


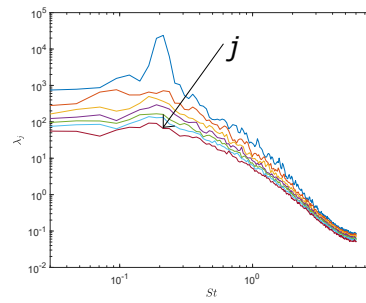
Figure 3-11. Comparisons of eigenfunctions of pressure perturbations between LES and prediction at $St = 0.1506$ for different azimuthal modes along the streamwise direction at $r/D = 3$.

of the sampled LES database is $2281 \times 30 \times 12 \times 44$, which corresponds to $[t, r, \theta, x]$. We separate the database with $N = 512$ with an overlap of 0.50. The total block number is 7. The setting is enough for analysis. The norm is based on pressure perturbations. The eigenvalues decrease as the mode number increases from $j = 1$ to 7 as the direction of the arrows in Fig. 3-12. It can be seen that as the azimuthal modes increase, the energy decreases. We observe a strong low-rank behaviour near $St = 0.2$ for $m = 1$, which coincides with the screech frequency of the jet. However, the low-rank behavior in other azimuthal modes do not exist.

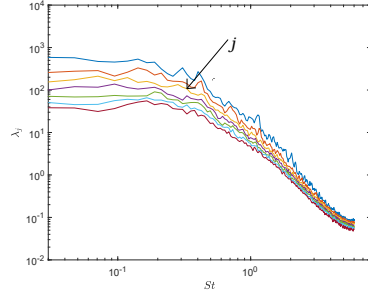
The pressure fields of the first and second POD modes for azimuthal modes $m = 0, 1, 2$, and 3 are plotted at $St = 0.12, 0.21, 0.4$, and 0.61 in Figs. 3-13 to 3-16. Some modes at some azimuthal modes take the form of coherent structures, such as the first mode of $St = 0.6$ for $m = 0$. Some modes have complex structures, such as the second mode of $St = 0.4$ for $m = 0$. We believe this is due to the existence of fine-scale structures in these modes. We reconstruct the flow-field from $-3 \leq m \leq 3$ with the 1st and 2nd POD modes as they are dominated by coherent structures.



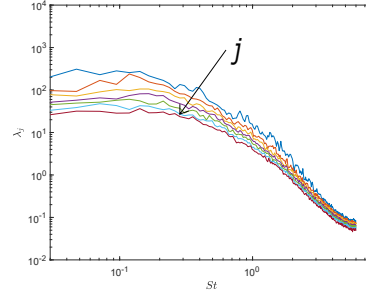
(a) $m = 0$



(b) $m = 1$



(c) $m = 2$



(d) $m = 3$

Figure 3-12. Eigenvalues as a function of St at different azimuthal modes.

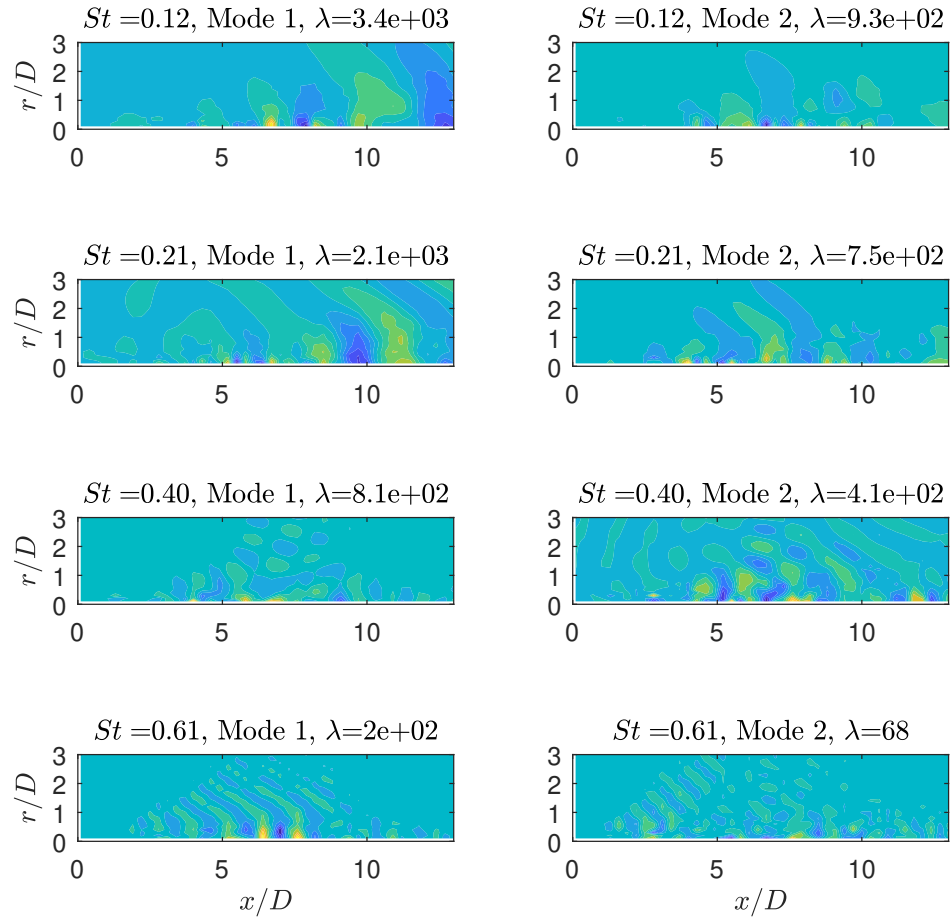


Figure 3-13. Eigenfunctions at $St = 0.12, 0.21, 0.4$, and 0.61 for 1st mode and 2nd mode for $m = 0$.

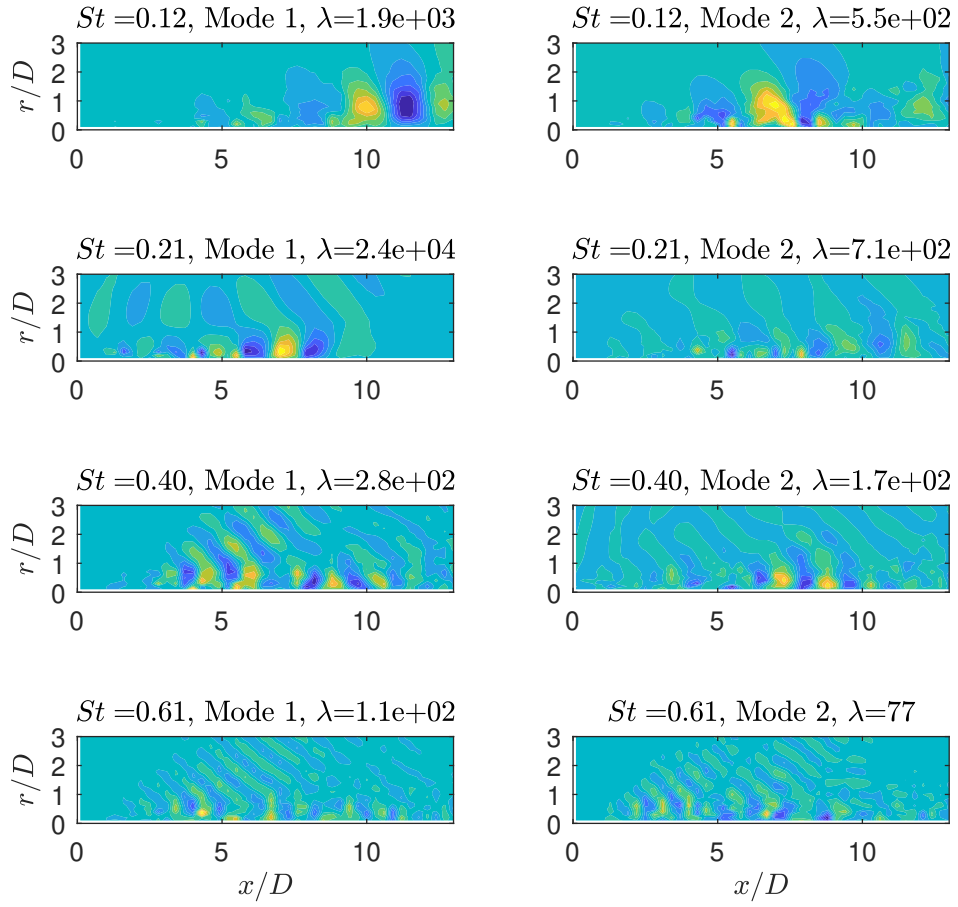


Figure 3-14. Eigenfunctions at $St = 0.12, 0.21, 0.4$, and 0.61 for 1st mode and 2nd mode for $m = 1$.

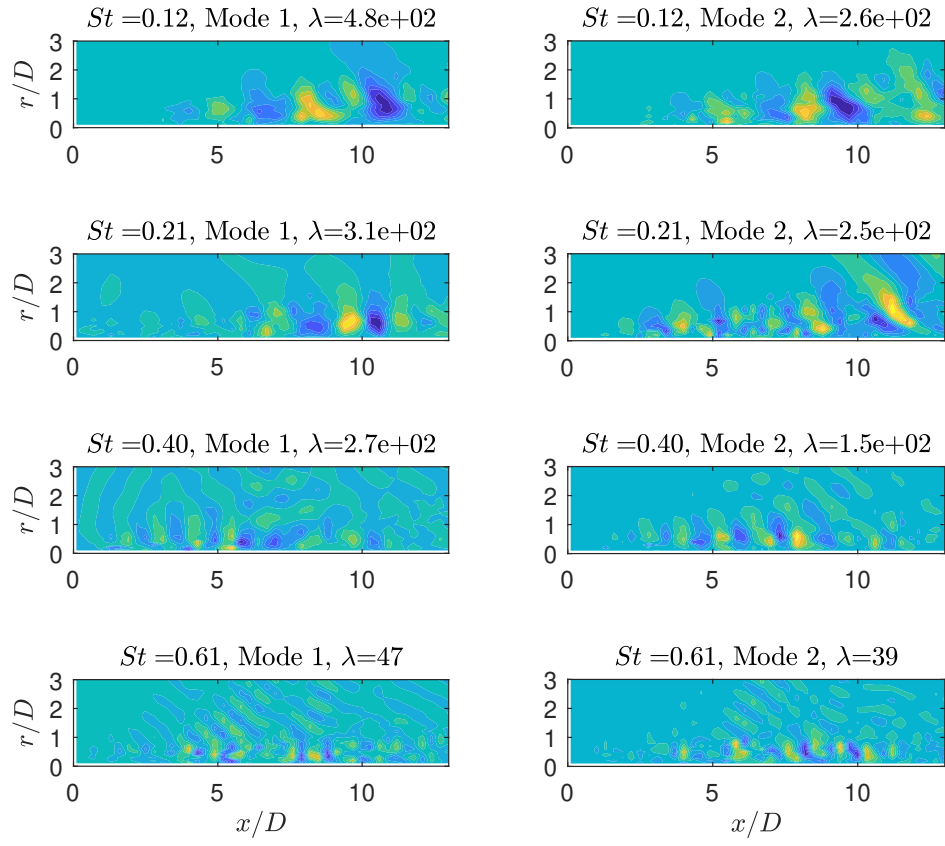


Figure 3-15. Eigenfunctions at $St = 0.12, 0.21, 0.4$, and 0.61 for 1st mode and 2nd mode for $m = 2$.

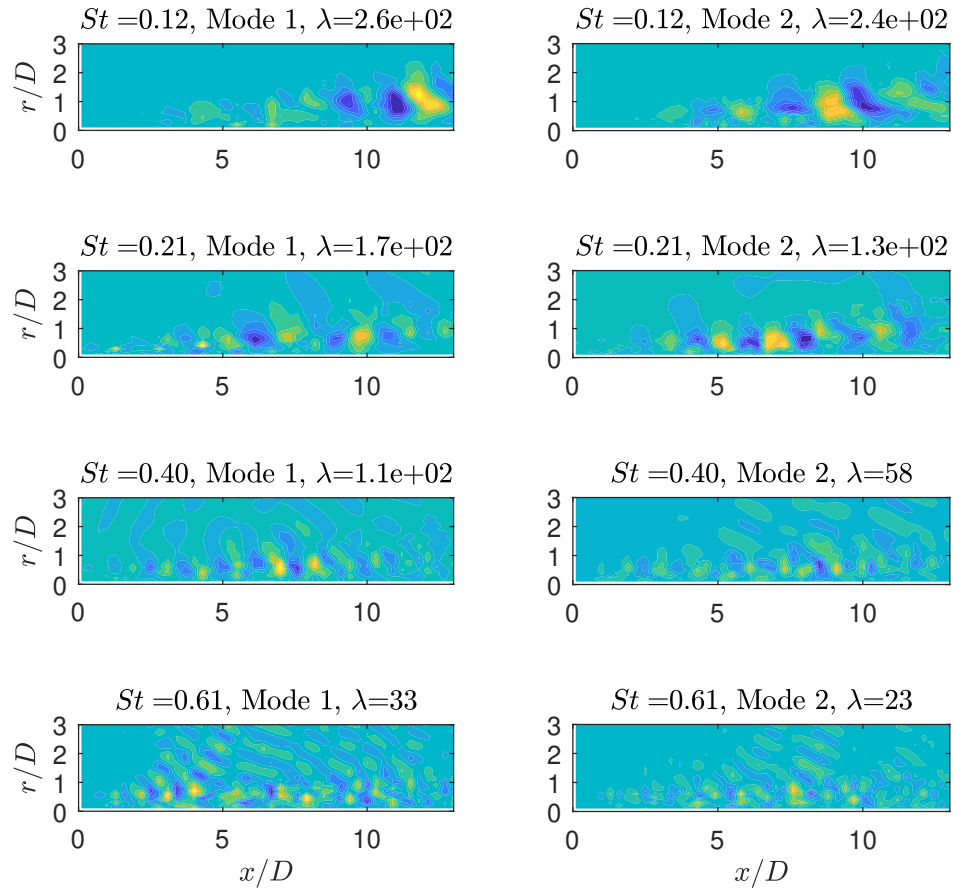


Figure 3-16. Eigenfunctions at $St = 0.12, 0.21, 0.4$, and 0.61 for 1st mode and 2nd mode for $m = 3$.

Figure 3-17 shows the comparisons of POD results and the calibrated instability wave models. It can be seen from the eigenfunctions in the radial direction (Fig. 3-17(a)) at $x/D = 2.5$ that they have a similar decay rate at $m = 1$ and 2. Furthermore, the comparison at $m = 0$ is improved due to the similar decay rate in the linear-hydrodynamic region. However, the eigenfunctions have poor agreement in the streamwise direction. We believe there are several reasons causing this. The matched asymptotic expansion method to combine the inner and outer solutions of instability waves may have some problems. The modes we chose to reconstruct the flow-field needs to be determined carefully. The norm of the POD analysis is a potential factor in constructing the flow-field to find the coherent structures.

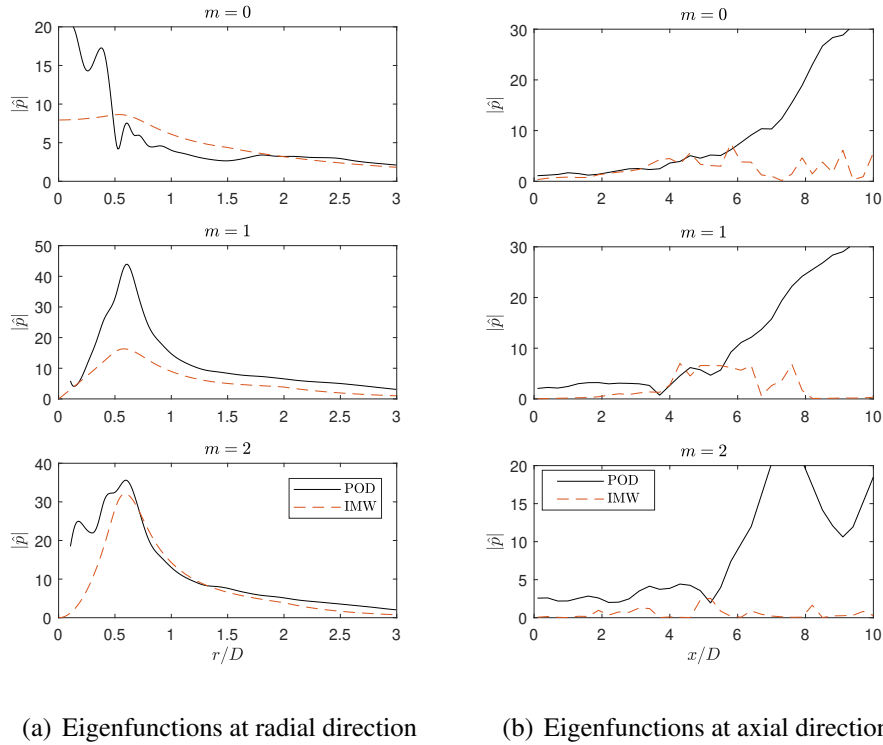


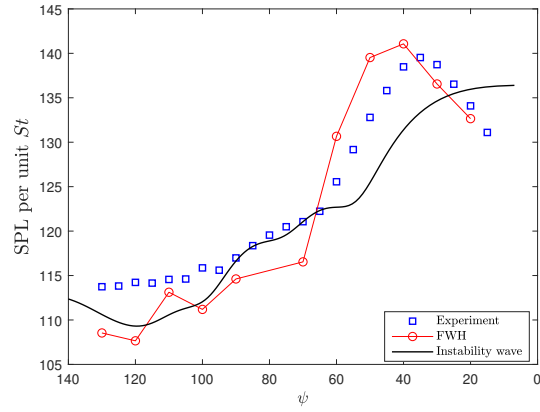
Figure 3-17. The comparison of eigenfunctions for different azimuthal modes at $St = 0.1506$.

3.1.3 Far-Field Sound

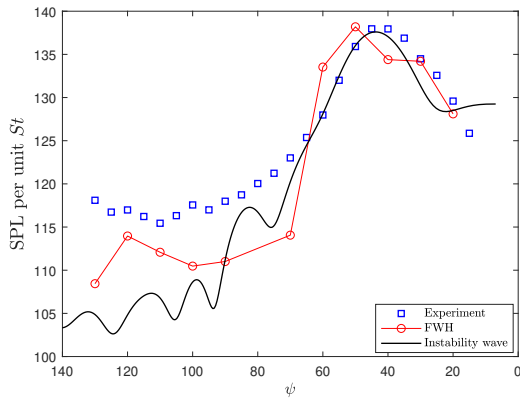
The far-field SPL from the instability wave solution is evaluated by Eqn. (2-27), where the term $\hat{g}(\bar{\eta}; \omega, m)$ is computed via Eqn. (2-37). The axial source region is chosen to extend to $x = 13D$, which is the maximum downstream location of sampled LES data.

Figure 3-18 shows the computed far-field SPL at discrete $St = 0.1003$, 0.2006 , and 0.4004 , where $St = 0.1003$ is the subharmonic frequency of 0.2006 , and $St = 0.4004$ is the harmonic frequency. The unknown constant \tilde{D} in Eqn. (2-27) is set equal to 0.05 , which ensures the SPL is the same as the maximum of experimental measurements at $St = 0.2006$. Figure 3-18(b) shows that predicted SPL matches experimental measurements for $\psi < 80^\circ$, where the jet noise from the large-scale turbulence dominants. In the upstream direction, the predicted SPL is approximately 7 to 10 dB lower than measurements. Our predictions confirm that the instability waves radiate noise in the upstream direction, but fine-scale mixing noise and BBSAN dominate in this direction. For FWH predictions ([152]) the peak noise amplitude in the upstream direction is dominated by BBSAN. The SPL predicted by FWH differs by at most 4 dB relative to experiment over the whole region as shown in Figs. 3-18(a) and 3-18(b). The predicted SPL of the instability wave at $St = 0.4004$ in Fig. 3-18(c) is lower by about 30 dB than experimental measurements and FWH in the upstream and lower by about 15 dB in the downstream directions. The subharmonic frequency of the excited instability wave in Fig. 3-18(a) shows that predicted SPL is 5 ~ 8 dB lower than the experiment in the downstream direction. This is because nonlinear effects are more pronounced at lower frequencies [80].

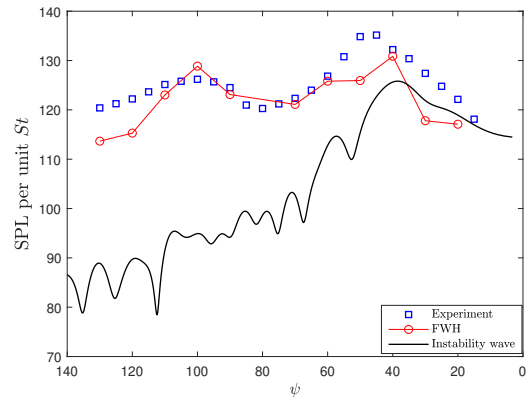
Figure 3-19 illustrates comparisons between the FWH and instability wave theory at different azimuthal modes from $m = 0$ to 3. We only present the positive azimuthal modes. The negative modes are the same as positive modes due to properties of eigenfunction [18]. The SPL from the FWH at $m = 0$ is higher than $m = 1, 2$ and 3 , which means large-scale turbulent structures contribute more to $m = 0$ radiated acoustic energy in the downstream direction. The instability noise source dominants at $m = 1$. According to Tam [19], when $M_j > 1.3$, the screech tone will change the mode shape from $m = 0$ (axisymmetric mode) to 1 (helical mode). Our predictions capture this observation. For $St = 0.4004$, the SPL of instability wave theory at $m = 2$ and 3 is larger than $m = 0$ and 1 , which means that the dominant modes will change or there is no single dominant mode for higher frequencies as described by Tam [18].



(a) $St = 0.1003$



(b) $St = 0.2006$



(c) $St = 0.4004$

Figure 3-18. Far-field noise comparisons on a polar arc of $100D$ relative to the nozzle exit at different St .

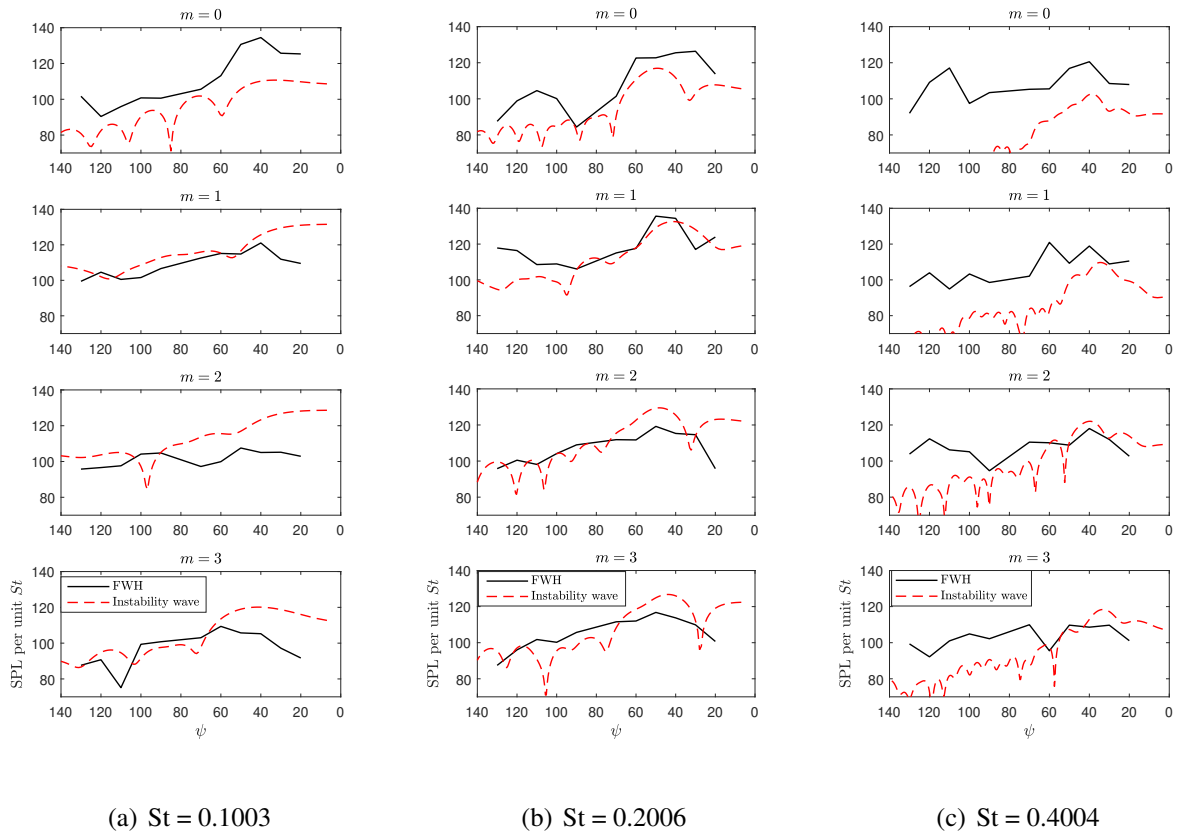


Figure 3-19. Far-field noise comparisons on a polar arc of $100D$ at different St at different azimuthal modes.

3.1.4 Correlation and Coherence Analysis

In this section, the auto-correlation, cross-correlation, and coherence in the far-field region for the predictions of instability waves and FWH methods are presented. The noise sources are analyzed based on the correlation results. In addition, the coherence analysis are used to understand the relation of the noise source in the frequency domain.

Firstly, the time series of pressure perturbations from instability wave models are constructed. We convert the outer solution (Eqn. (2-19)) to spherical coordinates and apply the stationary phase approximation method. Therefore, the pressure at the fixed azimuthal mode and frequency is obtained at the observer locations as

$$p(R, \psi) = \frac{R}{2} \hat{A}_0 \hat{g}(\bar{\eta}) \exp \left(i \left(\Phi(\bar{\eta}) - \frac{\pi}{2} (m+1) \right) \right) \exp(-i\omega t + im\theta), \quad (3-1)$$

and

$$\Phi(\bar{\eta}) = \frac{R}{1 - M_\infty^2} \bar{\rho}_\infty^{1/2} M_j \omega \left[(1 - M_\infty^2 \sin^2 \psi)^{1/2} - M_\infty \cos \psi \right]. \quad (3-2)$$

The amplitudes \hat{A}_0 are calibrated with the results in downstream direction ($\psi = 150^\circ$) where the large-scale turbulent structures dominant. The time series of pressure perturbations from instability wave models are obtained with the inverse Fourier transform of Eqn. (3-1).

3.1.4.1 Correlation Analysis

Figure 3-20 shows the comparison of measured normalized auto-correlations between the predictions from instability wave models and FWH method from $\psi = 160^\circ$ (downstream) to 50° (upstream) relative to the nozzle exit, where the dashed line is for results of instability waves and solid line is for FWH. It is shown that there are three shapes from the FWH results. When $\psi \geq 130^\circ$, they show large negative peaks, which demonstrates the character of the noise from large-scale turbulent structures [50]. When $\psi = 110^\circ$ and 120° , the negative values of FWH become smaller, which represent there are other noise sources become equivalent important as large-scale turbulent structures. When $\psi \leq 90^\circ$, there is a sharp peak and a clear ringing around the peak, which implies the combination of noise from fine-scale turbulent structures and BBSAN

[51]. On the other hand, the predictions show wide and large negative peaks for every angle, which provide evidence that the noise source of predictions are from large-scale turbulent structures. The instability waves can be used to approximate part of the noise from large-scale turbulence structures.

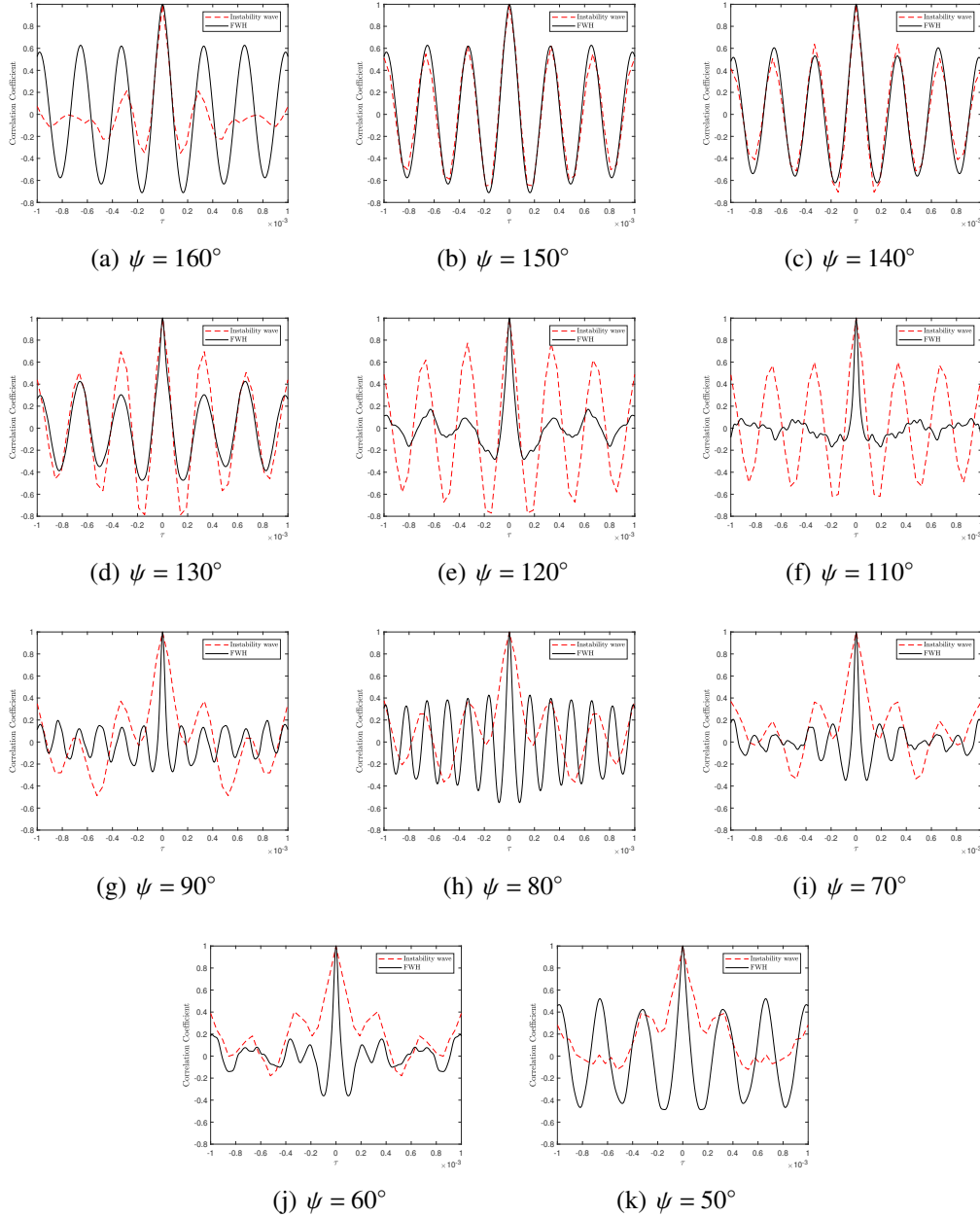


Figure 3-20. Comparison of auto-correlation between the predictions' and FWH results from $\psi = 160^\circ$ to $\psi = 50^\circ$.

Figure 3-21 shows the comparison of normalized cross-correlations between the predictions based on instability wave models and FWH method, where the fixed microphone is at $\psi = 150^\circ$ and $R/D = 100$ and the other microphone moves along an arc centered on the nozzle exit from $\psi = 150^\circ$ to 50° with distance $R/D = 100$. There is a peak value for $\psi = 150^\circ$ with $\psi = 160^\circ$ and $\psi = 140^\circ$, which means the dominant noise is from large-scale turbulent structures. However, there is no such peak at other observation angles. The results from predictions show similar shape and the range of coefficient are close, which shows that the radiated noise at other angles and the reference angle are from the similar noise source.

3.1.4.2 Coherence Analysis

An alternative method for ascertaining the level of correlation throughout the radiated sound field is formed via the coherence spectra computed via Eqn. (2-64). It can be used to learn more about the relation in the frequency domain. We show the coherence on several distinct St and observation angles.

Figures 3-22 and 3-23 are comparisons of coherence of far-field pressure perturbations between the instability waves models prediction and FWH method, where the reference microphone is located at $\psi = 150^\circ$ and $R/D = 100$. Figure 3-22 shows the variation of coherence with increasing St for $\psi = 150^\circ$ with 160° , 90° , and 50° , where Fig. 3-22(a) is the coherence of the results of instability waves. It can be seen that the coherence value are in the range of 0.4 to 1, while the coherence of the associated FWH method has its largest value at $St = 0.2$ (screech tone frequency). The value at other frequencies are relatively lower, for $\psi = 150^\circ$ with 90° and 50° . This phenomena shows the noise source is similar for the predictions based on the instability waves models. To be consistent with the far-field noise analysis, we still choose $St = 0.1$, 0.2 , and 0.4 to study the coherence. The coherence values from predictions based on the instability wave models are very close for three St for all the angles.

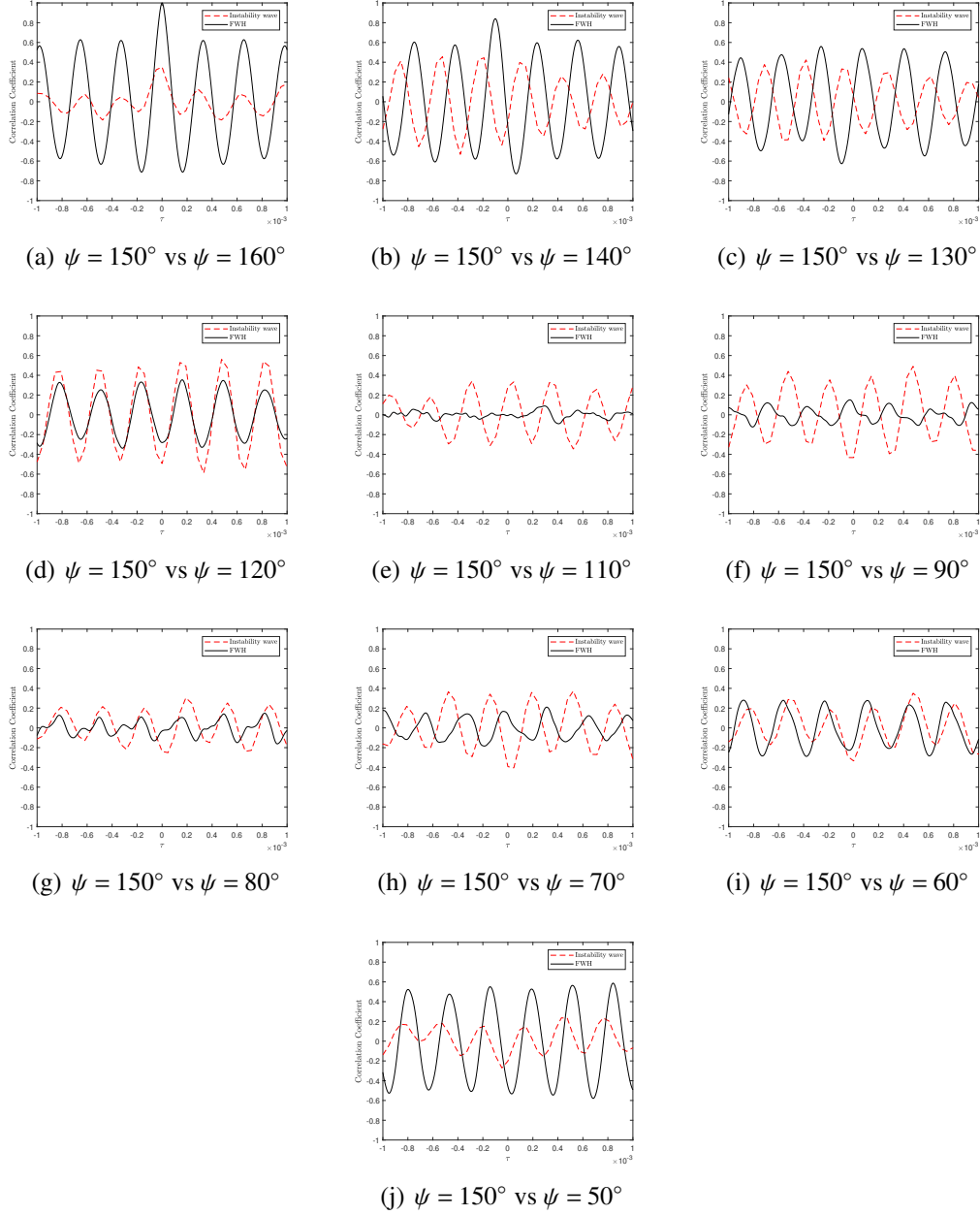
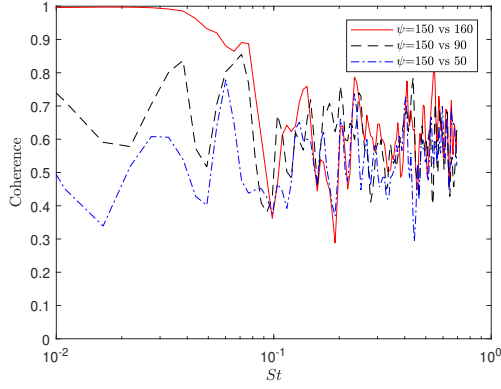
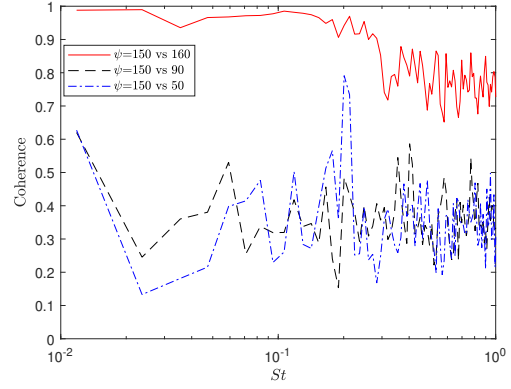


Figure 3-21. Comparison of cross-correlation between the predictions' and FWH results from $\psi = 160^\circ$ to $\psi = 50^\circ$ at far-field, where the reference microphone is at $\psi = 150^\circ$ and $R/D = 100$.

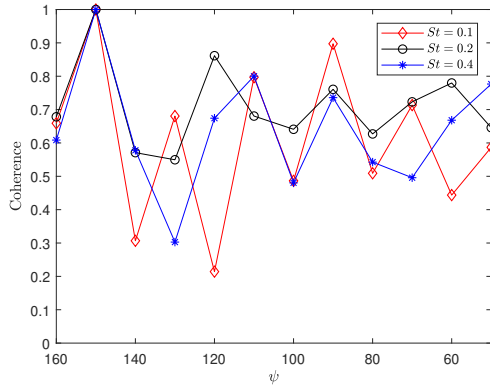


(a) Instability Wave

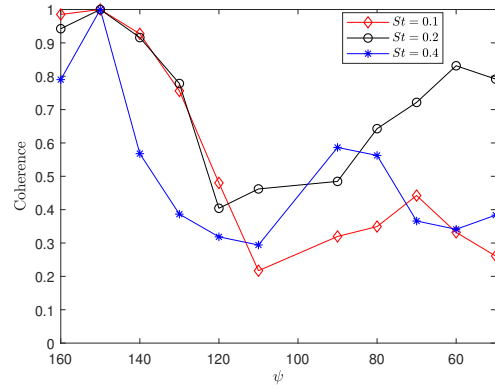


(b) FWH

Figure 3-22. Coherence of far-field pressure perturbations along with St for $\psi = 150^\circ$ vs 160° , 90° , and 50° .



(a) Instability Wave



(b) FWH

Figure 3-23. Coherence of far-field pressure perturbations at different angles at $St = 0.1$, 0.2 , and 0.4 , where the reference microphone is at $\psi = 150^\circ$.

3.2 Results of SERDP Case

3.2.1 Flow-Field Analysis

The second case we examine is an over-expanded conical nozzle from the SERDP program designed by Dr. Ukeiley's group at the University of Florida. The geometry of the nozzle is shown in Fig. 3-24 (courtesy by Dr. Ukeiley's group) [162]. The nozzle exit diameter is 0.0508 m. The design Mach number is $M_d = 1.76$. The fully-expanded jet Mach number is $M_j = 1.3$. The NPR and TTR are 2.77 and 1.00, respectively. The u_j is 385.6 m/s, and Re_D is 1.0×10^6 .

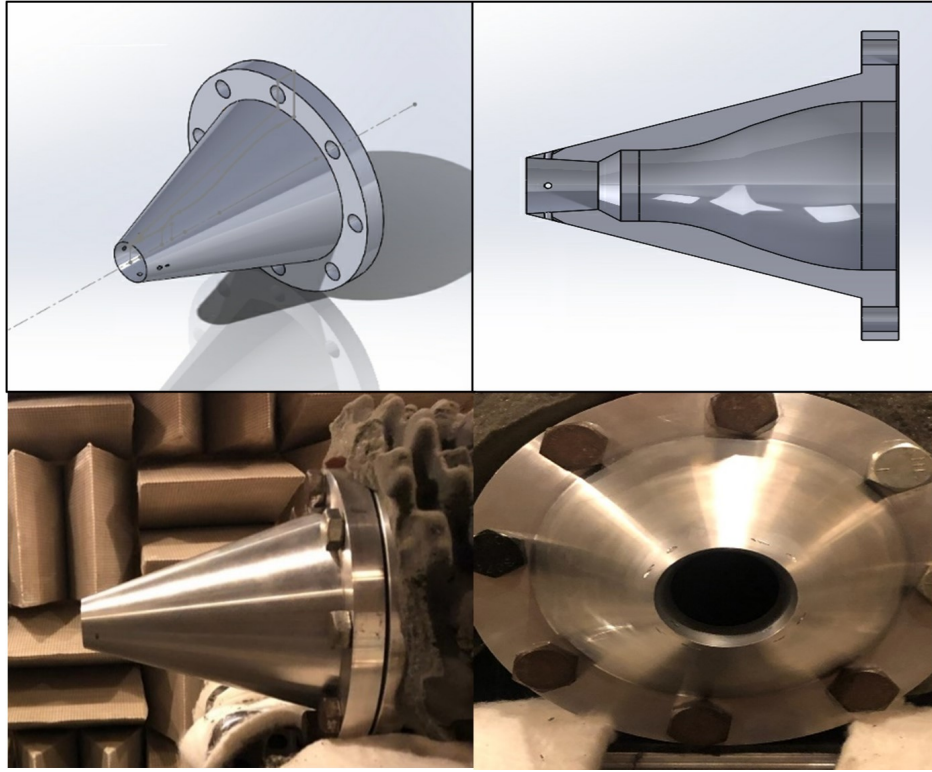


Figure 3-24. Isometric view of SolidWorks Nozzle (Top Left); Cut View of SolidWorks Nozzle (Top Right); Side View of Nozzle (Bottom Left); Front View of Nozzle (Bottom Right).

Figure 3-25(a) shows the results of mean axial velocity along the jet centerline from the LES and RANS, simulated by Dr. Shen [160] and Dr. Patel, respectively. Figure 3-25(b) shows comparison of the momentum thickness calculated numerically, which is an important factors in stability. The non-dimensional mean axial velocity from LES only has a small difference compared to RANS from the nozzle exit to $x/D = 2.5$. The potential core length of LES is

approximately $4.5D$ and that of RANS is around $5.5D$. The mean axial velocity of RANS and LES begin to decay with a similar rate after $x/D = 5$. The values of momentum thickness of RANS and LES are very close in the potential core region, however, the thickness of RANS becomes larger than that of LES.

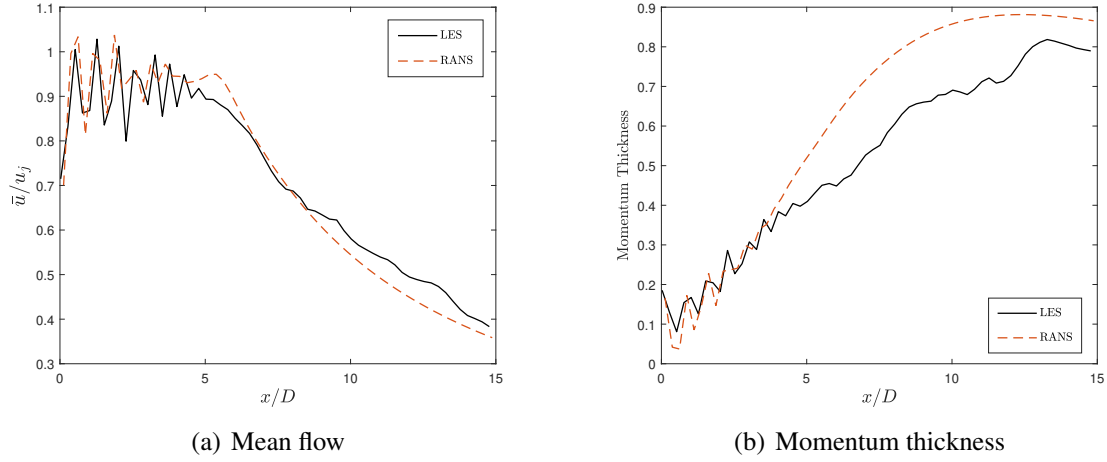


Figure 3-25. Comparisons of mean flow at the centerline and momentum thickness between LES and RANS.

3.2.2 Stability Analysis

Figure 3-26 presents the comparison of the phase speed and growth rate computed from the mean flow from RANS and LES for $0 < St < 0.7$ for $m = 0$ and 1 at $x/D = 2$. The changes of phase speed based on the mean flow of LES and RANS are similar. The phase speeds decrease at first and then have a fixed value around 0.78 for $m = 0$. The phase speed increases with the increasing St for $m = 1$. The growth rate of LES agree with that of RANS for $0.1 \leq St \leq 0.4$ for $m = 0$, while the growth rate of RANS is less than LES when $St > 0.4$. The growth rate of RANS is higher than that of LES when $St < 0.3$ for $m = 1$, but it becomes lower after this frequency. The variation is due to the difference of the mean flow and the momentum thickness [163, 88].

Figure 3-27 shows the comparison of phase speed and growth rate computed from the mean flow from the RANS and LES in the streamwise direction at $St = 0.2$ for $m = 0$ and 1. The analysis is initiated from $x/D = 0.2$. The phase speeds exhibit oscillations inside the potential core region for all modes analyzed for LES and RANS. This phenomenon reflects again that the instability

wave extracts the energy from the mean flow and is similar to the mean flow variation in the core region. Similarly, the phase speeds of LES and RANS begin to decay after the potential core. The growth rates for both modes peak on the initial axial plane and then decay with axial distance.

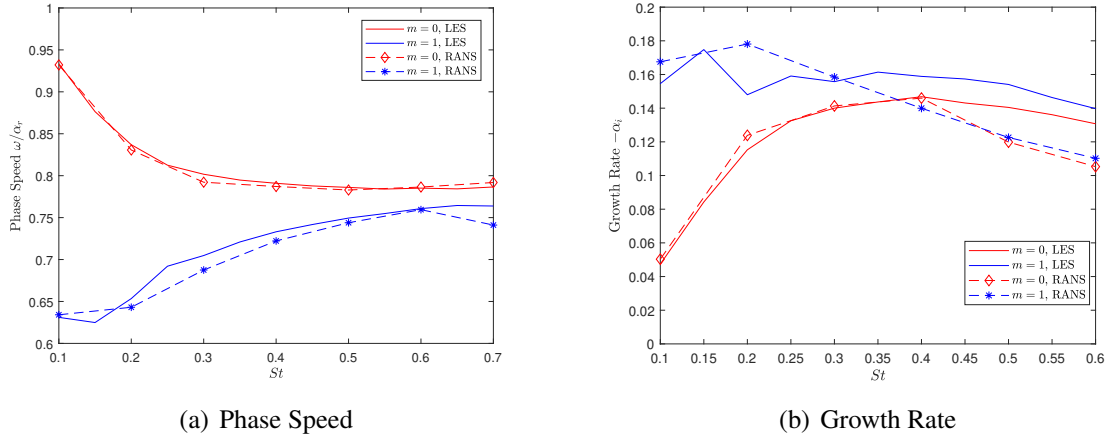


Figure 3-26. Phase speed and growth rate at different St computed from the mean flow of LES and RANS.

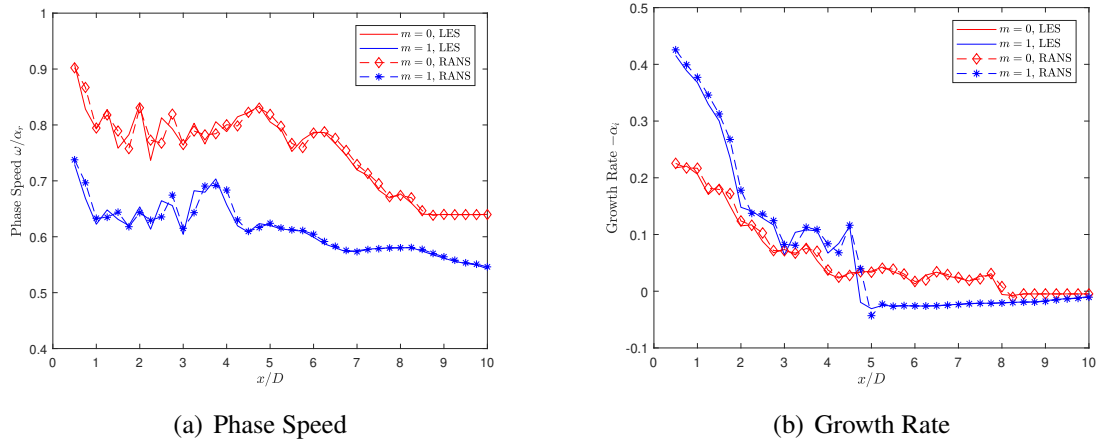


Figure 3-27. Phase speed and growth rate along the streamwise direction computed from the mean flow of LES and RANS.

3.2.3 Far-Field Noise Prediction

3.2.3.1 Far-Field Noise via Kirchhoff Surface Method

The experimental data was measured using a microphone array on an arc with a radius of $30D$ from the upstream direction of 60° to the downstream direction of 150° with an interval 10°

(measured and courtesy by Dr. Ukeiley's lab). The data on the Kirchhoff surface (R_s) is from LES database [160]. The number of samples is 2230 time steps on the KS with radius $R_s = 3.5D$ and length $x_s = 35D$. The time history of pressure fluctuations via the KS method is computed via Eqn. 2-62, where 12 evenly spaced azimuthal locations for each observation angle are computed. The spectra are averaged at the azimuthal locations to obtain the noise spectrum for each observation angle. This also can be used to eliminate the poor statistical convergence, especially at low frequencies.

Figure 3-28 shows comparisons of acoustic spectral between predictions and experimental measurement at one upstream angle of 60° , one sideline angle of 90° , and one downstream angle of 140° . For the KS approach, the predicted noise decays rapidly for $St \geq 1$. Based on grid resolution of the simulation, the St_{max} is around 1.5 computed with $St_{max} = \frac{(\mathcal{P}+1)c_\infty D}{8\Delta x u_j}$, where \mathcal{P} is the order of precision and Δx is the point spacing of the CFD simulation [164]. In addition, the specific decay frequency also depends on the observation angle. Therefore, the results are reasonable. There is an over-prediction at 60° when $St \leq 0.1$. We believe there are two reasons causing this. The first is the open-shell of KS, the other is the abrupt increment of pressure perturbations on the KS. It can be seen that the sound spectrum is improved when removing the abrupt increment of pressure perturbations as the blue line from the Fig. 3-28. The cut-off frequency at lower range is extended to $St = 0.04$.

3.2.3.2 Far-Field Noise from Instability Wave Models

The amplitudes of the instability waves are determined firstly within Eqn. (3-1) to reconstruct the time series of pressure perturbations. The dataset used to calibrate the amplitudes is obtained with KS method. We choose the dominant direction via the OASPL as shown in Fig. 3-29 within the range of $0 < St \leq 0.7$, which is the range of validity of instability waves for the present calculation. Therefore, we choose $\psi = 150^\circ$ as the angle to calibrate the amplitudes of instability waves.

Figure 3-30 shows the sound spectra at $\psi = 60^\circ, 90^\circ$, and 150° for SERDP at $R/D = 30$. The acoustic predictions are presented within the range of $St < 1$. It can be seen that the value of SPL

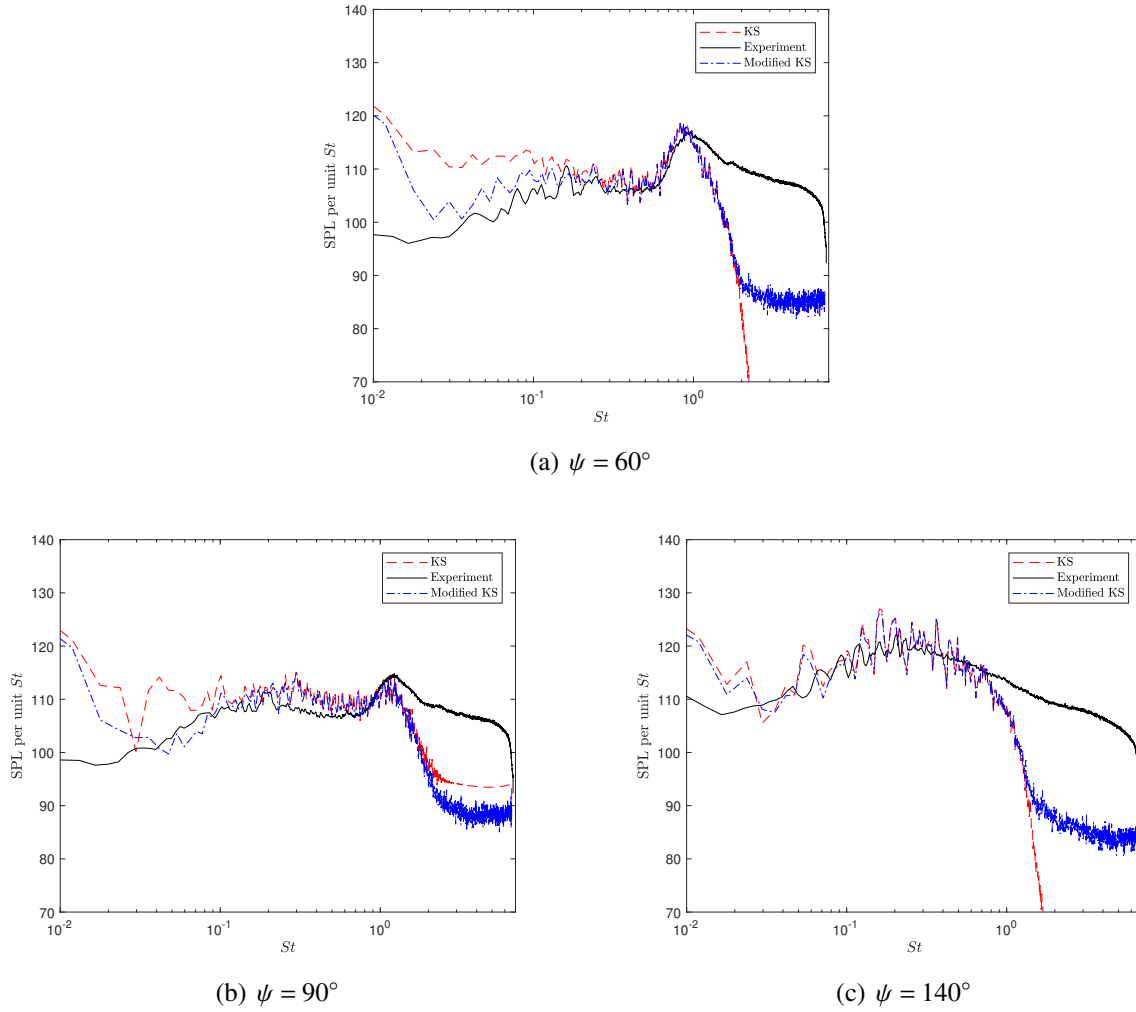


Figure 3-28. Comparisons of far-field sound spectra between the experiment and KS method at sideline and downstream directions.

of the predictions from the instability wave modes are lower than the experiment and KS method at lower $St < 0.1$, and higher at $St \geq 0.5$. The value of SPL at the intermediate St range are close to the experiment and KS method. The near-field sound spectrum ($\psi = 50^\circ$ and $R/D = 15$) is also predicted with the instability wave model and the comparison with the experimental measurement is shown in Fig. 3-31. The figure shows that there is an over-prediction for the KS method at lower frequencies, which is similar to the far-field results. The prediction from instability wave models show poor agreement with the experiment. But this large discrepancy is expected at the sideline and upstream directions, where the noise from fine-scale and BBSAN dominants.

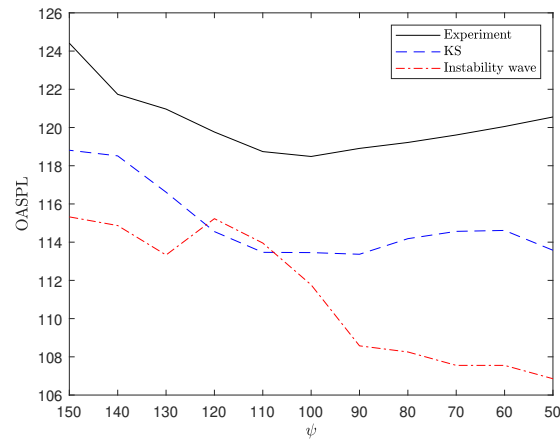
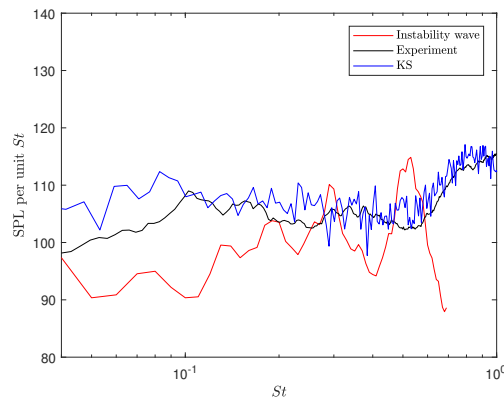
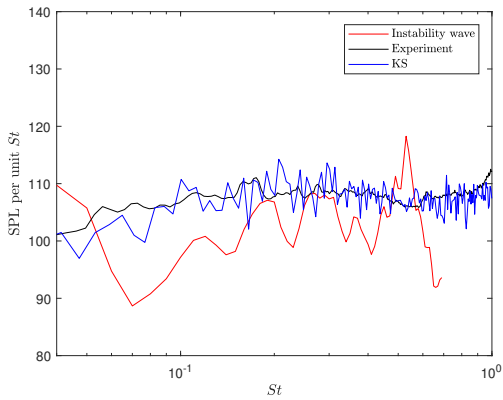


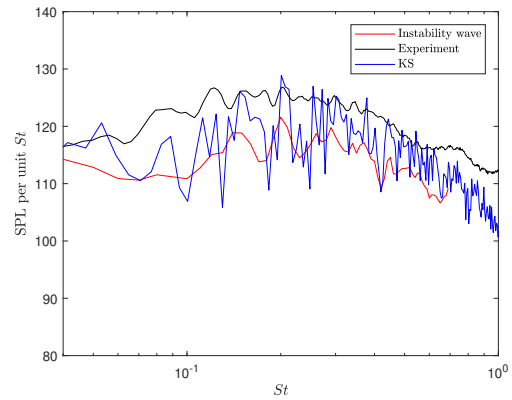
Figure 3-29. Comparisons of OASPL among predictions, the KS method, and experimental measurement.



(a) $\psi = 60^\circ$



(b) $\psi = 90^\circ$



(c) $\psi = 150^\circ$

Figure 3-30. Comparisons of far-field sound spectra among the instability wave solutions, KS method, and experiment in the upstream, sideline, and downstream directions.

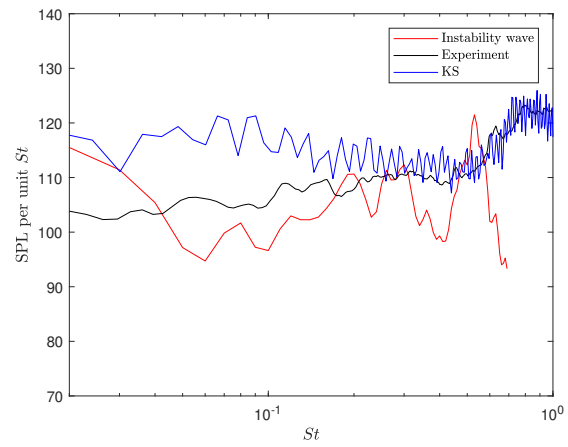


Figure 3-31. Comparisons of near-field sound spectrum between the instability wave solutions and experiment at upstream direction ($\psi = 50^\circ$).

3.2.4 Correlation and Coherence Analysis

The auto-correlation and cross-correlation of experimental measurements and predictions from instability wave models are compared for the bi-conic nozzle. The noise source are analyzed based on the correlation results. The coherence analysis provide information in the frequency domain. In addition, the correlation and coherence between the near- and far-field are analyzed. The results are used to explain that it is possible to design a control system for large-scale structure noise based on upstream control if the instability noise can be extracted.

3.2.4.1 Correlation Analysis

Figure 3-32 shows the comparison of measured normalized auto-correlations for the SERDP nozzle between the predictions' and experimental results from $\psi = 150^\circ$ to 60° . It is shown that there are two distinct shapes from the experimental results, which represent two different noise sources, as described by Tam et al. [50]. The wide peak and large negative peaks at $\psi = 150^\circ$ and 140° shows the character of the noise from large-scale turbulent structures. When $\psi \leq 110^\circ$, there is peak and clear ringing around the peak, which implies the combination of noise from fine-scale turbulent structures and BBSAN [51]. On the other hand, the results of predictions show wide peak and large negative peaks for every angle, which provides evidence that the noise source of predictions is large-scale turbulent structures. The instability waves can be used to approximate part of the noise from large-scale turbulence structures.

Figure 3-33 shows a comparison of maximum normalized cross-correlations. Comparisons are made between the predictions, KS results, and experiments, where the $\psi = 150^\circ$ microphone is the fixed microphone. The other microphone is moved along an arc centered on the nozzle exit. For 140° , the value of cross-correlation coefficient is larger than that of other angles, which indicates that the dominate noise at the downstream direction is from the large-scale turbulent structures. The cross-correlation coefficient of the instability predictions at other observer angles ($\psi \leq 130^\circ$) is much larger than experiment. This shows that the noise source in the upstream and sideline directions is very different from the downstream direction, which is related to the instability model.

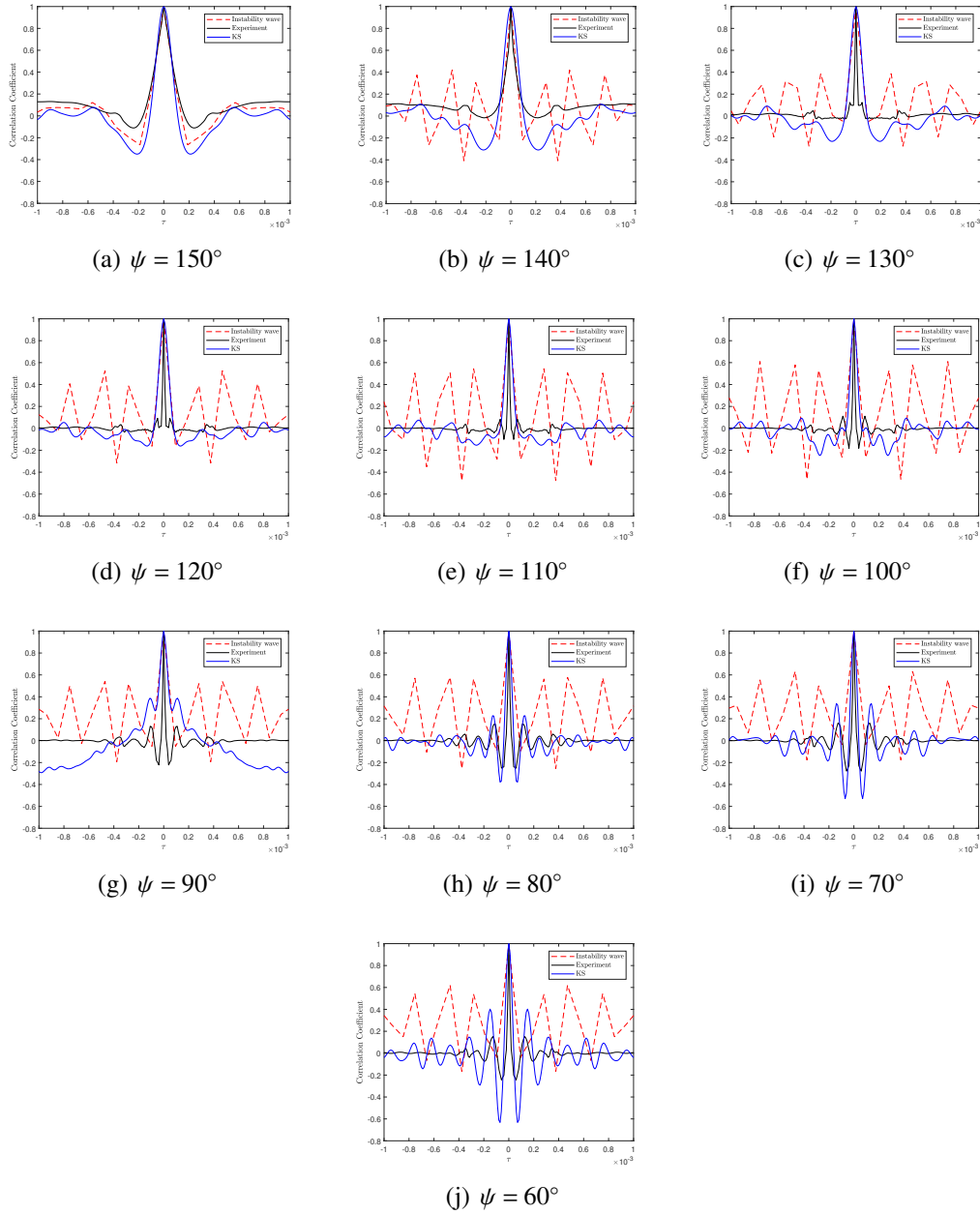


Figure 3-32. Comparison of auto-correlation between the predictions' and experimental results from $\psi = 150^\circ$ to $\psi = 60^\circ$.

Next, we study the correlation between the near- and far-field acoustic pressure of predictions, experimental measurement, and KS method. We choose the near-field microphone ($R/D = 15$ and $\psi = 50^\circ$) as the fixed reference microphone. Other microphones are at $R/D = 30$ from $\psi = 150^\circ$ to 60° . For the calculation of the time delay (τ), the near-field acoustic pressure

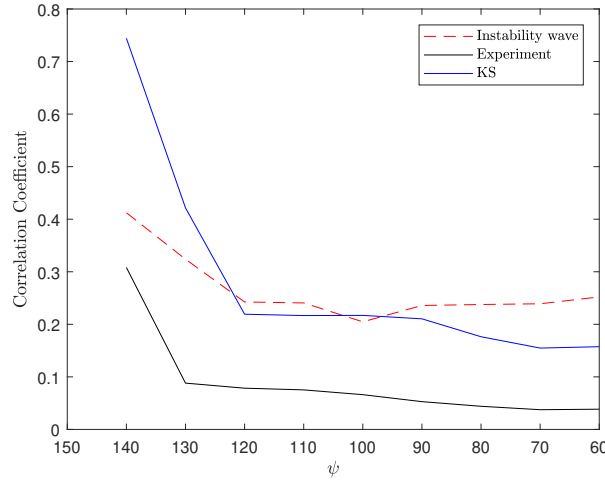


Figure 3-33. Comparison of maximum cross-correlation among the predictions, the KS method, and experimental results from $\psi = 140^\circ$ to $\psi = 60^\circ$, where the reference microphone is at $\psi = 150^\circ$.

has an approximate time advancement $d\tau = (|y_n| - |y_f|)/c_\infty$, where the subscript n and f denote the near- and far-field, and y is the distance between the noise source and observer locations [27]. The maximum normalized cross-correlation between the near- and far-field is shown in Fig. 3-34. It can be seen that the correlation coefficients of experimental measurements are less than 0.1 from $\psi = 150^\circ$ to 90° , while there is an incremental change for $\psi = 80^\circ$ to 60° . These results imply that the near-field upstream and far-field downstream radiation directions are uncorrelated, and the sound sources are distinct. The correlation coefficients of prediction results vary in the range between 0.2 to 0.6.

3.2.4.2 Coherence Analysis

Figure 3-35 shows the coherence of far-field acoustic pressure for the SERDP case, where the reference microphone is located at $\psi = 150^\circ$. The variation of coherence at distinct St in Fig. 3-35 shows a lower coherence value than 0.3 for the chosen St (Fig. 3-35(b)), while the coherence value of predictions are in the range of 0.4 to 1 as shown in Fig. 3-35(a). These results show that significant coherence is present according to the instability wave prediction alone compared to experimental measurements. The latter has dominant sources at varying observer angles, and therefore coherence is not expected to be large over a wide range of observer angles.

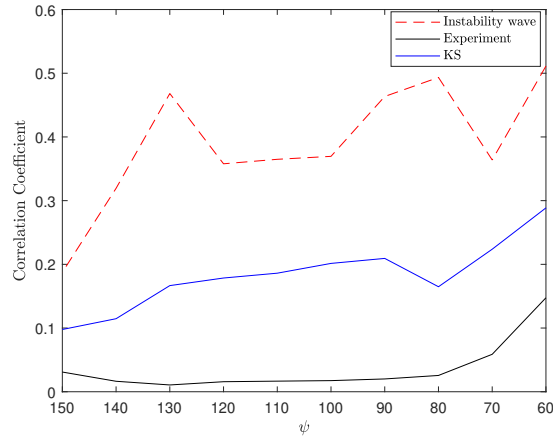


Figure 3-34. Comparison of maximum cross-correlation between the near- and far-field acoustic pressure from the prediction, the KS method, and experiment. The reference microphone is in the near-field.

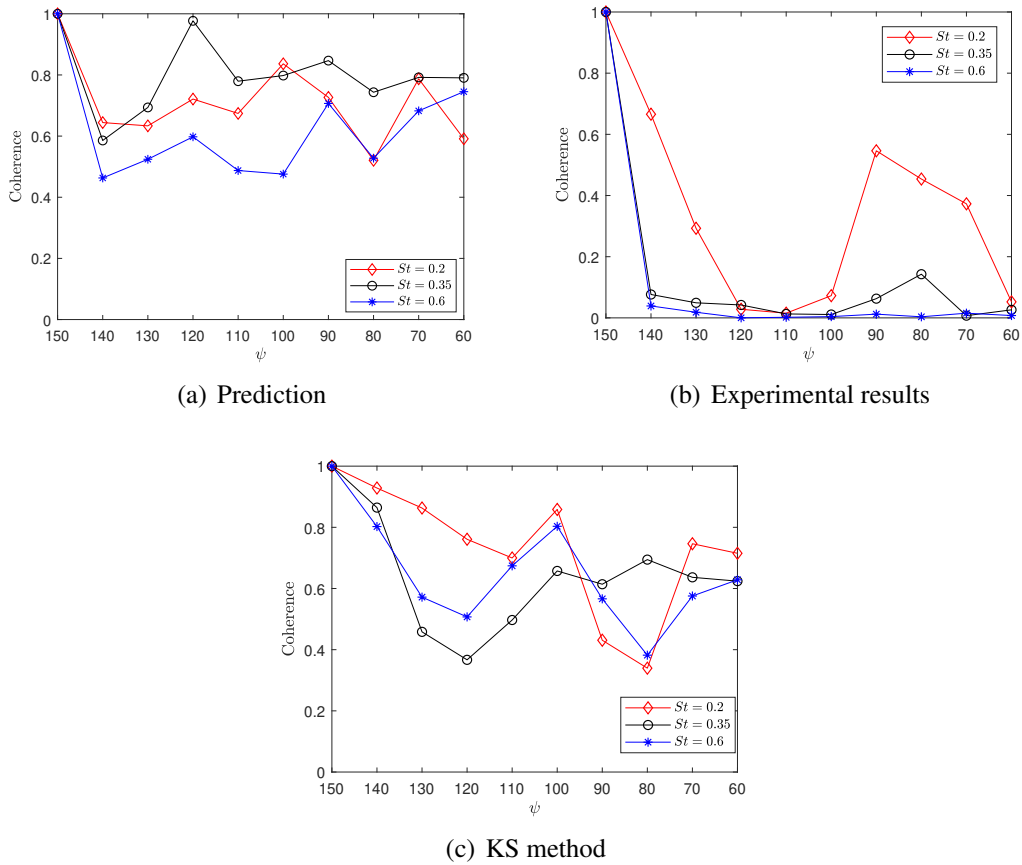


Figure 3-35. Coherence of far-field acoustic pressure at different angles for $St = 0.2, 0.35$, and 0.6 , where the reference microphone is at $\psi = 150^\circ$.

Next, we present the coherence between near- and far-field acoustic pressures in Fig. 3-36, where the reference microphone is at the near-field upstream position ($\psi = 50^\circ$ and $R/D = 15$). The coherence from instability waves varies within the range of 0.4 to 0.7 at all St , while the experimental results have coherence values less than a maximum of 0.30 and are nearly zero through the entire St investigated.

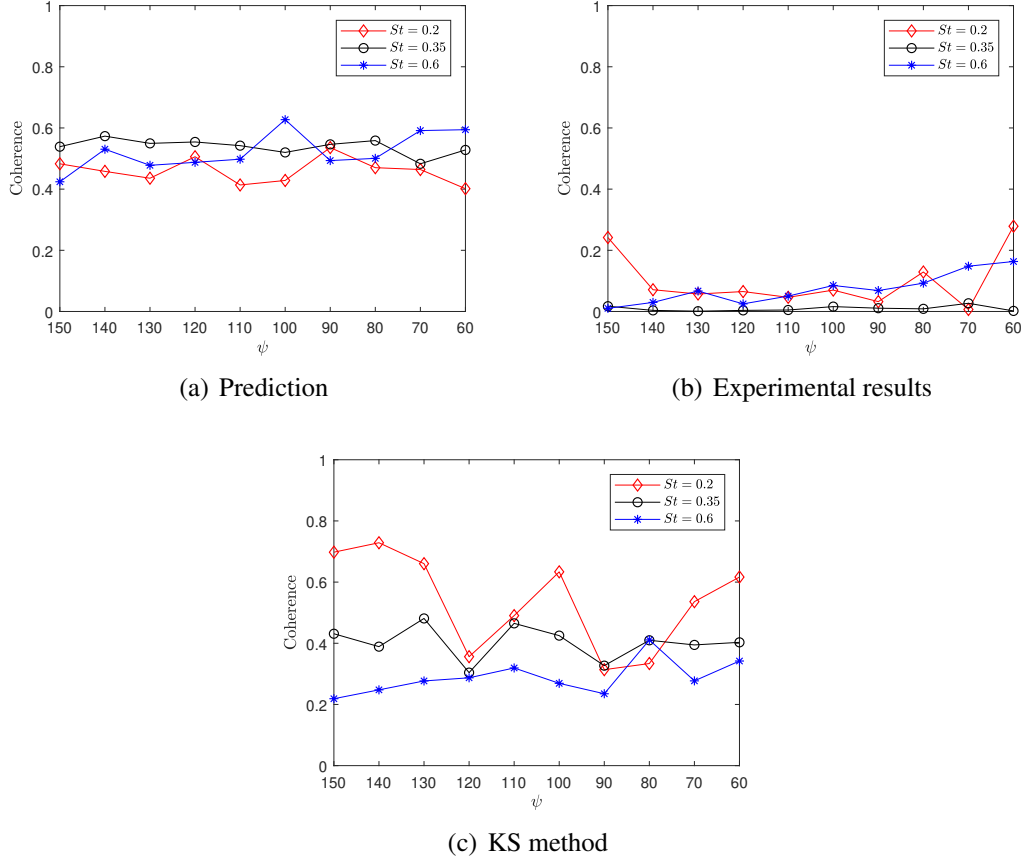


Figure 3-36. Coherence of near- and far-field acoustic pressure at different angles at $St = 0.2$, 0.35, and 0.6, where the reference microphone is at $\psi = 50^\circ$ and $R/D = 15$.

CHAPTER 4

CONE FLOWS AND STABILITY CALCULATIONS OF BOUNDARY LAYERS

In this chapter, the mean flow-fields, stability properties, and spatial coherence of pressure perturbations from instability waves for flows over the cone configuration are predicted, validated, and discussed, where the cone configuration with different nose radii from sharp to blunt and flow over cones at different free-stream Mach numbers are studied. Finally, the flow-fields with plasma actuation are examined.

4.1 Base Flow-Fields Computation and Validation

4.1.1 Mean Flow-Field Computation and Validation

The Stanford University Unstructured (SU2) open source software suite (see Palacios et al. [158] for details) is used to compute the time-averaged flow-field. The SU2 solver is finite-volume based, and we solve the steady compressible NS equations in axisymmetric form. We computed the freestream Mach number ($M_\infty = 3.5$) flow of Gross and Fasel [48] as the test case. In this test case, the cone half angle is (θ) 7° , the nose radii (r_n) is 0.038 mm, and the length of the cone (L) is 0.3556 m. The other freestream parameters used for the simulations are freestream temperature and density, and are 90.1 K and $8.74 \times 10^{-2} \text{ kg/m}^3$, respectively. Figure 4-1(a) shows the entire flow region ($0.3556 \text{ m} \times 0.2 \text{ m}$). A structured grid is used with an exponential distribution. This allows for decreased grid spacing near the wall. The grid point distribution around the nose region is shown in Fig. 4-1(b). We set the first mesh cell off the wall as $1 \times 10^{-6} \text{ m}$, which is estimated for a desired Y^+ value less than 1 using flat-plate compressible boundary layer theory. Additionally, a grid independence study is conducted. On the cone surface, the no-penetration and the no-slip conditions are enforced. The wall is set to be adiabatic ($\partial T / \partial y_n = 0$).

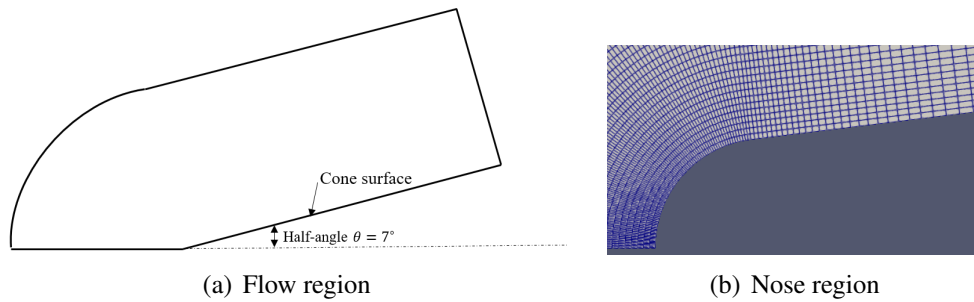


Figure 4-1. The domain and computational grid near the nose.

Two grid size are used to examine grid independence. The coarse grid size is 201 points in the wall normal direction and 201 points in the streamwise direction, and the fine grid uses 401 points in the wall normal direction and 201 points in the streamwise direction. Figure 4-2 shows the residual and Y^+ of the coarse grid simulation. These graphs show that the numerical simulation converges, and the grid distribution is sufficient to resolve the flow-field.

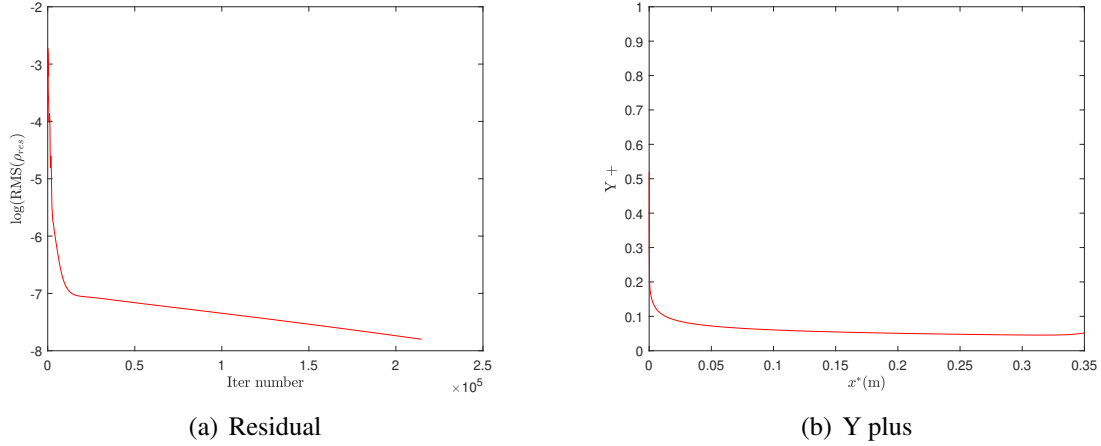


Figure 4-2. Residual and Y plus of the CFD simulation for the coarse grid point distribution.

The validations of flow-fields from numerical simulation are shown in Fig. 4-3. Comparisons of the flow-field between two profiles from numerical simulation and Gross and Fasel [48] (shown as “Ref”) are made with axial velocity and temperature distributions at three streamwise locations corresponding to Gross and Fasel [48] of $x^*/L = 0.624, 0.76$, and 0.825 . The axial velocity and temperature are normalized with the boundary layer edge values, which are directly extracted from the CFD solution. The positions of the boundary layer edge of Laible [165] are defined as the point where the wall normal derivative, $\partial u / \partial y$, of the velocity component parallel to the cone surface (u) is minimum. In this paper, we choose the positions as the value of derivative less than a small value (0.05). We apply the infinity norm of the relative error to quantify the error among the profiles in the Fig. 4-3. The error of flow-field profiles of the coarse and fine grid is 1.4% at $x^*/L = 0.76$ based on the variation of T in the cross-stream direction, which shows grid independence of the current numerical simulations. In addition, the maximum infinity norm of relative error between the numerical simulation and Gross and Fasel [48] (shown

as “Ref”) is 0.8% at $x^*/L=0.624$. Therefore, the coarse grid distribution is used in the following analysis.

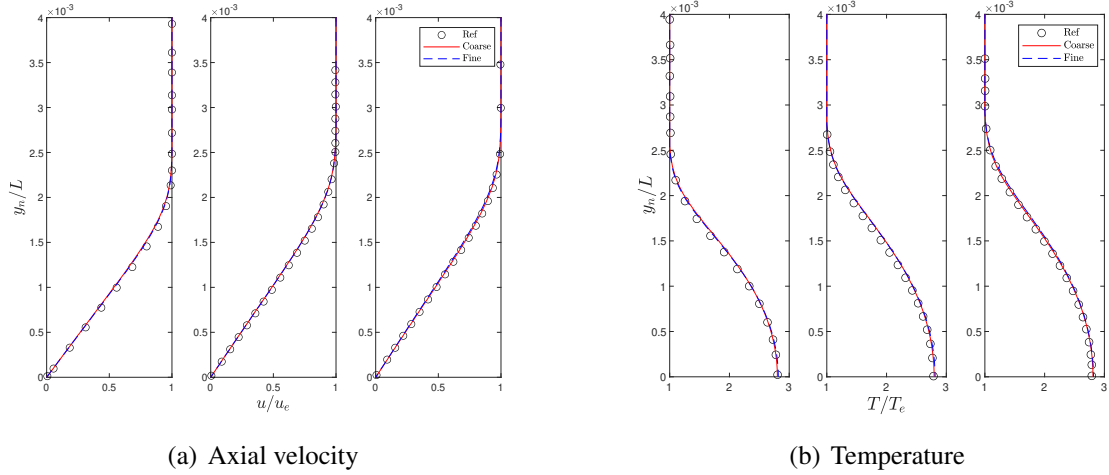


Figure 4-3. The comparison of axial velocity and temperature at different streamwise positions, where $x^*/L = 0.624, 0.76$, and 0.825 .

We perform a parametric study of flow conditions, which is summarized in Table 4-1. We vary Mach number and leading edge radius. The leading edge radii vary from a sharp curvature to a blunt cone [111]. We refer to the leading edge radii from smallest to largest as r_i , where i is from 1 to 10.

Table 4-1. Flow conditions.

Free-stream Mach numbers	$M_\infty = 2, 3.5$, and 5
Nose radius	$r_i = 0.038, 0.076, 0.152, 0.38, 1.14, 1.905, 3.969, 7.938, 15.876$ and 38.1 mm
Half-angle	$\theta = 7^\circ$
Free-stream temperature	$T_\infty = 90.1$ K
Free-stream pressure	$p_\infty = 2260.4$ Pa

For the flow region, we extend the test case region to $3.5 \text{ m} \times 3.5 \text{ m}$, which is a large value to guarantee that the flow-field is large enough to capture relevant data for our analysis. The grid size is 267 points in the wall normal direction and 301 points in the streamwise direction.

Numerical predictions are conducted in serial on the local high-performance computing cluster at University of Florida.

Figures 4-4, 4-5, and 4-6 show Mach number contours of a portion of the entire flow region ($0.3 \text{ m} \times 0.2 \text{ m}$) of $r_1 = 0.038$, $r_7 = 3.969$, and $r_{10} = 38.1 \text{ mm}$ at $M_\infty = 2$, 3.5, and 5. As the nose radii increases at fixed M_∞ , the shock detached from the leading edge and a bow shock appears. The shock layer becomes increasingly thicker, and the entropy layer emerges due to the shock curvature in the downstream direction. For example, the shock layer thickness within Fig. 4-6 for r_1 , r_7 and r_{10} at $x^* = 0.2 \text{ m}$ is 0.02, 0.03, and 0.08 m, respectively.

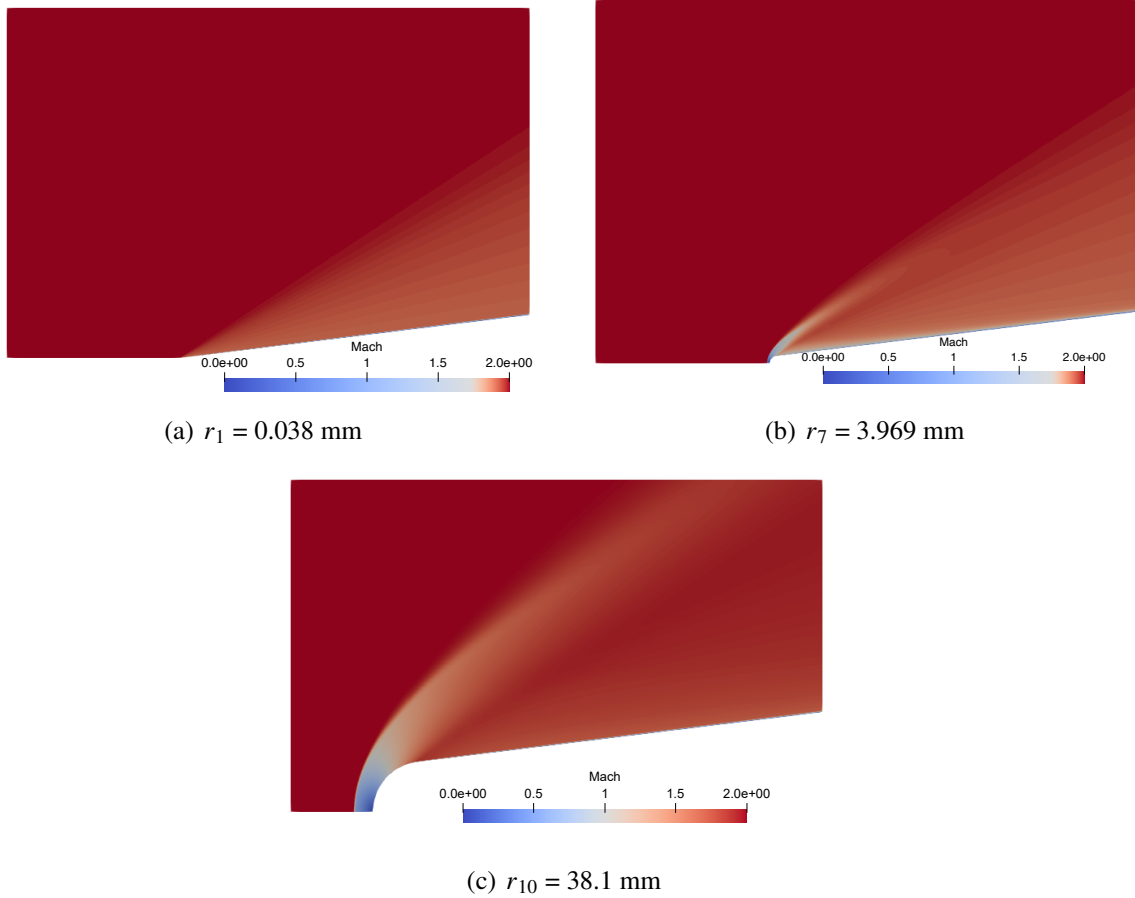
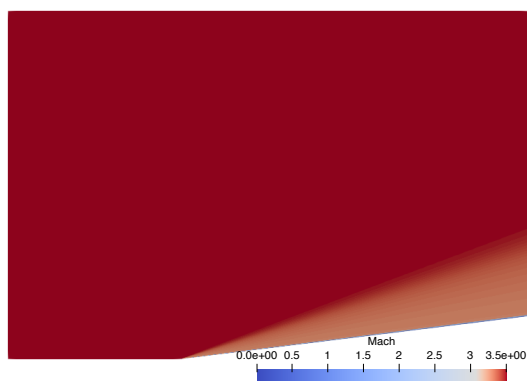
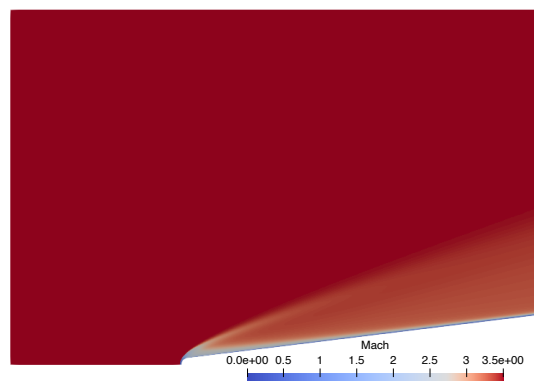


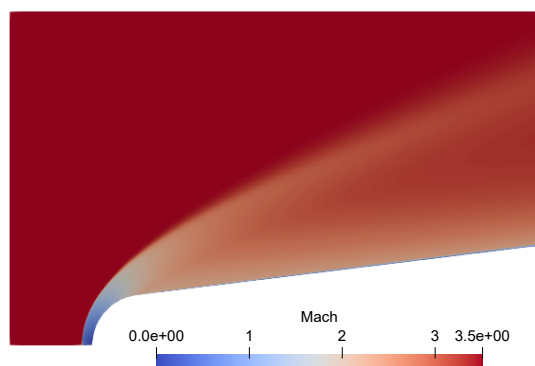
Figure 4-4. Mach number contours at r_1 , r_7 , and r_{10} at $M_\infty = 2$.



(a) $r_1 = 0.038$ mm

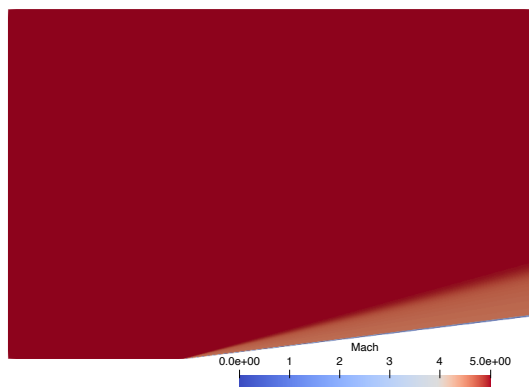


(b) $r_7 = 3.969$ mm

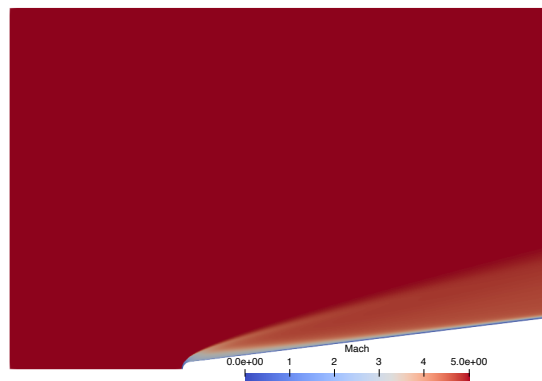


(c) $r_{10} = 38.1$ mm

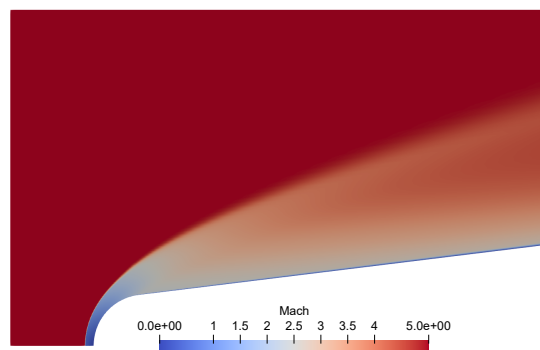
Figure 4-5. Mach number contours at r_1 , r_7 , and r_{10} at $M_\infty = 3.5$.



(a) $r_1 = 0.038$ mm



(b) $r_7 = 3.969$ mm



(c) $r_{10} = 38.1$ mm

Figure 4-6. Mach number contours at r_1 , r_7 , and r_{10} at $M_\infty = 5$.

4.1.2 Stability Computation and Validation

The stability parameters of our LST solver and results from Mayer [166] are shown in Table 4-2. The values of β and ω are given for the oblique wave and spatial stability computation. The eigenvalue $\alpha = \alpha_r + i\alpha_i$ is found from the previously described eigenvalue solver. The oblique wave angle (ψ) is computed via $\tan^{-1}(\beta/\alpha_r)$. Several factors affect the calculation of eigenvalues, which include the number of grid points, the discretization method, and the flow-fields. We note that there are some discrepancies between our calculation and the reference solution due to these factors.

Table 4-2. Stability Parameters.

	f^* (kHz)	n	α	ψ	u_p
Mayer [166]	23.415	21	350.1-22.5 i	N/A	N/A
LST	23.415	21	353.2-14.96 i	65.93°	0.64

Figure 4-7 shows the comparison of the normalized amplitude of eigenfunctions in the wall-normal direction between the LST and the results from Mayer [166], where the distance in the normal direction is normalized by the boundary layer thickness δ . Here, “Ref” indicates the results from Mayer [166]. It can be seen that similar variations of the eigenfunctions exist between our LST solver and Mayer [166]. There are discrepancies between LST and Mayer [166] results near the wall region for the u -velocity component and temperature eigenfunctions. The positions of the maximum value of \hat{u} are at $y_n/\delta = 0.6154$ and 0.5654 for LST and Mayer [166]. The error is 8.9% for the \hat{u} component. The error of \hat{T} is approximately 7.2%. The results of our LST prediction and that of Mayer [166] agree well after the position of the maximum value.

We focus on prediction of the unsteady coherent forcing on the vehicle surface due to instability waves from the Mack first mode within the present work. We restrict the frequency (f^*) to be less than 75 kHz for the flow conditions and the azimuthal modes less than 40 because the first modes are dominant at low supersonic speeds within these ranges. Figure 4-8 shows the maximum growth rates over all frequencies and azimuthal modes examined for conditions shown in Table 4-1. It can be seen that the difference of maximum growth rates along the streamwise direction are less than 1 (1/m) for $r_1 = 0.038$ to $r_4 = 0.38$ mm, which demonstrate that the very

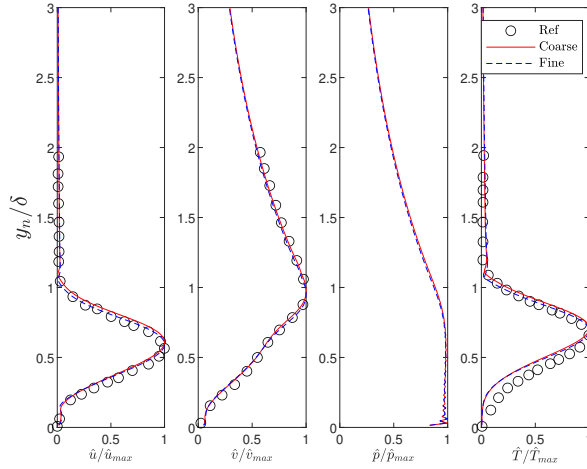


Figure 4-7. Comparison of normalized amplitudes of eigenfunctions between the LST prediction and the results from Mayer (Ref).

small nose radius will not have too many effects on the maximum growth rate. From $r_5 = 1.14$ to $r_7 = 3.969$ mm, the growth rates decrease monotonically as the nose radius increases at $M_\infty = 3.5$ and 5. However, the trend does not appear at $M_\infty = 2$. In addition, there are no trends for $r_7 = 3.969$ to $r_{10} = 38.1$ mm especially in the region close to the leading edge. This is due to the formation of the entropy layer. For leading edge geometries of $r_1 = 0.038$ to $r_6 = 1.905$ mm, there is an obvious peak in growth rate, then growth rates become smaller after the peak position at $M_\infty = 3.5$ and 5, which shows the instability waves firstly are amplified, then less amplified, and decayed finally within the physical sense. After the locations of peak value for r_7 to r_{10} , the values of maximum grow rates are changed less relative to the case of r_1 to r_6 . Specifically, the positions of peak value of each case are shown at Table 4-3. On the other hand, the value of growth rates maintain in the range between 18 and 23 for r_1 to r_6 after the locations of peak value at $M_\infty = 2$ except $x^* = 0.54$ m of r_5 due to numerical error.

Table 4-3. Peak position of maximum growth rates of each case (m).

M_∞	r_1	r_2	r_3	r_4	r_5	r_6	r_7	r_8	r_9	r_{10}
2.0	0.31	0.31	0.26	0.26	0.31	0.54	0.50	0.47	0.47	0.34
3.5	0.14	0.14	0.14	0.18	0.23	0.31	0.46	0.3	0.26	0.55
5.0	0.10	0.14	0.10	0.10	0.18	0.34	0.75	0.71	0.34	0.46

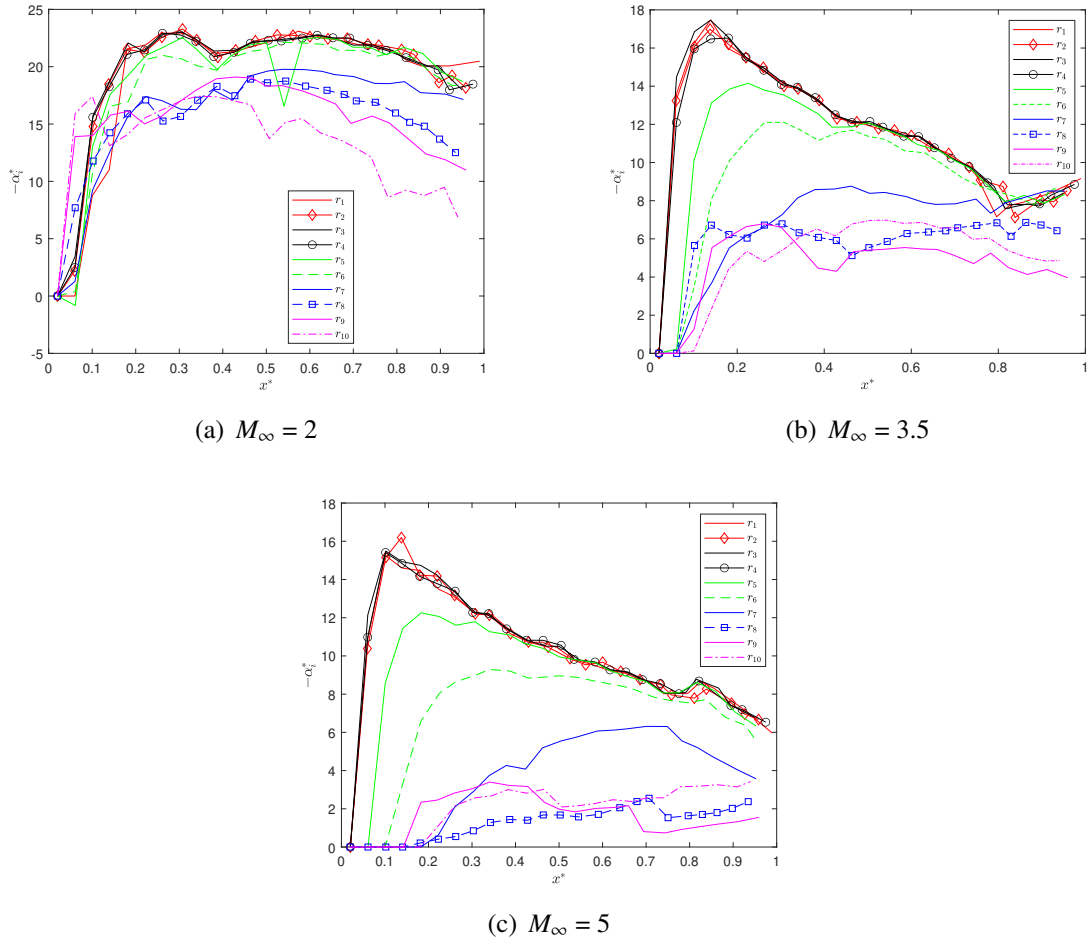


Figure 4-8. Comparison of maximum growth rate over all frequencies and spanwise wavenumber along streamwise direction for r_1 to r_{10} at $M_\infty = 2, 3.5$ and 5 .

4.1.3 Spatial Coherence

We now present spatial coherence predictions relative to separation distance and radial frequency. Figures 4-9, 4-10, and 4-11 show the spatial coherence for nose radii from r_1 through r_{10} at $M_\infty = 2, 3.5$, and 5 , where the reference point ($\xi = 0$) is the position of maximum growth rate of each case of Fig. 4-8. For example, spatial coherence shows similar trends for r_1 through r_4 . The separation distance between the reference point for higher spatial coherence becomes smaller as the frequency increases. The larger nose radii shows higher spatial coherence within a smaller range of frequencies. Secondly, the distribution of high spatial coherence in the frequency domain is different at each M_∞ . The results of spatial coherence at $M_\infty = 2$ (Fig. 4-9) are at

higher value when $\omega^* \leq 100$ kHz. A narrow band of higher spatial coherence of r_1 to r_7 occurs when $\omega^* \geq 100$ kHz. However, there are unexpected bands at r_8 to r_{10} . The results at $M_\infty = 3.5$ and 5.0 are similar. The frequency range of high spatial coherence is from 50 kHz to the maximum frequency at r_1 to r_4 . The lower frequency band becomes smaller when nose radii increase. However, the upper frequency band of r_5 and r_6 does not change at $M_\infty = 5$. Several unexpected bands also appears for r_{10} at $M_\infty = 3.5$ and r_8 at $M_\infty = 5$.

Amplified instability waves show higher spatial coherence than damped instability waves, which create the distribution of the spatial coherence within Figs. 4-9, 4-10, and 4-11. The values of growth rates mainly depend on the non-dimensional frequency, $\omega = 2\pi f^*(\nu_e^* x^*/u_e^*)^{1/2}/u_e^*$, and the instability waves are amplified when ω is within a range, i.e. $0.02 \sim 0.06$. The non-dimensional frequency is proportional to the dimensional frequency, streamwise locations, length scale, and inversely proportional to velocity. Specifically, for the nose radii r_1 through r_4 at fixed M_∞ , the reference points (x^*) are smaller so that the instability waves are amplified at higher dimensional frequencies. The length scale increases as the nose radii increases at fixed M_∞ , hence, the frequency range becomes smaller as nose radii increases. The frequency range becomes larger for higher M_∞ .

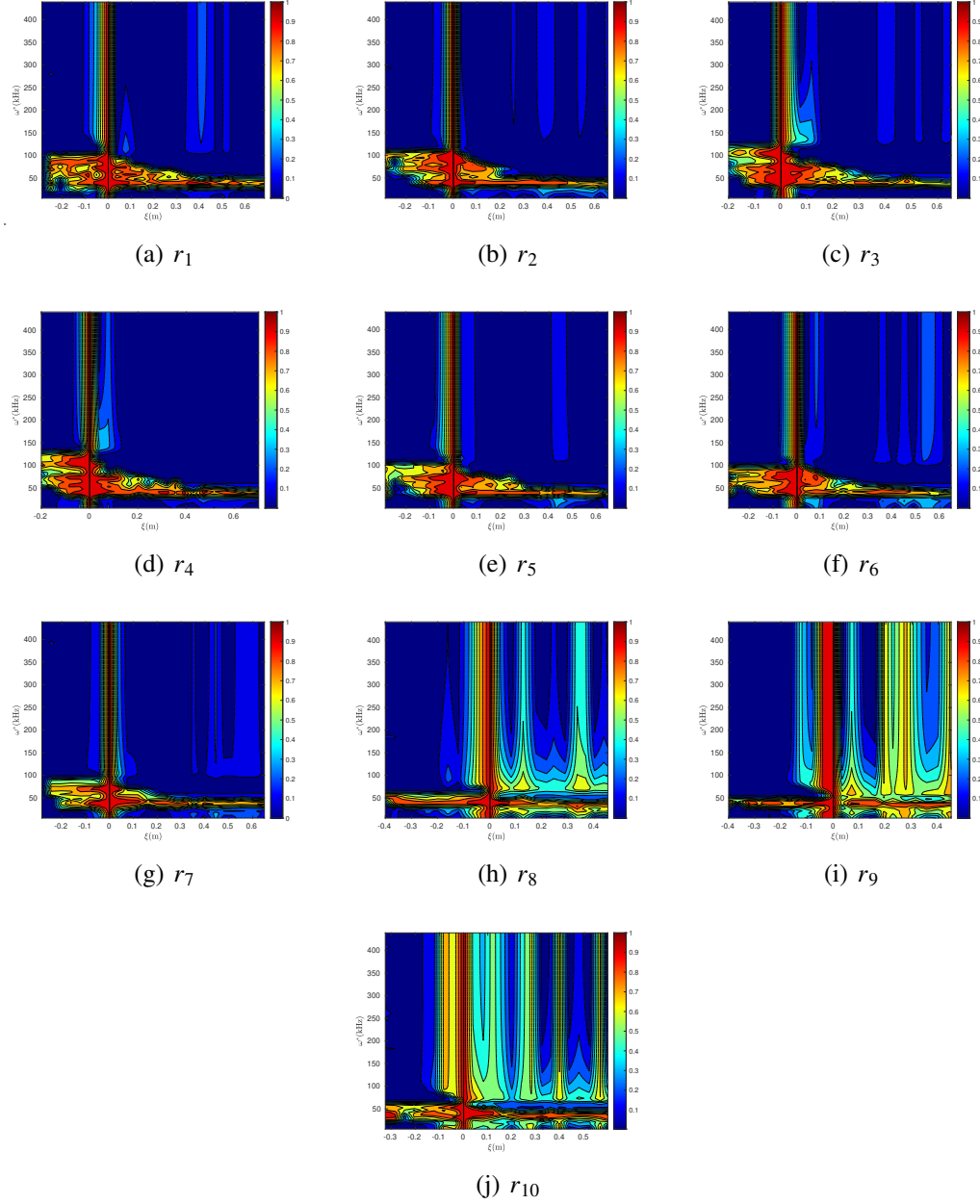


Figure 4-9. Spatial coherence of different nose radii from r_1 to r_{10} at $M_\infty = 2$, where the reference point of each case is at the maximum grow rate along streamwise direction.

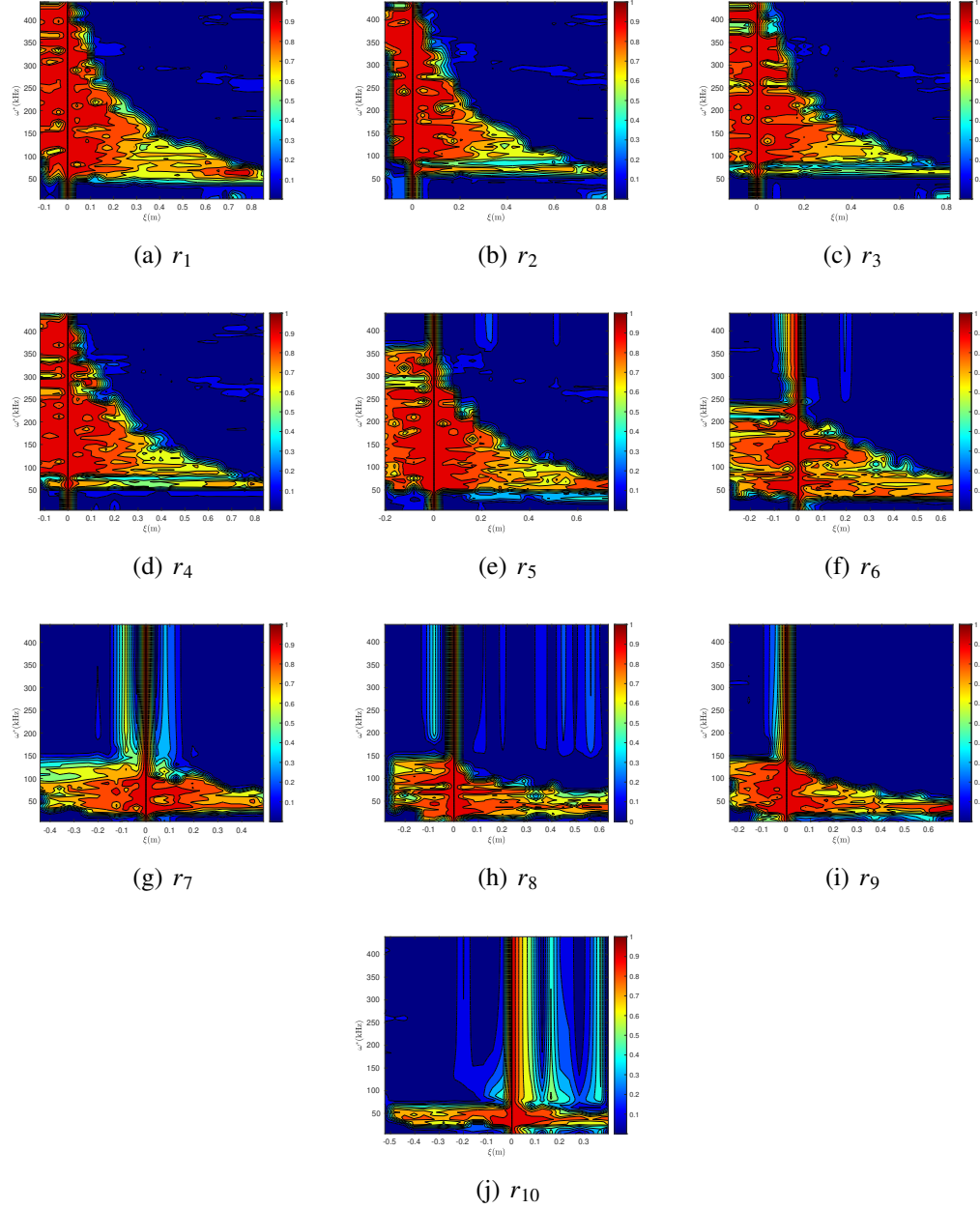


Figure 4-10. Spatial coherence of different nose radii from r_1 to r_{10} at $M_\infty = 3.5$, where the reference point of each case is at the maximum grow rate along streamwise direction.

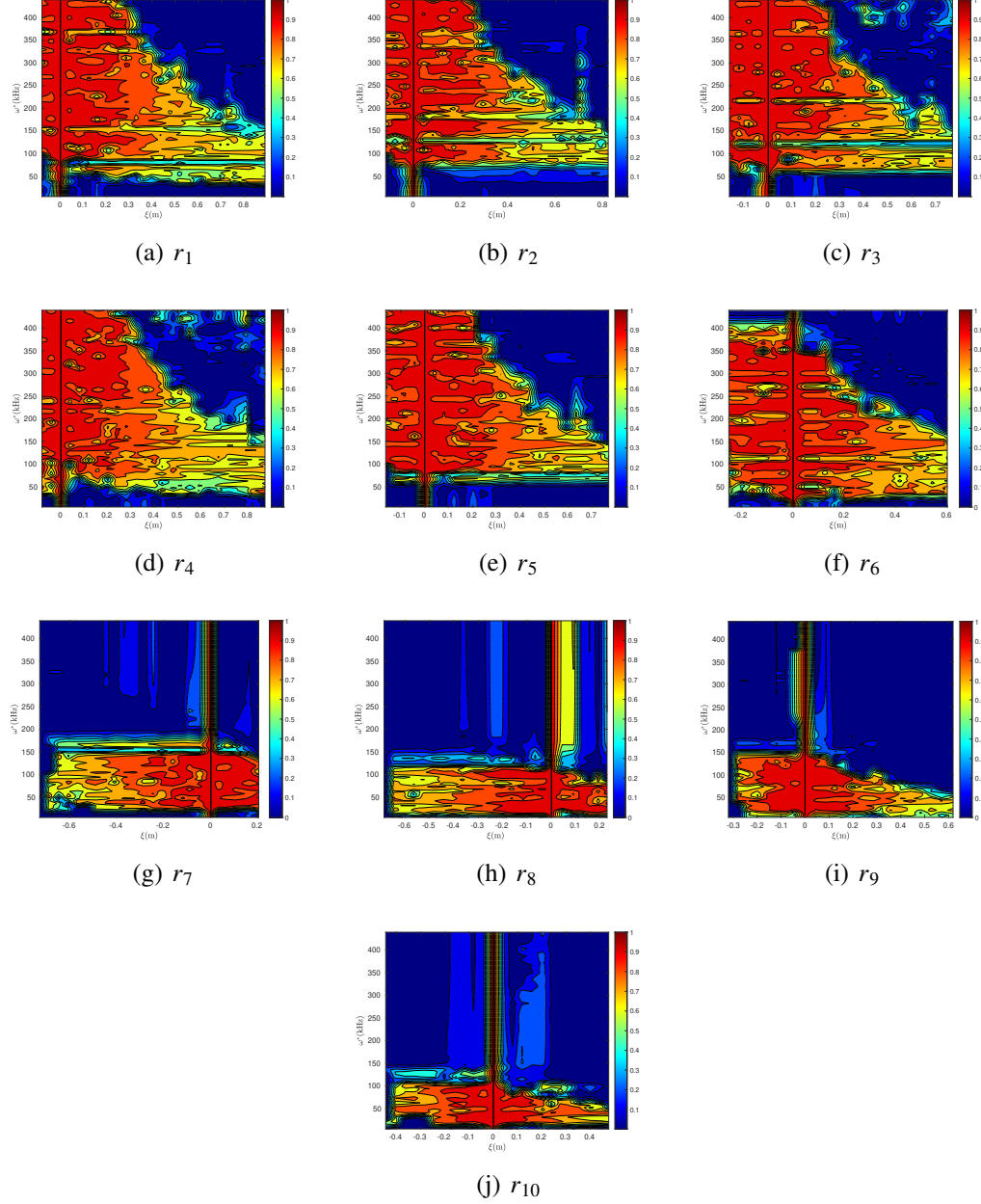


Figure 4-11. Spatial coherence of different nose radii from r_1 to r_{10} at $M_\infty = 5$, where the reference point of each case is at the maximum grow rate along streamwise direction.

4.2 The Effects of Plasma Actuator Model

4.2.1 Validation and Flow Structures

We validate our implementation of the plasma actuation model via comparison with the ramp flow of Poggie [138, 137]. The ramp configuration of Poggie [138, 137] consists of an initial flat plate of length $L = 0.439$ m and width $W = 0.61$ m mounted parallel to the freestream. The wall turns at an angle of $\theta = 24^\circ$. The freestream conditions are $M_\infty = 14.1$, $T_\infty = 72.28$ K, and $Re_\infty(1/m) = 238,040$. The parameters of the plasma actuator model (Eqn. (2-91)) are set as $Q = 100$ W, $x_c = L/2$, $y_c = 0.008$ m, $z_c = W/2$ m, and $a = 0.005$ m. We reduce the computation by scaling half size of the ramp configuration. The wall is set as isothermal, and the temperature is $T_w = 297.46$ K. Figure 4-12 shows the grid distribution. The grid is finer in the inlet and the corner region to resolve the base flow (Fig. 4-12(a)). The grid is also finer in the region around the plasma actuator model for flow with plasma actuation (Fig. 4-12(b)). The number of grid points are $181 \times 61 \times 90$ and $196 \times 61 \times 90$, respectively. The number of grid in the cross-stream direction is set to ensure the value of Y^+ less than 1.

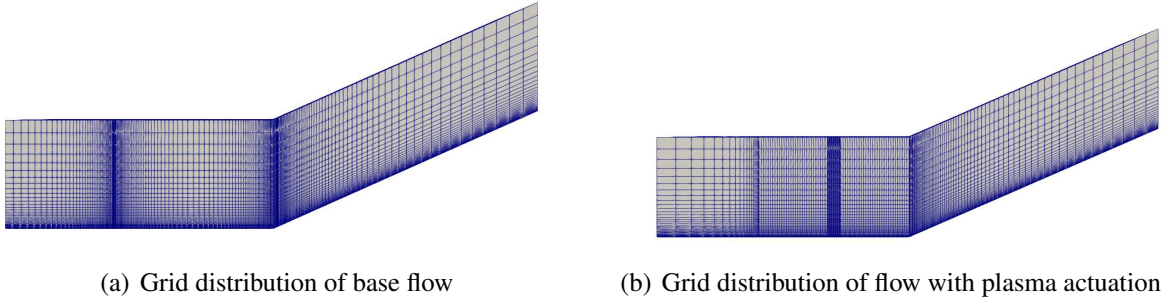


Figure 4-12. Grid distribution.

The comparison of pressure coefficient, $C_p = 2p_w/\rho_\infty u_\infty^2$, between the simulations and experimental measurement is shown in Fig. 4-13. The comparison between the results of the base flow and experiment has a maximum difference of approximately 0.23 at $x/L = 1.42$. This is likely due to the closure not accurately predicting the correct separation point. On the other hand, the value of C_p of flow with a source at $x/L = 1.29$ is 0.356, which is lower than the that of base flow of 0.465. This is consistent with results of [137, 141]. In addition, the values of C_p of flow

with the actuator model are larger near the position of x_c . This observation is expected based on experimental results [130].

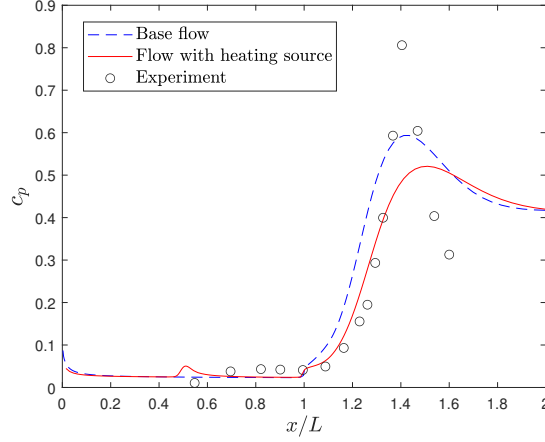
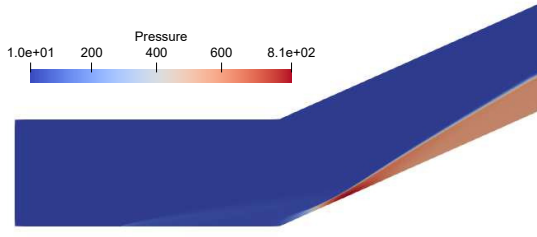
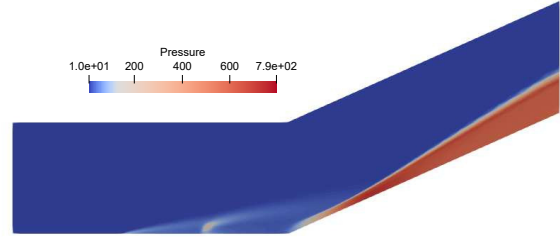


Figure 4-13. Comparison of pressure coefficient of base flow and flow with plasma actuator model.

We show contours of pressure and temperature of flow-fields with and without actuation in Figs 4-14 and 4-15. These contours are in the plane $z = z_c$. The actuator causes an increase of pressure around the source region (Fig. 4-14(b)) and a conic shock forms in front of the actuator, which explains the localized increasing C_p by 0.05 as shown in Fig. 4-13. It can be seen that the plasma actuator model generates a localized region with high temperature up to 3500 K above the plate surface as shown in Fig. 4-15(b) (scaled to 2000K for comparison). The temperature of the region behind x_c also increases because the heat is convected to downstream regions. Figure 4-16 shows the temperature distribution at the surface $y = y_c$. There is a limited region in the z -direction with higher temperature due to the added plasma actuator model. The affected range in the z -direction is between $z - z_c \sim [-0.01 \quad 0.01]$, which is consistent with the distributions of plasma actuator. The temperature decreases by 70.8% relative to the center of the plasma actuator. In addition, the heat is transferred to the end of the ramp, which has a distance of 0.48 m to the actuator.

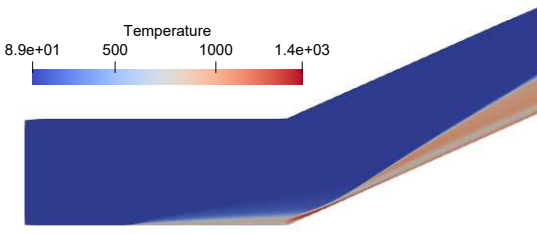


(a) Pressure distribution

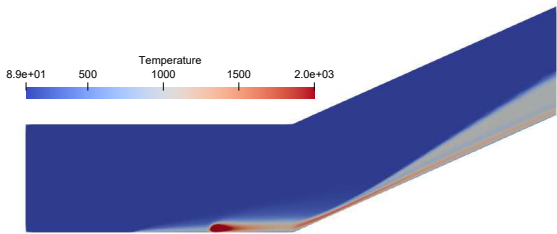


(b) Pressure distribution with heating source

Figure 4-14. Pressure distribution at the surface z_c .

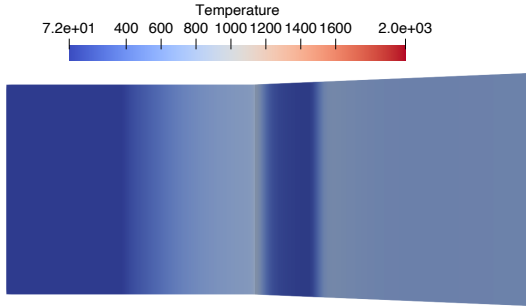


(a) Temperature distribution

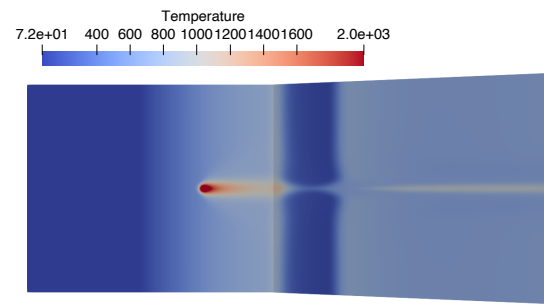


(b) Temperature distribution with heating source

Figure 4-15. Temperature distribution at the surface z_c .



(a) Temperature distribution



(b) Temperature distribution with heating source

Figure 4-16. Temperature distribution at the surface y_c .

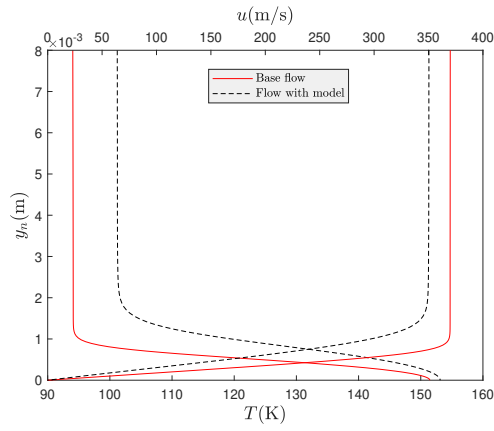
4.2.2 Cone Flows with plasma actuator

We now examine steady flows over cones with plasma actuation. The mean flow-field over the cone with actuation is computed with SU2. We use the same boundary conditions as the base flow described in Section 4.1. The computational domain is refined near the plasma actuator region. We modified the plasma actuator model by eliminating z -direction as $S_v = \frac{Q}{\pi a^2} \exp\left(-\frac{d^2}{a^2}\right)$

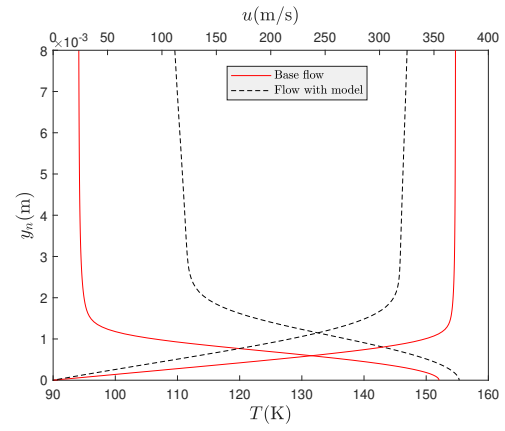
and $d = \sqrt{(x - x_c)^2 + (y - y_c)^2}$. The parameters of the plasma actuator model are $Q = 100$ W, $a = 0.005$ m, $y_c = 0.008$ m, and x_c is set as the position of maximum growth rate of each case (Fig. 4-8) according to the investigations of Corke et al. [136].

4.2.2.1 Mean Flow-Field Modifications

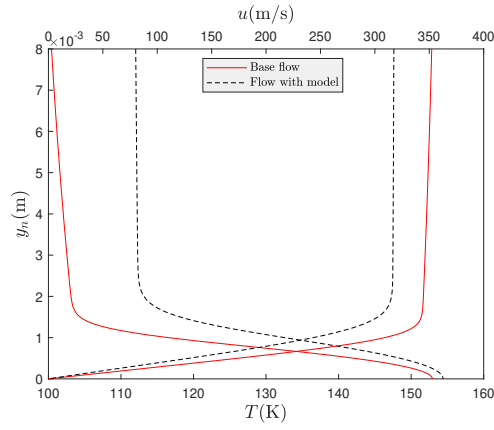
We first examine modifications to the steady flow-field. Figures 4-17, 4-18, and 4-19 show the comparison of temperature and velocity in the cross-stream direction for r_1 , r_7 , and r_{10} at $x^* = x_c$ at $M_\infty = 2, 3.5$, and 5, where the y -axis is extended to y_c . The solid lines are the predictions from the base flow, and the dash lines are the predictions of the flow with actuation. It can be seen that the temperature increases from the cone surface and the velocity become smaller for each case. For example, the temperature differences between the flow with plasma actuator model and base flow at $M_\infty = 3.5$ of each nose radii around of $y^* = y_c$ are 20, 55.2, and 38.4 K, respectively. The velocity difference of each case around $y^* = y_c$ are 15.2, 91.1, and 68.7 m/s, respectively.



(a) $r_1 = 0.038$ mm

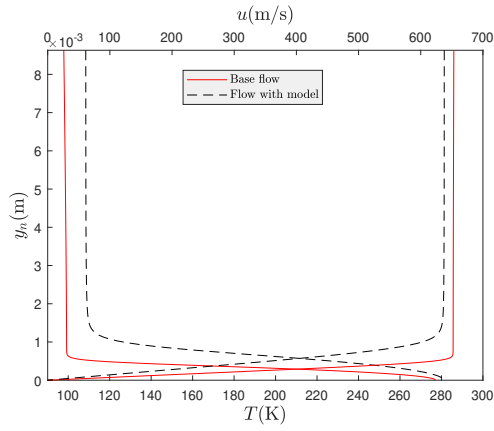


(b) $r_7 = 3.969$ mm

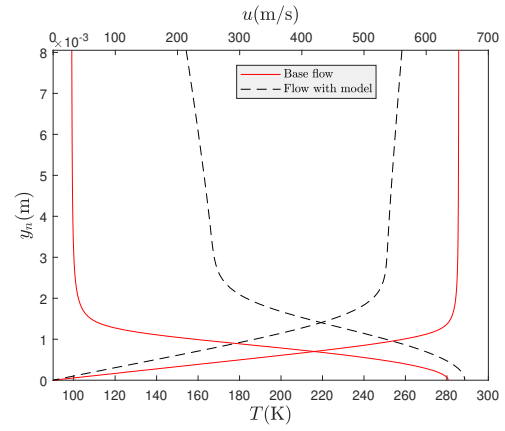


(c) $r_{10} = 38.1$ mm

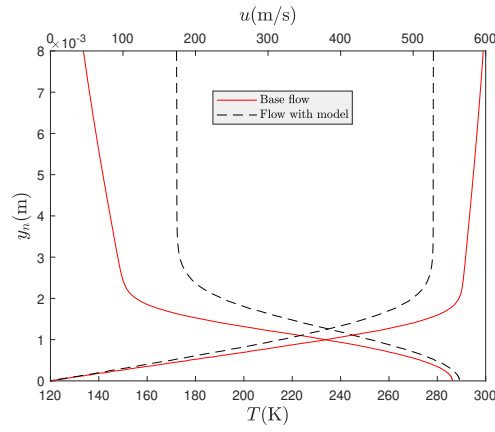
Figure 4-17. Comparison of temperature and velocity between base flow and flow with plasma actuator model of r_1 , r_7 , and r_{10} at $x^* = x_c$ at $M_\infty = 2$.



(a) $r_1 = 0.038$ mm

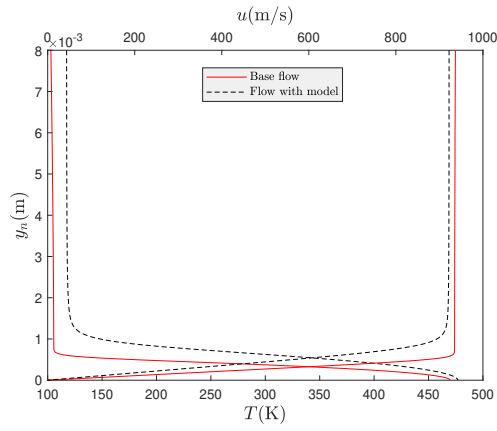


(b) $r_7 = 3.969$ mm

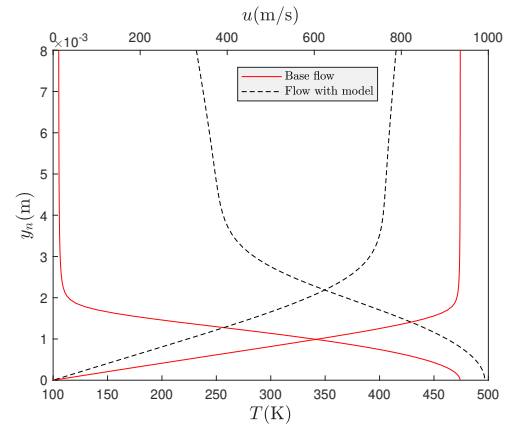


(c) $r_{10} = 38.1$ mm

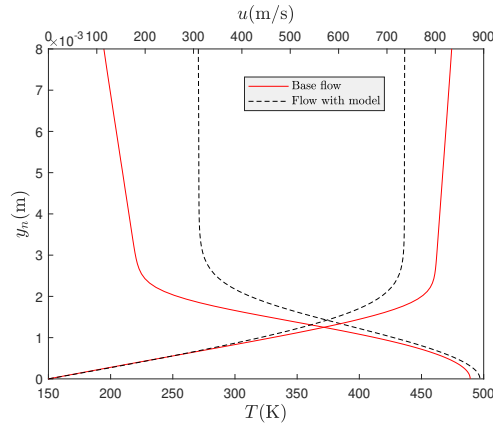
Figure 4-18. Comparison of temperature and velocity between base flow and flow with plasma actuator model of r_1 , r_7 , and r_{10} at $x^* = x_c$ at $M_\infty = 3.5$.



(a) $r_1 = 0.038$ mm



(b) $r_7 = 3.969$ mm



(c) $r_{10} = 38.1$ mm

Figure 4-19. Comparison of temperature and velocity between base flow and flow with plasma actuator model of r_1 , r_7 , and r_{10} at $x^* = x_c$ at $M_\infty = 5$.

We compare the temperature distribution in the wall normal direction at $x^* = x_c$ for r_1 to r_{10} at $M_\infty = 2, 3.5$, and 5 because the main effect of plasma actuation adds an equivalent heating source. Figure 4-20 shows the temperature difference between the flow with the plasma actuator model (T_h) and base flow (T_b) related to the temperature of the base flow at $x^* = x_c$, where the x -axis is distance from the cone surface normalized with the boundary layer thickness (δ) of the base flow. The maximum value of the relative temperature difference becomes larger as freestream Mach number increases. There are two peaks for the r_1 to r_5 cases, which we refer to as the first and second peaks, where the positions of the two peaks are at the boundary layer edge and shock layer edge, respectively. The value of the first peak is larger than that of the second peak because the center of the plasma actuator is more closer to the boundary layer edge. The values of relative temperature difference between the first and second peak become larger at r_6 due to the presence of an entropy layer. A new peak appears between the first and second peaks at r_8 to r_{10} . The value of the new peak is larger than the first and second peaks at $M_\infty = 3.5$ and 5 . For example, the value of new peak is 1.2 for r_9 for $M_\infty = 5$, whereas that of second value is 0.64 . Based on our predictions, the effect of high freestream Mach number is relatively strong compared to lower Mach numbers on the maximum relative temperature difference.

4.2.2.2 Stability Modifications

Figure 4-21 shows the maximum growth rate distribution in the streamwise direction with actuation for r_1 to r_{10} at $M_\infty = 2, 3.5$ and 5 , respectively. In general, the growth rates decrease with actuation except r_9 and r_{10} at $M_\infty = 2$, which shows the instability waves are stabilized with actuation. It can be seen that there is no obvious trends of the growth rate distributions with increasing nose radii. We believe this is due to the different positions of plasma actuator model at each nose radii. However, we can still obtain several trends. For r_1 to r_4 , the positions of plasma actuator are same or varies between -0.04 to 0.04 m. It can be seen that the values of maximum growth rate decrease as the nose radii increase at $M_\infty = 3.5$ and 5 , which shows that the flow-fields with actuation are stabilized more intensively with larger nose radii. On the other hand, at $M_\infty = 2$, the values of maximum growth rates of r_1 to r_4 vary less than 4 before $x^* = 0.3$

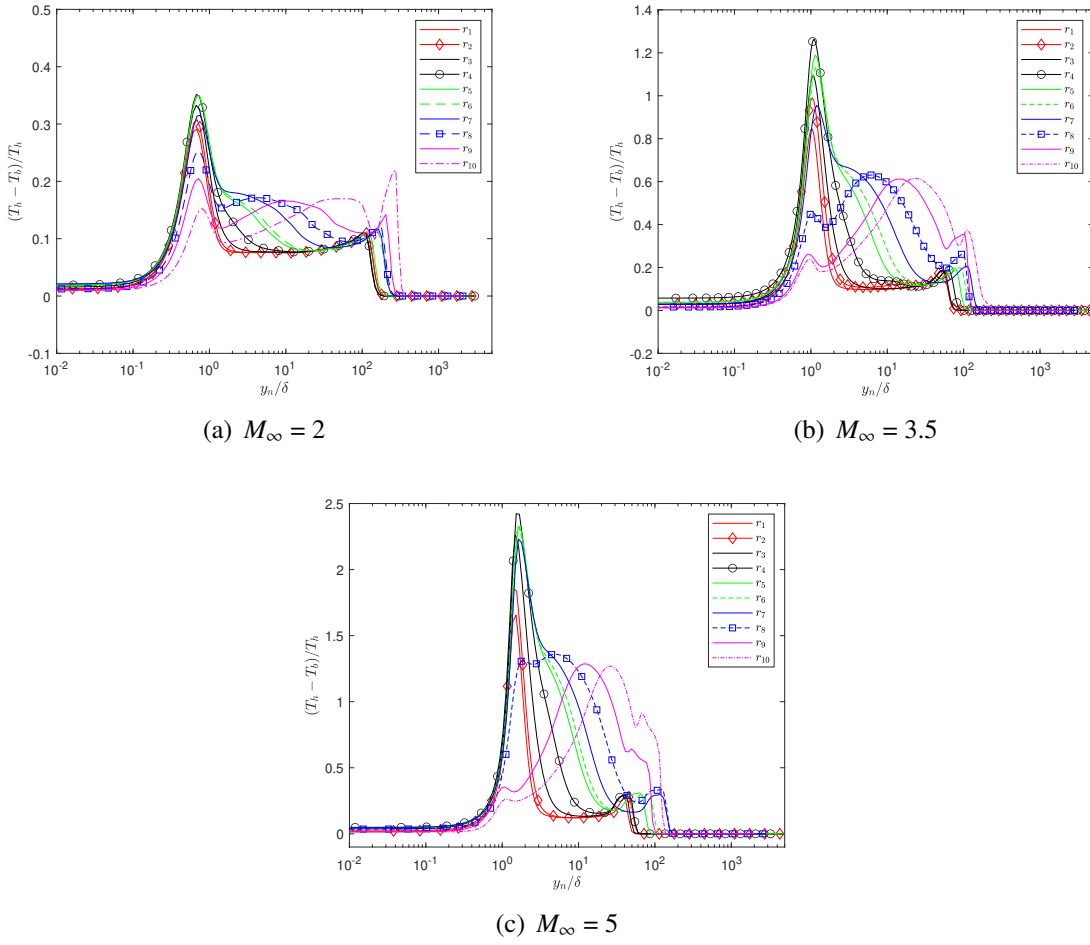


Figure 4-20. Relative temperature difference caused by the plasma actuator at $x^* = x_c$ for r_1 to r_{10} at $M_\infty = 2, 3.5$, and 5 .

m, which is the position of the plasma actuation of r_1 and r_2 . Based on the phenomenon, we think that the effects of nose radii is notable for flow with actuation at higher free-stream Mach number.

Figure 4-22 shows the relative difference of maximum growth rates between the base flow and flow with actuation, where the x -axis is normalized with x_c . The growth rate difference is normalized with maximum growth rate of the base flow-fields for each conditions. These results illustrate the effect of the plasma actuator model on stability in the positions before and after the position of the plasma actuator model. For smaller nose radii (r_1 to r_4), the higher value of the relative difference is located close to the heating source ($0.5 < x^*/x_c < 1.5$) at $M_\infty = 3.5$ and 5 . However, the reverse effect is shown at $M_\infty = 2$. One potential reason is that the value of x_c of

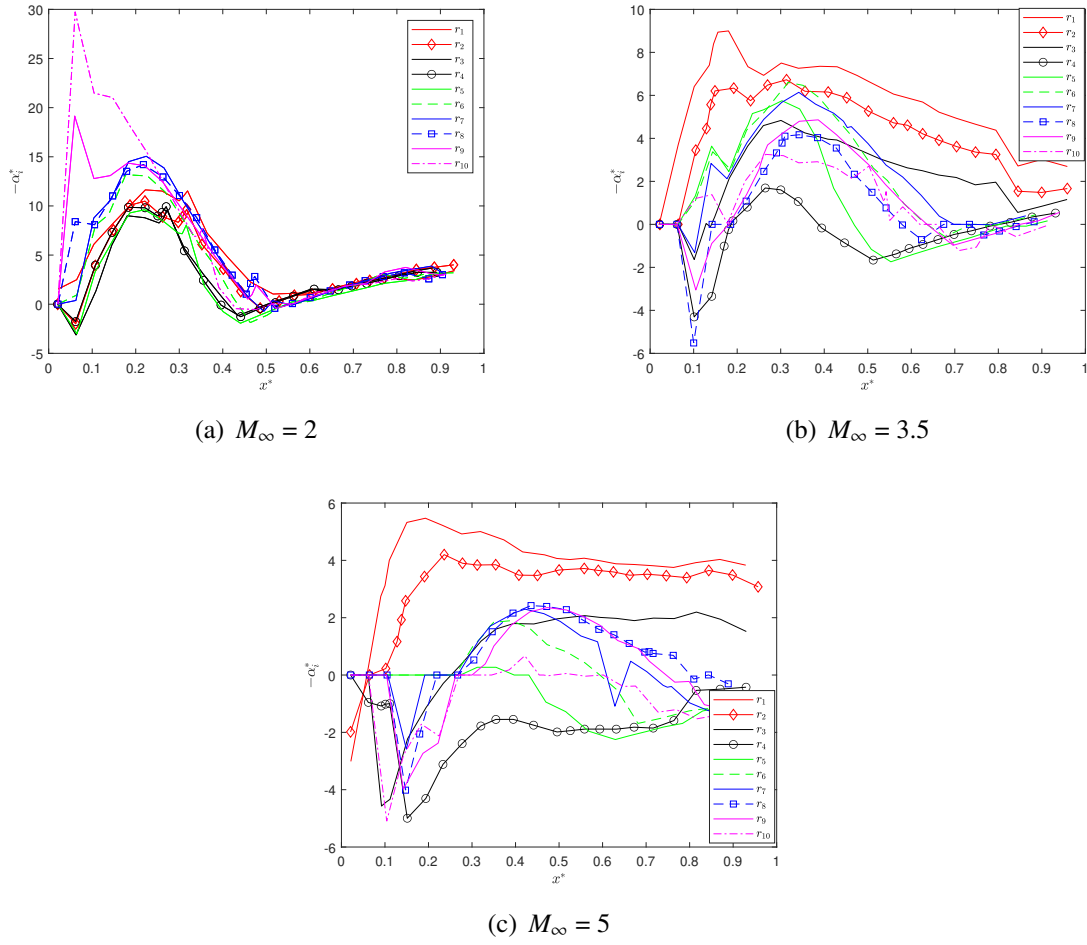


Figure 4-21. Comparison of maximum growth rate over all frequencies and spanwise wavenumber along streamwise direction of flow with plasma actuator model for r_1 to r_{10} at $M_\infty = 2, 3.5$ and 5 .

$M_\infty = 2$ is larger than that of $M_\infty = 3.5$ and 5 . It also can be seen that the effects of plasma actuation on stability at $M_\infty = 2$ within the region $x > x_c$ is stronger than that at $M_\infty = 3.5$ and 5 . For large nose radii (r_5 to r_{10}), the trends are difficult to ascertain. The interaction of the entropy layer and plasma actuation create a complicated nonlinear trend.

Figures 4-23, 4-24, and 4-25 show the spatial coherence of flow with actuation for nose radii from r_1 through r_{10} at $M_\infty = 2, 3.5$, and 5 . The actuated flows have smaller separation distance with high spatial coherence than that of base flow at the same frequency. For example, for r_5 at $M_\infty = 3.5$, the separation distance is 0.68 m for base flow at $\omega^* = 75$ kHz, however, that value of actuated flow is 0.12 m. Additionally, the actuated flows show high spatial coherence

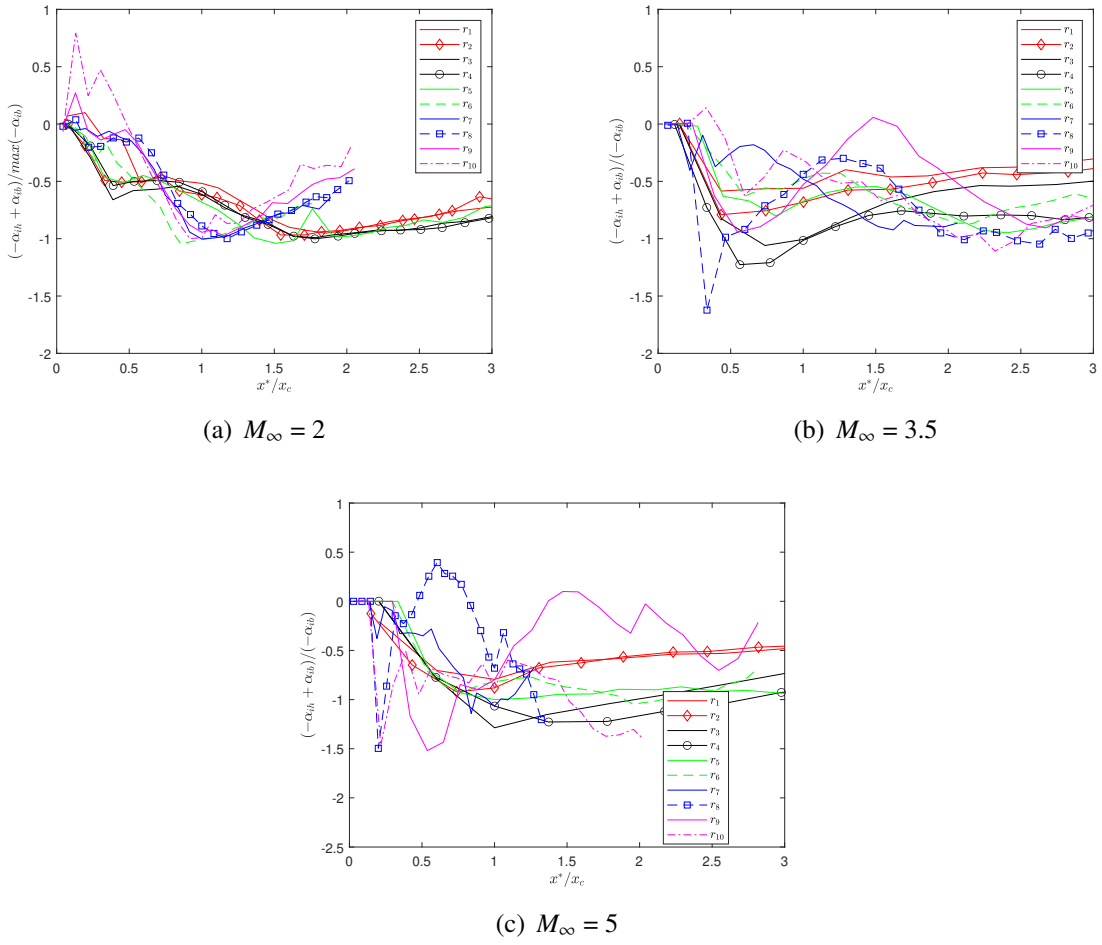


Figure 4-22. Relative difference of maximum growth rate along streamwise direction for r_1 to r_{10} at $M_\infty = 2, 3.5$ and 5 .

within a smaller frequency range compared with the base flow. For example, at $M_\infty = 3.5$ with radii r_5 , the frequency range with high spatial coherence for base flow is between 26 to 371 kHz, whereas the range of flow with plasma actuator is 15 to 105 kHz. It also can be seen that the lower and upper limit frequency with high spatial coherence of actuated flow become smaller than that of base flow. The reason is that the value u_e^* of the flow with plasma actuation is smaller than that of base flow. Therefore, the frequency needs to become smaller to keep the value of ω to have the instability wave amplified. The decrease of separation distance can also be explained via this way.

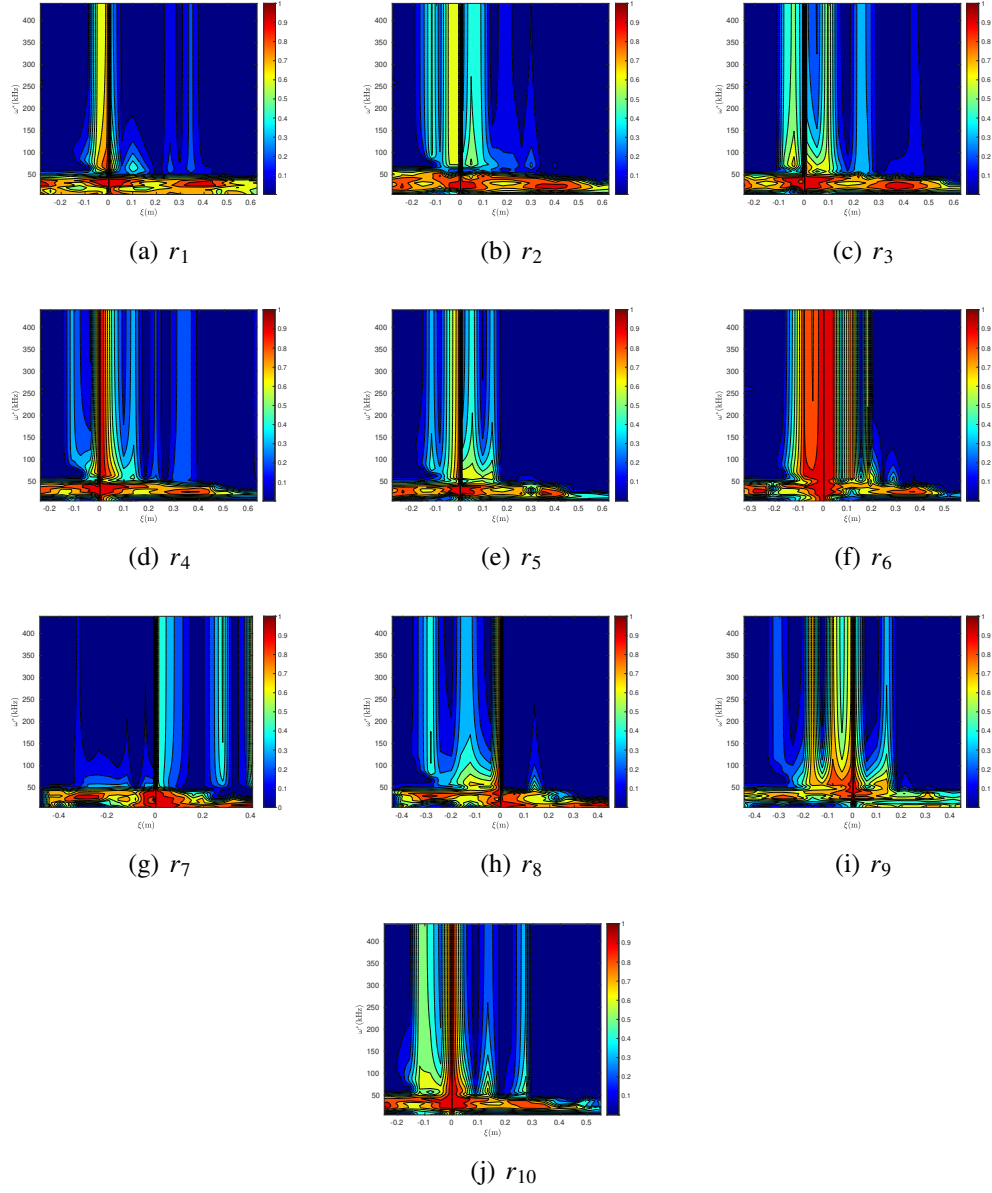


Figure 4-23. Spatial coherence of flow with plasma actuator model for r_1 to r_{10} at $M_\infty = 2$.

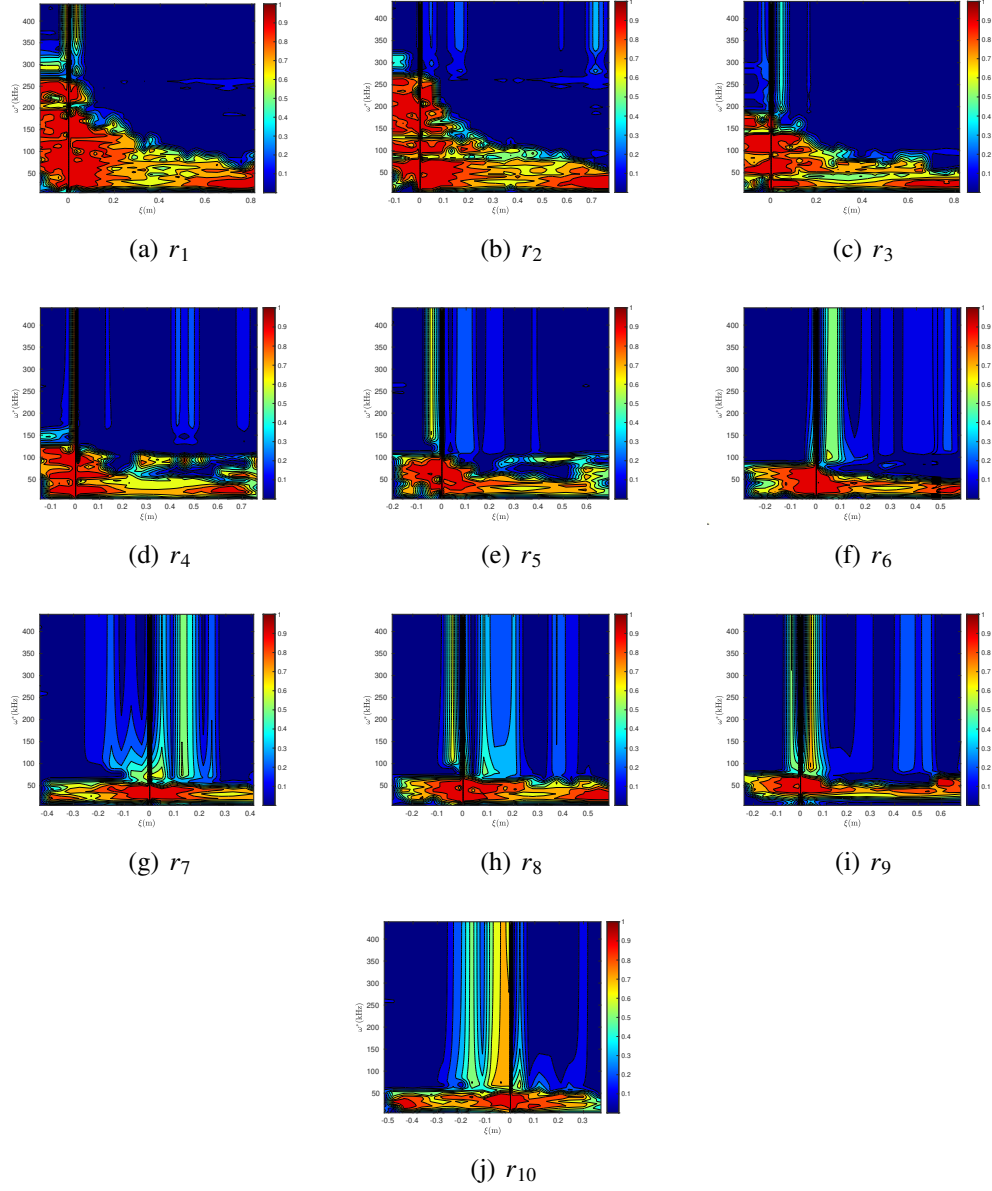


Figure 4-24. Spatial coherence of flow with plasma actuator model for r_1 to r_{10} at $M_\infty = 3.5$.

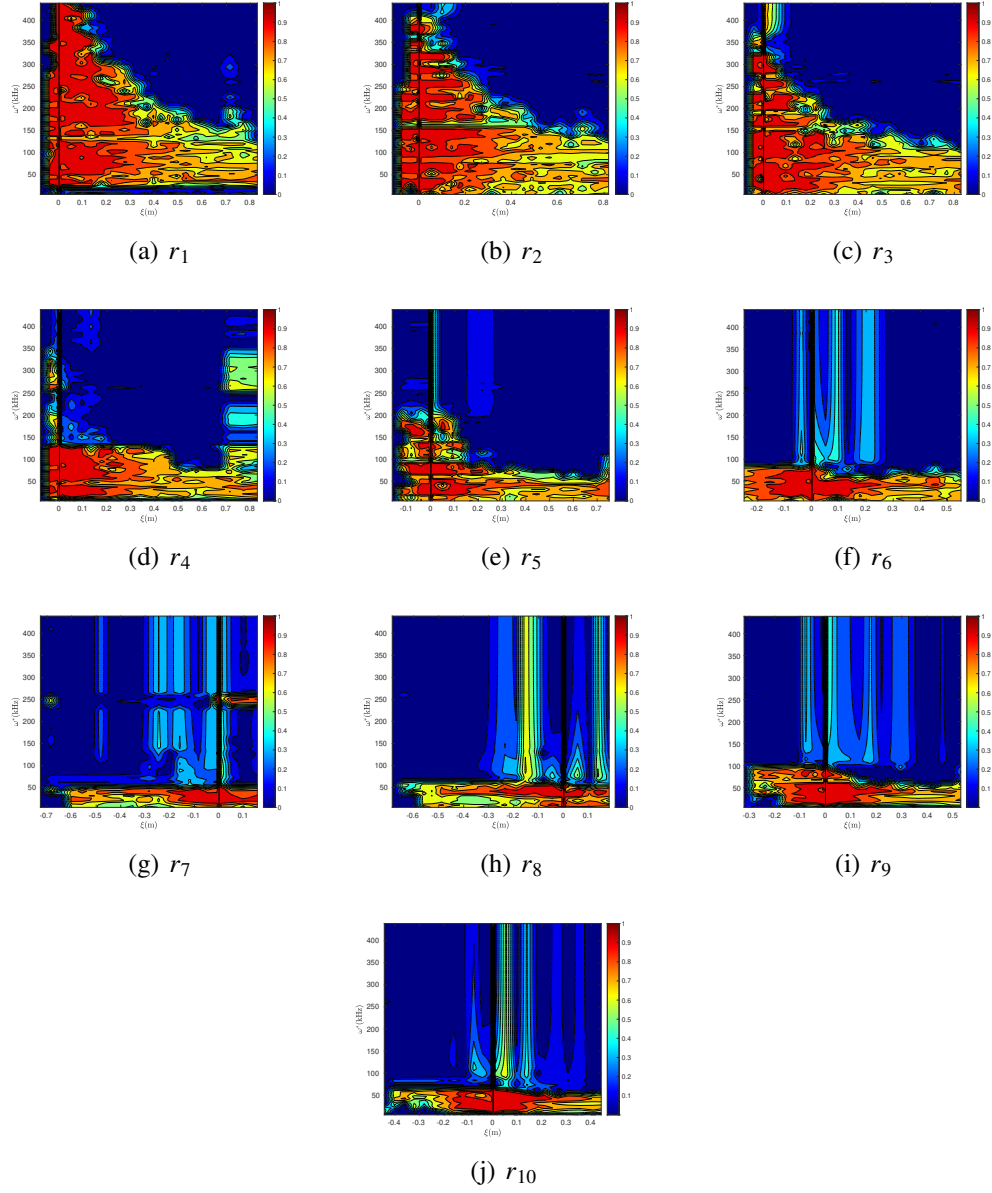


Figure 4-25. Spatial coherence of flow with plasma actuator model for r_1 to r_{10} at $M_\infty = 5$.

CHAPTER 5 SUMMARY AND FUTURE WORK

5.1 Summary of Results

5.1.1 Jet Flows

Large-scale turbulent structures are the dominant noise sources in the downstream direction within jet flows. In this dissertation, we apply instability wave models to represent the effects of large-scale turbulent structures within the turbulent jet. The near-field dynamics and far-field noise in both the downstream and upstream directions are calculated and analyzed. The previous chapters reviewed the method used, such as the POD method to identify the large-scale turbulent structures. The instability wave amplitudes are calculated with the far-field noise predicted by the KS method. The jet noise prediction via the KS method is based on an LES database.

The results and discussion are shown for two jet flows in different configurations. One is a round convergent nozzle with an under-expanded condition from the SHJAR database. The other is a bi-conic nozzle operating at an over-expanded condition, which is the SERDP case. The corresponding operating conditions are shown in Table 5-1.

Table 5-1. Operating Conditions.

Nozzle	NPR	TTR	T_j [K]	M_j	u_j [m/s]	Re_D
SHJAR	3.514	3.20	670.4	1.47	762.39	6.26×10^5
SERDP	2.77	1.00	218.9	1.30	385.62	1.60×10^6

We examine the properties of the noise from instability waves, such as the directivity in the far-field and the dominance of azimuthal modes for the SHJAR case. The results show that the instability wave theory captures the directivity pattern of large-scale turbulent structures, which dominates the downstream radiation direction. Instability theory is able to quantify the radiation of noise from the large-scale turbulent structures in the upstream direction, where fine-scale turbulent structures dominate. The SPL from instability waves are lower by approximately 10 to 30 dB relative to experiment as expected. Predictions using instability wave theory in terms of azimuthal decomposition verify that the screech tone can alter the dominant mode shape of jet noise from an axisymmetric mode to helical mode. Additionally, the phase speed in the streamwise direction oscillates strongly similar to mean flow variations due to the existence of the

shock cell structure. This is unlike supersonic jets that operate on-design or subsonic jets, which do not contain shock waves.

The POD method is used to extract the most energetic part from LES results and are applied to calibrate the amplitudes of the instability wave models. Even though the results are improved after calibration with the reconstructed flow-fields with selected POD modes, the region after the potential core cannot be matched. The nonlinear interaction mechanism at the lower frequencies cannot be captured with linear theory.

The newly implemented Kirchhoff surface prediction scheme is validated against experimental measurement by comparison with acoustic spectra for the SERDP case. The radiation from the instability wave model are used to calculate far-field noise signal statistics including coherence and cross-correlations. The auto-correlation and cross-correlation results from the predictions of instability waves have similar statistics relative to the experiment at the downstream direction ($\psi = 140^\circ$ and 130°). The correlations maintain a similar shape at other observation angles, which shows the sound at various observation angles is from the similar noise source. We compare statistics of near-field upstream radiation at $\psi = 50^\circ$ with downstream far-field radiation from $\psi = 140^\circ$ to 60° . As expected, there is high coherence of the predictions from instability waves between the near-field upstream and far-field radiation, which reside between 0.4 and 0.62. In summary, the instability waves can be used to represent the onset of large-scale turbulent structures and associated radiation statistics.

5.1.2 Boundary Layer Flows

The amplitude and location of excitation strongly affect the vibration and radiated noise of a structure. In general, the excitation is expressed in terms of a single power spectral density and spatial coherence. In this dissertation, we apply the LST within boundary layer flows to obtain the instability wave solutions, construct the pressure fluctuations, and obtain the corresponding spatial coherence of pressure fluctuations on the cone surface. The time-averaged velocity field, pressure, and temperature distribution over a cone with different conditions are computed via SU2 and validated by comparing with publicly available data in the literature. The base flow-field

(time-averaged Navier-Stokes equations) is used as an argument for the instability equations. These instability solutions include local wavenumbers and shape functions at varying azimuthal modes and frequencies at multiple streamwise locations. Additionally, the phenomenological plasma actuator model is added as the heating source to the energy equation and can be used to alter the flow-fields and stability properties. The previous chapters reviewed the formulas used, such as the reconstructed pressure time history based on the instability wave solutions.

The results and discussion are shown for cone flow with different nose radii and at different free-stream Mach numbers. The cone configuration is selected because it is similar with the leading edge geometries of flight-vehicle at high-speed. The nose radii cover from the sharp to blunt cones. The freestream Mach number is from the moderate supersonic to hypersonic regime. The specific conditions are shown in Table 4-1.

We examine the growth rate distribution of instability waves along the streamwise directions. The results show that the small leading edge radii for cones do not alter maximum growth rate. Large radii cones have lower growth rates due to a thicker boundary layer. In addition, the existence of entropy layer affect the properties of the first-mode. Therefore, the larger nose radii may not decrease the growth rates of the first mode and the corresponding effects. For example, the distribution of growth rates show complex behavior when the nose radii is larger than $r_7 = 3.969$ mm for $M_\infty = 3.5$. The spatial coherence of pressure fluctuations from instability waves with varying nose radii are computed and analyzed, where the reference point is selected as the peak value of growth rates distribution of each conditions. The results are presented in terms of the separation distance and frequency. The frequency range with higher spatial coherence decreases with nose radii. The frequency range with high spatial coherence of typical nose radii are shown in Table 5-2. The relative frequency ranges with high spatial coherence between r_1 and r_{10} are around 50%, 88.5%, and 76.9% for $M_\infty = 2, 3.5$, and 5, respectively.

Additionally, the effects of phenomenological plasma actuator model are also examined. Firstly, the flow structures of ramp configuration are investigated. The results show that the phenomenological plasma actuator model can add local heating to the flow-field. The position

Table 5-2. Frequency range (ω^*) with high spatial coherence (kHz) of base flow.

	$M_\infty = 2$	$M_\infty = 3.5$	$M_\infty = 5$
$r_1 = 0.038$ mm	10 ~ 100	50 ~ 440	50 ~ 440
$r_7 = 3.967$ mm	15 ~ 90	10 ~ 140	10 ~ 180
$r_{10} = 38.1$ mm	10 ~ 55	10 ~ 65	10 ~ 100

(x_c) of plasma actuator model of cone flows is chosen as the peak value of the growth rates distribution in the streamwise directions. Increased nose radii lowers the relative temperature difference between the actuated and base flow-fields. The values of relative temperature difference are higher at higher freestream Mach number based on the current results. We find that plasma actuation stabilizes the flow-field and spatial coherence becomes smaller. The frequency range with high spatial coherence of typical nose radii are shown in Table 5-3. The frequency range with higher spatial coherence of each nose radii decreased by around 10 ~ 40% for actuated flow compared with base flow except for r_1 at M_∞ . On the other hand, for r_1 at M_∞ , the value of separation distance with high spatial coherence of actuated flow is around 30% ~ 50% of base flow.

Table 5-3. Frequency range (ω^*) with high spatial coherence (kHz) of actuated flow.

	$M_\infty = 2$	$M_\infty = 3.5$	$M_\infty = 5$
$r_1 = 0.038$ mm	5 ~ 50	10 ~ 270	10 ~ 440
$r_7 = 3.967$ mm	5 ~ 50	10 ~ 55	5 ~ 50
$r_{10} = 38.1$ mm	10 ~ 50	5 ~ 50	10 ~ 60

The results of this dissertation demonstrate the effects of leading edge radii on the growth rate distributions and spatial coherence, which is beneficial to understand the characteristics of the driving force causing the vibration during rocket ascent. These results can be used to choose an appropriate nose radius when combined with structural analysis to minimize unsteady loading in the region leading to transition. In addition, the flow-field variation with plasma actuation can be used to understand the mechanism of temperature effects on stability and transition.

5.2 Future Work

5.2.1 Jet Flows

For jet noise prediction, we applied the instability wave method to predict the pressure perturbation signal at the upstream and sideline directions. The results show the high correlation between the signal at the upstream and downstream direction. Therefore, the effects of instability waves as a stimulus signal to the plasma actuator control to destroy the coherent structures can be measured in the upstream direction as we proposed. In the future, we plan to further study the modification of the SPL and correlation of noise source by adding the plasma actuation. Additionally, the POD method has been used to extract the most energetic part of flow-fields and compared with the results of instability waves. However, the POD modes used to reconstruct the pressure perturbations history need to be further investigated. In the future, we will try to find the POD modes via the results of correlation between POD modes and the radiation part of the Lighthill noise source [71] and predict the jet noise from the flow-fields reconstructed from the selected POD modes.

Kirchhoff surface method is an acoustic analogy method, however, there is an over-prediction at lower frequency and smaller cut-off frequency. The method can be used to predict the jet noise from the POD modes, which has been applied and discussed in the previous investigation. In the future, we will try to resolve this over-prediction and increase the cut-off frequency. In addition, the far-field noise from POD modes via this method will be computed and discussed.

5.2.2 Boundary Layer Flows

The pressure fluctuations from instability waves at the cone surface are constructed via linear superposition over the frequency range and the effects of amplitude of instability waves are not considered. In fact, in order to obtain the accurate excitation within vibro-acoustic problems, the amplitudes is an important factor. However, the amplitudes of instability waves require the pressure fluctuations from experimental measurements and/or high-fidelity numerical simulation [98, 49]. Additionally, in order to calibrate the amplitudes of instability waves, the methods to

extract the coherent structures are required, such as the POD method as shown in Section 2.1.2.2. In the future, we will consider the effects of amplitudes of instability waves. The calibration process will be based on the least-square sense as shown in Section 2.1.2.1.

The mean flow-field variables to obtain the instability wave solutions are from laminar flow in this dissertation. In the future, the mean flow-field variables from turbulent flows will be applied and studied. The work from Sharma and McKeon [58] is based on an analysis of the Navier-Stokes equations under an assumption of a turbulent mean profile for a pipe flow, where the velocity fluctuation is expressed as a sum of harmonic, radially varying travelling waves. The results show that the complex coherent structures can be created from minimum superpositions of response modes. In addition, hairpins and modulated hairpin packets are predicted by simple combinations of response modes.

The frequency range with high spatial coherence decreases with plasma actuation, which shows the possibility that the plasma actuation can alter the excitation of vibro-acoustic problems. However, the position (y_c) of the plasma actuation is the same as the previous investigations. In the future, we plan to change the positions of the plasma actuator model, especially y_c , based on the results of experimental measurements related to plasma actuators.

REFERENCES

- [1] Kundu, P. K., Cohen, I. M., and Dowling, D. R., *Fluid Mechanics*, Academic Press, 2016.
- [2] Ryu, J., “Study of High-Speed Turbulent Jet Noise Using Decomposition Methods,” Ph.D. thesis, Stanford University, 2010.
- [3] Delville, J., Ukeiley, L., Cordier, L., Bonnet, J. P., and Glauser, M., “Examination of Large-Scale Structures in a Turbulent Plane Mixing Layer. Part 1. Proper Orthogonal Decomposition,” *Journal of Fluid Mechanics*, Vol. 391, 1999, pp. 91–122. doi:[10.1017/s0022112099005200](https://doi.org/10.1017/s0022112099005200).
- [4] Gudmundsson, K., and Colonius, T., “Parabolized Stability Equation Models for Turbulent Jets and Their Radiated Sound,” *15th AIAA/CEAS Aeroacoustics Conference (30th AIAA Aeroacoustics Conference)*, AIAA Paper No. 2009-3380, 2009. doi:[10.2514/6.2009-3380](https://doi.org/10.2514/6.2009-3380).
- [5] Huff, D. L., “NASA Glenn’s Contribution to Aircraft Engine Noise Research,” NASA TP-2013-217818, Jun 2014.
- [6] Morrell, S., Taylor, R., and Lyle, D., “A Review of Health Effects of Aircraft Noise,” *Australian and New Zealand Journal of Public Health*, Vol. 21, No. 2, 1997, pp. 221–236. doi:[10.1111/j.1467-842x.1997.tb01690.x](https://doi.org/10.1111/j.1467-842x.1997.tb01690.x).
- [7] Bjorn, V. S., Albery, C. B., and McKinley, R. L., “U.S. Navy Flight Deck Hearing Protection Use Trends: Survey Results,” OMB No. 0704-0188, Apr 2005.
- [8] Morris, P., “Reduction of Advanced Military Aircraft Noise,” SERDP, WP-1583, Feb 2012.
- [9] Kailasanath, K., “Mechanical Chevrons and Fluidics for Advanced Military Aircraft Noise Reduction,” SERDP, WP-1584, Feb 2012.
- [10] Miller, S. A. E., “Flow Control of Large-Scale Coherent Turbulence to Reduce Jet Noise,” SERDP, WP19-1014, Dec 2020.
- [11] Lighthill, M. J., “On Sound Generated Aerodynamically I. General Theory,” *Proceedings of the Royal Society of London. Series A. Mathematical and Physical Sciences*, Vol. 211, No. 1107, 1952, pp. 564–587. doi:[10.1098/rspa.1952.0060](https://doi.org/10.1098/rspa.1952.0060).
- [12] Lighthill, M. J., “On Sound Generated Aerodynamically II. Turbulence as a Source of Sound,” *Proceedings of the Royal Society of London. Series A. Mathematical and Physical Sciences*, Vol. 222, No. 1148, 1954, pp. 1–32. doi:[10.1098/rspa.1954.0049](https://doi.org/10.1098/rspa.1954.0049).
- [13] Tam, C. K. W., “Jet Noise Generated by Large-Scale Coherent Motion,” *Aeroacoustics of Flight Vehicles: Theory and Practice. Volume 1: Noise Sources*, Vol. 1, 1991, pp. 311–390.
- [14] Ffowcs-Williams, J. E., and Hawkings, D. L., “Sound Generation by Turbulence and Surfaces in Arbitrary Motion,” *Philosophical Transactions of the Royal Society of London. Series A, Mathematical and Physical Sciences*, Vol. 264, No. 1151, 1969, pp. 321–342. doi:[10.1098/rsta.1969.0031](https://doi.org/10.1098/rsta.1969.0031).
- [15] Farassat, F., and Myers, M., “Extension of Kirchhoff’s Formula to Radiation from Moving Surfaces,” *Journal of Sound and Vibration*, Vol. 123, No. 3, 1988, pp. 451–460. doi:[10.1016/s0022-460x\(88\)80162-7](https://doi.org/10.1016/s0022-460x(88)80162-7).

- [16] Tam, C. K. W., and Burton, D. E., “Sound Generated by Instability Waves of Supersonic Flows. Part 1. Two-Dimensional Mixing Layers,” *Journal of Fluid Mechanics*, Vol. 138, No. 1, 1984, pp. 249–271. doi:[10.1017/s0022112084000112](https://doi.org/10.1017/s0022112084000112).
- [17] Tam, C. K. W., and Burton, D. E., “Sound Generated by Instability Waves of Supersonic Flows. Part 2. Axisymmetric Jets,” *Journal of Fluid Mechanics*, Vol. 138, No. 1, 1984, pp. 273–295. doi:[10.1017/s0022112084000124](https://doi.org/10.1017/s0022112084000124).
- [18] Tam, C. K. W., and Chen, P., “Turbulent Mixing Noise from Supersonic Jets,” *AIAA Journal*, Vol. 32, No. 9, 1994, pp. 1774–1780. doi:[10.2514/3.12173](https://doi.org/10.2514/3.12173).
- [19] Tam, C. K. W., “Supersonic Jet Noise,” *Annual Review of Fluid Mechanics*, Vol. 27, No. 1, 1995, pp. 17–43. doi:[10.1146/annurev.fl.27.010195.000313](https://doi.org/10.1146/annurev.fl.27.010195.000313).
- [20] Tam, C. K. W., Golebiowski, M., and Seiner, J., “On the Two Components of Turbulent Mixing Noise from Supersonic Jets,” *Aeroacoustics Conference*, AIAA Paper No. 1996-1716, 1996. doi:[10.2514/6.1996-1716](https://doi.org/10.2514/6.1996-1716).
- [21] Tam, C. K. W., “Directional Acoustic Radiation from a Supersonic Jet Generated by Shear Layer Instability,” *Journal of Fluid Mechanics*, Vol. 46, No. 4, 1971, pp. 757–768. doi:[10.1017/s0022112071000831](https://doi.org/10.1017/s0022112071000831).
- [22] Tam, C. K. W., Chen, P., and Seiner, J. M., “Relationship between the Instability Waves and Noise of High-Speed Jets,” *AIAA Journal*, Vol. 30, No. 7, 1992, pp. 1747–1752. doi:[10.2514/3.11132](https://doi.org/10.2514/3.11132).
- [23] Kopiev, V., Chernyshev, S., Zaitsev, M., and Kuznetsov, V., “Experimental Validation of Instability Wave Theory for Round Supersonic Jet,” *12th AIAA/CEAS Aeroacoustics Conference (27th AIAA Aeroacoustics Conference)*, AIAA Paper No. 2006-2595, 2006. doi:[10.2514/6.2006-2595](https://doi.org/10.2514/6.2006-2595).
- [24] Tam, C. K. W., and Morris, P. J., “The Radiation of Sound by the Instability Waves of a Compressible Plane Turbulent Shear Layer,” *Journal of Fluid Mechanics*, Vol. 98, No. 2, 1980, pp. 349–381. doi:[10.1017/s0022112080000195](https://doi.org/10.1017/s0022112080000195).
- [25] Uzun, A., Alvi, F. S., Colonius, T., and Hussaini, M. Y., “Spatial Stability Analysis of Subsonic Jets Modified for Low-Frequency Noise Reduction,” *AIAA Journal*, Vol. 53, No. 8, 2015, pp. 2335–2358. doi:[10.2514/1.J053719](https://doi.org/10.2514/1.J053719).
- [26] Henderson, B., “Fifty Years of Fluidic Injection for Jet Noise Reduction,” *International Journal of Aeroacoustics*, Vol. 9, No. 1-2, 2010, pp. 91–122. doi:[10.1260/1475-472x.9.1-2.91](https://doi.org/10.1260/1475-472x.9.1-2.91).
- [27] Prasad, C., and Morris, P., “Effect of Fluid Injection on Turbulence and Noise Reduction of a Supersonic Jet,” *Philosophical Transactions of the Royal Society A: Mathematical, Physical and Engineering Sciences*, Vol. 377, No. 2159, 2019. doi:[10.1098/rsta.2019.0082](https://doi.org/10.1098/rsta.2019.0082).
- [28] Muller, R. R., “Me 262, Volume One (Revised Edition),” *Global War Studies*, Vol. 9, No. 1, 2012, pp. 112–113.

- [29] Caiazzo, A., D’Amico, R., and Desmet, W., “Use of a Generalized Corcos Model to Predict Flow-Induced Noise in a Cavity-plate System,” *Proceedings of the 27th International Conference on Noise and Vibration Engineering, ISMA2016 & USD2016*, 2016, pp. 1319–1332.
- [30] Lubert, C. P., “Sixty Years of Launch Vehicle Acoustics,” *Acoustical Society of America*, 2017, p. 040004. doi:[10.1121/2.0000704](https://doi.org/10.1121/2.0000704).
- [31] Marchetto, C., Maxit, L., Robin, O., and Berry, A., “Experimental Prediction of the Vibration Response of Panels under a Turbulent Boundary Layer Excitation from Sensitivity Functions,” *The Journal of the Acoustical Society of America*, Vol. 143, No. 5, 2018, pp. 2954–2964. doi:[10.1121/1.5037362](https://doi.org/10.1121/1.5037362).
- [32] Fahy, F. J., “Statistical Energy Analysis: a Critical Overview,” *Philosophical Transactions of the Royal Society of London. Series A: Physical and Engineering Sciences*, Vol. 346, No. 1681, 1994, pp. 431–447. doi:[10.1098/rsta.1994.0027](https://doi.org/10.1098/rsta.1994.0027).
- [33] Langenecker, B., “Effect of Sonic and Ultrasonic Radiation on Safety Factors of Rockets and Missiles,” *AIAA Journal*, Vol. 1, No. 1, 1963, pp. 80–83. doi:[10.2514/3.1474](https://doi.org/10.2514/3.1474).
- [34] da Rocha, J. L. T., “Coupled Structural-Acoustic Analytical Models for the Prediction of Turbulent Boundary-Layer-Induced Noise in Aircraft Cabins,” Ph.D. thesis, University of Victoria, 2010.
- [35] Chase, D., “Modeling the Wavevector-Frequency Spectrum of Turbulent Boundary Layer Wall Pressure,” *Journal of Sound and Vibration*, Vol. 70, No. 1, 1980, pp. 29–67. doi:[10.1016/0022-460x\(80\)90553-2](https://doi.org/10.1016/0022-460x(80)90553-2).
- [36] Ffowcs-Williams, J. E., “Boundary-Layer Pressures and the Corcos Model: a Development to Incorporate Low-Wavenumber Constraints,” *Journal of Fluid Mechanics*, Vol. 125, No. -1, 1982, p. 9. doi:[10.1017/s0022112082003218](https://doi.org/10.1017/s0022112082003218).
- [37] Corcos, G. M., “The Structure of the Turbulent Pressure Field in Boundary-Layer Flows,” *Journal of Fluid Mechanics*, Vol. 18, No. 03, 1964, pp. 353–378. doi:[10.1017/s002211206400026x](https://doi.org/10.1017/s002211206400026x).
- [38] Efimtsov, B., “Characteristics of the Field of Turbulent Wall Pressure-Fluctuations at Large Reynolds-Numbers,” *Soviet Physics Acoustics-USSR*, Vol. 28, No. 4, 1982, pp. 289–292.
- [39] Lee, C., and Jiang, X., “Flow Structures in Transitional and Turbulent Boundary Layers,” *Physics of Fluids*, Vol. 31, No. 11, 2019, p. 111301. doi:[10.1063/1.5121810](https://doi.org/10.1063/1.5121810).
- [40] Robinson, S. K., “Coherent Motions in the Turbulent Boundary Layer,” *Annual Review of Fluid Mechanics*, Vol. 23, No. 1, 1991, pp. 601–639. doi:[10.1146/annurev.fl.23.010191.003125](https://doi.org/10.1146/annurev.fl.23.010191.003125).
- [41] Marusic, I., “On the Role of Large-Scale Structures in Wall Turbulence,” *Physics of Fluids*, Vol. 13, No. 3, 2001, pp. 735–743. doi:[10.1063/1.1343480](https://doi.org/10.1063/1.1343480).

- [42] Morrison, G., and McLaughlin, D., “Noise Generation by Instabilities in Low Reynolds Number Supersonic Jets,” *Journal of Sound and Vibration*, Vol. 65, No. 2, 1979, pp. 177–191. doi:[10.1016/0022-460x\(79\)90512-1](https://doi.org/10.1016/0022-460x(79)90512-1).
- [43] Tam, C. K. W., and Hu, F. Q., “On the Three Families of Instability Waves of High-speed Jets,” *Journal of Fluid Mechanics*, Vol. 201, No. 1, 1989, p. 447. doi:[10.1017/s002211208900100x](https://doi.org/10.1017/s002211208900100x).
- [44] Malik, M., “Numerical Methods for Hypersonic Boundary Layer Stability,” *Journal of Computational Physics*, Vol. 86, No. 2, 1990, pp. 376–413. doi:[10.1016/0021-9991\(90\)90106-b](https://doi.org/10.1016/0021-9991(90)90106-b).
- [45] Malik, M. R., and Spall, R. E., “On the Stability of Compressible Flow Past Axisymmetric Bodies,” *Journal of Fluid Mechanics Digital Archive*, Vol. 228, 1991, pp. 443–463. doi:[10.1017/s002211209100277x](https://doi.org/10.1017/s002211209100277x).
- [46] Knisely, C. P., and Zhong, X., “Sound Radiation by Supersonic Unstable Modes in Hypersonic Blunt Cone Boundary Layers. I. Linear Stability Theory,” *Physics of Fluids*, Vol. 31, No. 2, 2019, p. 024103. doi:[10.1063/1.5055761](https://doi.org/10.1063/1.5055761).
- [47] Laible, A., Mayer, C., and Fasel, H., “Numerical Investigation of Supersonic Transition for a Circular Cone at Mach 3.5,” *38th Fluid Dynamics Conference and Exhibit*, AIAA Paper No. 2008-4397, 2008. doi:[10.2514/6.2008-4397](https://doi.org/10.2514/6.2008-4397).
- [48] Gross, A., and Fasel, H. F., “Numerical Investigation of Supersonic Flow for Axisymmetric Cones,” *Mathematics and Computers in Simulation*, Vol. 81, No. 1, 2010, pp. 133–142. doi:[10.1016/j.matcom.2010.07.018](https://doi.org/10.1016/j.matcom.2010.07.018).
- [49] Ryu, J., and Lele, S. K., “Instability Waves in High-Speed Jets: Near- and Far-Field DNS/LES Data Analysis,” *International Journal of Aeroacoustics*, Vol. 14, No. 3-4, 2015, pp. 643–673. doi:[10.1260/1475-472x.14.3-4.643](https://doi.org/10.1260/1475-472x.14.3-4.643).
- [50] Tam, C. K. W., Viswanathan, K., Ahuja, K. K., and Panda, J., “The Sources of Jet Noise: Experimental Evidence,” *Journal of Fluid Mechanics*, Vol. 615, 2008, pp. 253—292. doi:[10.1017/S0022112008003704](https://doi.org/10.1017/S0022112008003704).
- [51] Swift, S. H., Gee, K. L., Neilsen, T. B., Wall, A. T., Downing, J. M., and James, M. M., “Spatiotemporal-Correlation Analysis of Jet Noise from a Round Nozzle High-Performance Aircraft,” *2018 AIAA/CEAS Aeroacoustics Conference*, AIAA Paper No. 2018-3938, 2018. doi:[10.2514/6.2018-3938](https://doi.org/10.2514/6.2018-3938).
- [52] Fiedler, H., “Coherent Structures in Turbulent Flows,” *Progress in Aerospace Sciences*, Vol. 25, No. 3, 1988, pp. 231–269. doi:[10.1016/0376-0421\(88\)90001-2](https://doi.org/10.1016/0376-0421(88)90001-2).
- [53] Premnath, R., “Qualitative Air Flow Modelling and Analysis of Data Centre Air Conditioning as Multiple Jet Array,” Ph.D. thesis, Cochin University of Science and Technology, Nov 2011.

- [54] Gudmundsson, K., “Instability Wave Models of Turbulent Jets from Round and Serrated Nozzles,” Ph.D. thesis, California Institute of Technology, Jan 2010.
- [55] Mayer, C. S. J., “Numerical Investigation of the Nonlinear Transition Regime in Supersonic Boundary Layer,” Ph.D. thesis, The University of Arizona, Nov 2009.
- [56] Cengel, Y. A., and Cimbala, J. M., *Fluid Mechanics: Fundamentals and Applications*, McGraw-Hill Companies, Inc., 2014.
- [57] Hussain, A. K. M. F., “Coherent Structures and Turbulence,” *Journal of Fluid Mechanics*, Vol. 173, 1986, pp. 303–356. doi:[10.1017/s0022112086001192](https://doi.org/10.1017/s0022112086001192).
- [58] Sharma, A. S., and McKeon, B. J., “On Coherent Structure in Wall Turbulence,” *Journal of Fluid Mechanics*, Vol. 728, 2013, pp. 196–238. doi:[10.1017/jfm.2013.286](https://doi.org/10.1017/jfm.2013.286).
- [59] Harker, B. M., Neilsen, T. B., Gee, K. L., Wall, A. T., and James, M. M., “Spatiotemporal-Correlation Analysis of Jet Noise from a High-Performance Military Aircraft,” *AIAA Journal*, Vol. 54, No. 5, 2016, pp. 1554–1566. doi:[10.2514/1.j054442](https://doi.org/10.2514/1.j054442).
- [60] Miller, S. A. E., “Toward a Comprehensive Model of Jet Noise Using an Acoustic Analogy,” *AIAA Journal*, Vol. 52, No. 10, 2014, pp. 2143–2164. doi:[10.2514/1.j052809](https://doi.org/10.2514/1.j052809).
- [61] Liu, J., “On Eddy-Mach Wave Radiation Source Mechanism in the Jet Noise Problem,” *9th Aerospace Sciences Meeting*, AIAA Paper No. 1971-150, 1971. doi:[10.2514/6.1971-150](https://doi.org/10.2514/6.1971-150).
- [62] Edgington-Mitchell, D., “Aeroacoustic Resonance and Self-Excitation in Screeching and Impinging Supersonic Jets – A Review,” *International Journal of Aeroacoustics*, Vol. 18, No. 2-3, 2019, pp. 118–188. doi:[10.1177/1475472x19834521](https://doi.org/10.1177/1475472x19834521).
- [63] Powell, A., “On the Mechanism of Choked Jet Noise,” *Proceedings of the Physical Society. Section B*, Vol. 66, No. 12, 1953, pp. 1039–1056. doi:[10.1088/0370-1301/66/12/306](https://doi.org/10.1088/0370-1301/66/12/306).
- [64] Powell, A., Umeda, Y., and Ishii, R., “Observations of the Oscillation Modes of Choked Circular Jets,” *The Journal of the Acoustical Society of America*, Vol. 92, No. 5, 1992, pp. 2823–2836. doi:[10.1121/1.404398](https://doi.org/10.1121/1.404398).
- [65] Norum, T. D., “Screech Suppression in Supersonic Jets,” *AIAA Journal*, Vol. 21, No. 2, 1983, pp. 235–240. doi:[10.2514/3.8059](https://doi.org/10.2514/3.8059).
- [66] Tam, C. K. W., and Tanna, H. K., “Shock Associated Noise of Supersonic Jets from Convergent-Divergent Nozzles,” *Journal of Sound and Vibration*, Vol. 81, No. 3, 1982, pp. 337–358. doi:[10.1016/0022-460x\(82\)90244-9](https://doi.org/10.1016/0022-460x(82)90244-9).
- [67] Ffowcs-Williams, J. E., “Aeroacoustics,” *Annual Review of Fluid Mechanics*, Vol. 9, No. 1, 1977, pp. 447–468.
- [68] Bodony, D. J., and Lele, S. K., “Current Status of Jet Noise Predictions Using Large-Eddy Simulation,” *AIAA Journal*, Vol. 46, No. 2, 2008, pp. 364–380. doi:[10.2514/1.24475](https://doi.org/10.2514/1.24475).

- [69] Jordan, P., and Colonius, T., “Wave Packets and Turbulent Jet Noise,” *Annual Review of Fluid Mechanics*, Vol. 45, No. 1, 2013, pp. 173–195.
doi:[10.1146/annurev-fluid-011212-140756](https://doi.org/10.1146/annurev-fluid-011212-140756).
- [70] Mankbadi, R., and Liu, J. T. C., “Sound Generated Aerodynamically Revisited: Large-Scale Structures in a Turbulent Jet as a Source of Sound,” *Philosophical Transactions of the Royal Society of London. Series A, Mathematical and Physical Sciences*, Vol. 311, No. 1516, 1984, pp. 183–217. doi:[10.1098/rsta.1984.0024](https://doi.org/10.1098/rsta.1984.0024).
- [71] Freund, J., and Colonius, T., “Turbulence and Sound-Field POD Analysis of a Turbulent Jet,” *International Journal of Aeroacoustics*, Vol. 8, No. 4, 2009, pp. 337–354.
- [72] Ffowcs-Williams, J. E., “The Noise from Turbulence Convected at High Speed,” *Philosophical Transactions of the Royal Society A: Mathematical, Physical and Engineering Sciences*, Vol. 255, No. 1061, 1963, pp. 469–503. doi:[10.1098/rsta.1963.0010](https://doi.org/10.1098/rsta.1963.0010).
- [73] Farassat, F., “Derivation of Formulations 1 and 1A of Farassat,” 2007.
NASA/TM-2007-214853.
- [74] di Francescantonio, P., “A New Boundary Integral Formulation for the Prediction of Sound Radiation,” *Journal of Sound and Vibration*, Vol. 202, No. 4, 1997, pp. 491–509.
doi:[10.1006/jsvi.1996.0843](https://doi.org/10.1006/jsvi.1996.0843).
- [75] Brentner, K. S., and Farassat, F., “Analytical Comparison of the Acoustic Analogy and Kirchhoff Formulation for Moving Surfaces,” *AIAA Journal*, Vol. 36, No. 8, 1998, pp. 1379–1386. doi:[10.2514/2.558](https://doi.org/10.2514/2.558).
- [76] Lilley, G. M., “On the Noise from Jets, Noise Mechanism,” *Annual Review of Fluid Mechanics*, Vol. 131, No. 345, 1974, pp. 13.1–13.12.
- [77] Goldstein, M. E., “Aeroacoustics of Turbulent Shear Flows,” *Annual Review of Fluid Mechanics*, Vol. 16, No. 1, 1984, pp. 263–285. doi:[10.1146/annurev.fl.16.010184.001403](https://doi.org/10.1146/annurev.fl.16.010184.001403).
- [78] Goldstein, M. E., “A Generalized Acoustic Analogy,” *Journal of Fluid Mechanics*, Vol. 488, 2003, pp. 315–333. doi:[10.1017/s0022112003004890](https://doi.org/10.1017/s0022112003004890).
- [79] Balachandar, S., and Eaton, J. K., “Turbulent Dispersed Multiphase Flow,” *Annual Review of Fluid Mechanics*, Vol. 42, No. 1, 2010, pp. 111–133.
doi:[10.1146/annurev.fluid.010908.165243](https://doi.org/10.1146/annurev.fluid.010908.165243).
- [80] Cheung, L., Bodony, D., and Lele, S., “Noise Radiation Predictions from Jet Instability Waves Using a Hybrid Nonlinear PSE-Acoustic Analogy Approach,” *13th AIAA/CEAS Aeroacoustics Conference (28th AIAA Aeroacoustics Conference)*, AIAA Paper No. 2007-3638, 2007. doi:[10.2514/6.2007-3638](https://doi.org/10.2514/6.2007-3638).
- [81] Yang, H., Zhou, L., Zhang, X., Wan, Z., and Sun, D., “Nonlinear Interaction of Instability Waves and Vortex-Pairing Noise in Axisymmetric Subsonic Jets,” *Fluid Dynamics Research*, Vol. 48, No. 5, 2016, p. 055502. doi:[10.1088/0169-5983/48/5/055502](https://doi.org/10.1088/0169-5983/48/5/055502).

- [82] Suzuki, T., and Colonius, T., “Instability Waves in a Subsonic Round Jet Detected Using a Near-Field Phased Microphone Array,” *Journal of Fluid Mechanics*, Vol. 565, 2006, pp. 197–226. doi:[10.1017/S0022112006001613](https://doi.org/10.1017/S0022112006001613).
- [83] Mankbadi, R., and Liu, J. T. C., “A study of the Interactions between Large-Scale Coherent Structures and Fine-Grained Turbulence in a Round Jet,” *Philosophical Transactions of the Royal Society of London. Series A, Mathematical and Physical Sciences*, Vol. 298, No. 1443, 1981, pp. 541–602. doi:[10.1098/rsta.1981.0001](https://doi.org/10.1098/rsta.1981.0001).
- [84] McLaughlin, D. K., Morrison, G. L., and Troutt, T. R., “Experiments on the Instability Waves in a Supersonic Jet and Their Acoustic Radiation,” *Journal of Fluid Mechanics*, Vol. 69, No. 1, 1975, pp. 73–95. doi:[10.1017/s0022112075001322](https://doi.org/10.1017/s0022112075001322).
- [85] Troutt, T. R., and McLaughlin, D. K., “Experiments on the Flow and Acoustic Properties of a Moderate-Reynolds-Number Supersonic Jet,” *Journal of Fluid Mechanics*, Vol. 116, 1982, pp. 123–156. doi:[10.1017/s0022112082000408](https://doi.org/10.1017/s0022112082000408).
- [86] Oertel, H., “Mach Wave Radiation of Hot Supersonic Jets Investigated by Means of the Shock Tube and New Optical Techniques,” *Proc. of the 12th Intl Symp. on Shock Tubes and Waves, Jerusalem*, 1980, pp. 266–275.
- [87] Crighton, D. G., and Gaster, M., “Stability of Slowly Diverging Jet Flow,” *Journal of Fluid Mechanics*, Vol. 77, No. 2, 1976, pp. 397–413. doi:[10.1017/s0022112076002176](https://doi.org/10.1017/s0022112076002176).
- [88] Kay, E., Agarwal, A., and Cavalieri, A. V., “The Effect of Base-Flow Changes on Kelvin-Helmholtz Instability and Noise Radiation in Jets,” *20th AIAA/CEAS Aeroacoustics Conference*, AIAA Paper No. 2014-2605, 2014. doi:[10.2514/6.2014-2605](https://doi.org/10.2514/6.2014-2605).
- [89] Mohseni, K., “A Universality in Vortex Formation. B. Evaluation of Mach Wave Radiation in a Supersonic Jet,” Ph.D. thesis, California Institute of Technology, Nov 2000.
- [90] Herbert, T. H., “Boundary Layer Transition - Analysis and Prediction Revisited,” *29th Aerospace Sciences Meeting*, AIAA Paper No. 1991-737, 1991. doi:[10.2514/6.1991-737](https://doi.org/10.2514/6.1991-737).
- [91] Herbert, T., “Parabolized Stability Equations,” *Annual Review of Fluid Mechanics*, Vol. 29, No. 1, 1997, pp. 245–283. doi:[10.1146/annurev.fluid.29.1.245](https://doi.org/10.1146/annurev.fluid.29.1.245).
- [92] Malik, M. R., and Chang, C. L., “Nonparallel and Nonlinear Stability of Supersonic Jet Flow,” *Computers & Fluids*, Vol. 29, No. 3, 2000, pp. 327–365. doi:[10.1016/s0045-7930\(99\)00013-4](https://doi.org/10.1016/s0045-7930(99)00013-4).
- [93] Piot, E., Casalis, G., Muller, F., and Bailly, C., “Investigation of the PSE Approach for Subsonic and Supersonic Hot Jets. Detailed Comparisons with LES and Linearized Euler Equations Results,” *International Journal of Aeroacoustics*, Vol. 5, No. 4, 2006, pp. 361–393. doi:[10.1260/147547206779379877](https://doi.org/10.1260/147547206779379877).
- [94] Ryu, J., Lele, S., and Viswanathan, K., “Identification of Instability Waves in High-Speed Turbulent Jets,” *13th AIAA/CEAS Aeroacoustics Conference (28th AIAA Aeroacoustics Conference)*, AIAA Paper No. 2007-3624, 2007. doi:[10.2514/6.2007-3624](https://doi.org/10.2514/6.2007-3624).

- [95] Suzuki, T., and Colonius, T., “Identification of Jet Instability Waves and Design of a Microphone Array,” *10th AIAA/CEAS Aeroacoustics Conference*, AIAA Paper No. 2004-2960, 2004. doi:[10.2514/6.2004-2960](https://doi.org/10.2514/6.2004-2960).
- [96] Nair, U. S., Goparaju, K., and Gaitonde, D., “Energy Dynamics Resulting in Turbulent and Acoustic Phenomena in an Underexpanded Jet,” *Aerospace*, Vol. 5, No. 2, 2018. doi:[10.3390/aerospace5020049](https://doi.org/10.3390/aerospace5020049).
- [97] Grizzi, S., and Camussi, R., “Wavelet Analysis of Near-Field Pressure Fluctuations Generated by a Subsonic Jet,” *Journal of Fluid Mechanics*, Vol. 698, 2012, pp. 93–124. doi:[10.1017/jfm.2012.64](https://doi.org/10.1017/jfm.2012.64).
- [98] Sinha, A., Rodríguez, D., Brès, G. A., and Colonius, T., “Wavepacket Models for Supersonic Jet Noise,” *Journal of Fluid Mechanics*, Vol. 742, 2014, pp. 71–95. doi:[10.1017/jfm.2013.660](https://doi.org/10.1017/jfm.2013.660).
- [99] Dahl, M. D., “The Aeroacoustics of Supersonic Coaxial Jets,” Ph.D. thesis, The Pennsylvania State University, Dec 1994.
- [100] Tam, C. K. W., and Chen, K. C., “A Statistical Model of Turbulence in Two-dimensional Mixing Layers,” *Journal of Fluid Mechanics*, Vol. 92, No. 2, 1979, pp. 303–326. doi:[10.1017/S002211207900063X](https://doi.org/10.1017/S002211207900063X).
- [101] Papamoschou, D., “Prediction of Jet Noise Shielding,” *48th AIAA Aerospace Sciences Meeting Including the New Horizons Forum and Aerospace Exposition*, AIAA Paper No. 2010-653, 2010. doi:[10.2514/6.2010-653](https://doi.org/10.2514/6.2010-653).
- [102] Papamoschou, D., “Wavepacket Modeling of the Jet Noise Source,” *International Journal of Aeroacoustics*, Vol. 17, No. 1-2, 2018, pp. 52–69. doi:[10.1177/1475472X17743653](https://doi.org/10.1177/1475472X17743653).
- [103] Koenig, M., Cavalieri, A. V., Jordan, P., Delville, J., Gervais, Y., and Papamoschou, D., “Far-Field Filtering and Source Imaging of Subsonic Jet Noise,” *Journal of Sound and Vibration*, Vol. 332, No. 18, 2013, pp. 4067–4088. doi:[10.1016/j.jsv.2013.02.040](https://doi.org/10.1016/j.jsv.2013.02.040).
- [104] Reba, R., Narayanan, S., Colonius, T., and Suzuki, T., “Modeling Jet Noise from Organized Structures Using Near-Field Hydrodynamic Pressure,” *11th AIAA/CEAS Aeroacoustics Conference*, AIAA Paper No. 2005-3093, 2005. doi:[10.2514/6.2005-3093](https://doi.org/10.2514/6.2005-3093).
- [105] Reba, R., Simonich, J., and Schlinker, R., “Measurement of Source Wave-Packets in High-Speed Jets and Connection to Far-Field Sound,” *14th AIAA/CEAS Aeroacoustics Conference (29th AIAA Aeroacoustics Conference)*, AIAA Paper No. 2008-2891, 2008. doi:[10.2514/6.2008-2891](https://doi.org/10.2514/6.2008-2891).
- [106] Fedorov, A., and Tumin, A., “High-Speed Boundary-Layer Instability: Old Terminology and a New Framework,” *AIAA Journal*, Vol. 49, No. 8, 2011, pp. 1647–1657. doi:[10.2514/1.j050835](https://doi.org/10.2514/1.j050835).

- [107] Zhong, X., and Ma, Y., “Boundary-layer Receptivity of Mach 7.99 Flow over a Blunt Cone to Free-Stream Acoustic Waves,” *Journal of Fluid Mechanics*, Vol. 556, 2006, p. 55. doi:[10.1017/s0022112006009293](https://doi.org/10.1017/s0022112006009293).
- [108] Balakumar, P., and Malik, M. R., “Discrete Modes and Continuous Spectra in Supersonic Boundary Layers,” *Journal of Fluid Mechanics*, Vol. 239, No. -1, 1992, p. 631. doi:[10.1017/s0022112092004555](https://doi.org/10.1017/s0022112092004555).
- [109] Malik, M. R., “Prediction and Control of Transition in Supersonic and Hypersonic Boundary Layers,” *AIAA Journal*, Vol. 27, No. 11, 1989, pp. 1487–1493. doi:[10.2514/3.10292](https://doi.org/10.2514/3.10292).
- [110] Esfahanian, V., “Computation and Stability Analysis of Laminar Flow over a Blunt Cone in Hypersonic Flow,” Ph.D. thesis, Ohio State University, 1991.
- [111] Lei, J., and Zhong, X., “Linear Stability Analysis of Nose Bluntness Effects on Hypersonic Boundary Layer Transition,” *Journal of Spacecraft and Rockets*, Vol. 49, No. 1, 2012, pp. 24–37. doi:[10.2514/1.52616](https://doi.org/10.2514/1.52616).
- [112] Schneider, S. P., “Flight Data for Boundary-Layer Transition at Hypersonic and Supersonic Speeds,” *Journal of Spacecraft and Rockets*, Vol. 36, No. 1, 1999, pp. 8–20. doi:[10.2514/2.3428](https://doi.org/10.2514/2.3428).
- [113] Rosenboom, I., Hein, S., and Dallmann, U., “Influence of Nose Bluntness on Boundary-Layer Instabilities in Hypersonic Cone Flows,” *30th Fluid Dynamics Conference*, AIAA Paper No. 1999-3591, 1999. doi:[10.2514/6.1999-3591](https://doi.org/10.2514/6.1999-3591).
- [114] Kufner, E., Dallmann, U., and Stilla, J., “Instability of Hypersonic Flow Past Blunt Cones - Effects of Mean Flow Variations,” *23rd Fluid Dynamics, Plasmadynamics, and Lasers Conference*, AIAA Paper No. 1993-2983, 1993. doi:[10.2514/6.1993-2983](https://doi.org/10.2514/6.1993-2983).
- [115] Masad, J., Nayfeh, A., and Al-Maaitah, A., “Effect of Heat Transfer on the Stability of Compressible Boundary Layers,” *Computers & Fluids*, Vol. 21, No. 1, 1992, pp. 43–61. doi:[10.1016/0045-7930\(92\)90032-q](https://doi.org/10.1016/0045-7930(92)90032-q).
- [116] Masad, J. A., and Abid, R., “On Transition in Supersonic and Hypersonic Boundary Layers,” *International Journal of Engineering Science*, Vol. 33, No. 13, 1995, pp. 1893–1919. doi:[10.1016/0020-7225\(95\)00046-z](https://doi.org/10.1016/0020-7225(95)00046-z).
- [117] Sidorenko, A., Gromyko, Y., Bountin, D., Polivanov, P., and Maslov, A., “Effect of the Local Wall Cooling/Heating on the Hypersonic Boundary Layer Stability and Transition,” *Progress in Flight Physics – Volume 7*, EDP Sciences, 2015. doi:[10.1051/eucass/201507549](https://doi.org/10.1051/eucass/201507549).
- [118] Polivanov, P., Gromyko, Y., Sidorenko, A., Maslov, A., Keller, M., Groskopf, G., and Kloker, M., “Effects of Local Wall Heating and Cooling on Hypersonic Boundary-Layer Stability,” *Proceedings of the Summer Program*, Citeseer, 2011.

- [119] Bitter, N. P., and Shepherd, J. E., “Stability of Highly Cooled Hypervelocity Boundary Layers,” *Journal of Fluid Mechanics*, Vol. 778, 2015, pp. 586–620. doi:[10.1017/jfm.2015.358](https://doi.org/10.1017/jfm.2015.358).
- [120] Balakumar, P., and Chou, A., “Transition Prediction in Hypersonic Boundary Layers Using Receptivity and Freestream Spectra,” *AIAA Journal*, Vol. 56, No. 1, 2018, pp. 193–208. doi:[10.2514/1.j056040](https://doi.org/10.2514/1.j056040).
- [121] Steson, K., Thompson, E., Donaldson, J., and Siler, L., “Laminar Boundary Layer Stability Experiments on a Cone at Mach 8. III - Sharp Cone at Angle of Attack,” *23rd Aerospace Sciences Meeting*, AIAA Paper No. 1985-492, 1985. doi:[10.2514/6.1985-492](https://doi.org/10.2514/6.1985-492).
- [122] Rushton, G. H., and Stetson, K. F., “Shock Tunnel Investigation of Boundary-Layer Transition at M Equals 5.5,” *AIAA Journal*, Vol. 5, No. 5, 1967, pp. 899–906. doi:[10.2514/3.4098](https://doi.org/10.2514/3.4098).
- [123] Palumbo, D., “Determining Correlation and Coherence Lengths in Turbulent Boundary Layer Flight Data,” *Journal of Sound and Vibration*, Vol. 331, No. 16, 2012, pp. 3721–3737.
- [124] Graham, W., “A Comparison of Models for the Wavenumber Frequency Spectrum of Turbulent Boundary Layer Pressures,” *Journal of Sound and Vibration*, Vol. 206, No. 4, 1997, pp. 541–565. doi:[10.1006/jsvi.1997.1114](https://doi.org/10.1006/jsvi.1997.1114).
- [125] el Hak, M. G., “Modern Developments in Flow Control,” *Applied Mechanics Reviews*, Vol. 49, No. 7, 1996, pp. 365–379. doi:[10.1115/1.3101931](https://doi.org/10.1115/1.3101931).
- [126] Marchis, M. D., Milici, B., Sardina, G., and Napoli, E., “Interaction between Turbulent Structures and Particles in Roughened Channel,” *International Journal of Multiphase Flow*, Vol. 78, 2016, pp. 117–131. doi:[10.1016/j.ijmultiphaseflow.2015.09.011](https://doi.org/10.1016/j.ijmultiphaseflow.2015.09.011).
- [127] Wang, L., Luo, Z., Xia, Z., Liu, B., and Deng, X., “Review of Actuators for High Speed Active Flow Control,” *Science China Technological Sciences*, Vol. 55, No. 8, 2012, pp. 2225–2240. doi:[10.1007/s11431-012-4861-2](https://doi.org/10.1007/s11431-012-4861-2).
- [128] Visbal, M., and Gaitonde, D., “Control of Vortical Flows Using Simulated Plasma Actuators,” *44th AIAA Aerospace Sciences Meeting and Exhibit*, AIAA Paper No. 2006-505, 2006. doi:[10.2514/6.2006-505](https://doi.org/10.2514/6.2006-505).
- [129] Jousot, R., Lago, V., and Parris, J.-D., “Quantification of the Effect of Surface Heating on Shock Wave Modification by a Plasma Actuator in a Low-Density Supersonic Flow over a Flat Plate,” *Experiments in Fluids*, Vol. 56, No. 5, 2015. doi:[10.1007/s00348-015-1970-2](https://doi.org/10.1007/s00348-015-1970-2).
- [130] Leonov, S. B., Li, J., and Fu, S., “Review of Plasma-Based Methods for High-Speed Flow Control,” AIP, 2011. doi:[10.1063/1.3651958](https://doi.org/10.1063/1.3651958).
- [131] Bletzinger, P., Ganguly, B. N., Wie, D. V., and Garscadden, A., “Plasmas in High Speed Aerodynamics,” *Journal of Physics D: Applied Physics*, Vol. 38, No. 4, 2005, pp. R33–R57. doi:[10.1088/0022-3727/38/4/r01](https://doi.org/10.1088/0022-3727/38/4/r01).

- [132] Shang, J. S., Kimmel, R. L., Menart, J., and Surzhikov, S. T., "Hypersonic Flow Control Using Surface Plasma Actuator," *Journal of Propulsion and Power*, Vol. 24, No. 5, 2008, pp. 923–934. doi:[10.2514/1.24413](https://doi.org/10.2514/1.24413).
- [133] Shyy, W., Jayaraman, B., and Andersson, A., "Modeling of Glow Discharge-Induced Fluid Dynamics," *Journal of Applied Physics*, Vol. 92, No. 11, 2002, pp. 6434–6443. doi:[10.1063/1.1515103](https://doi.org/10.1063/1.1515103).
- [134] Ebrahimi, A., and Hajipour, M., "Flow Separation Control over an Airfoil Using Dual Excitation of DBD Plasma Actuators," *Aerospace Science and Technology*, Vol. 79, 2018, pp. 658–668. doi:[10.1016/j.ast.2018.06.019](https://doi.org/10.1016/j.ast.2018.06.019).
- [135] Babou, Y., Martin Nieto, E., and Fajardo Pena, P., "Simple Body Force Model for Dielectric Barrier Discharge Plasma Actuator," 2017. doi:[10.13009/EUCASS2017-122](https://doi.org/10.13009/EUCASS2017-122).
- [136] Corke, T. C., Cavalieri, D. A., and Matlis, E., "Boundary-Layer Instability on Sharp Cone at Mach 3.5 with Controlled Input," *AIAA Journal*, Vol. 40, No. 5, 2002, pp. 1015–1018. doi:[10.2514/2.1744](https://doi.org/10.2514/2.1744).
- [137] Poggie, J., "Plasma-Based Hypersonic Flow Control," *37th AIAA Plasmadynamics and Lasers Conference*, AIAA Paper No. 2006-3567, 2006. doi:[10.2514/6.2006-3567](https://doi.org/10.2514/6.2006-3567).
- [138] Poggie, J., "Plasma-Based Control of Shock-Wave / Boundary-Layer Interaction," *44th AIAA Aerospace Sciences Meeting and Exhibit*, AIAA Paper No. 2006-1007, 2006. doi:[10.2514/6.2006-1007](https://doi.org/10.2514/6.2006-1007).
- [139] Corke, T., Cavalieri, D., Corke, T., and Cavalieri, D., "Controlled Experiments on Instabilities and Transition to Turbulence in Supersonic Boundary Layers," *28th Fluid Dynamics Conference*, AIAA Paper No. 1997-1817, 1997. doi:[10.2514/6.1997-1817](https://doi.org/10.2514/6.1997-1817).
- [140] Bivolaru, D., and Kuo, S. P., "Aerodynamic Modification of Supersonic Flow Around Truncated Cone Using a Pulsed Electrical Discharges," *AIAA Journal*, Vol. 43, No. 7, 2005, pp. 1482–1489. doi:[10.2514/1.7361](https://doi.org/10.2514/1.7361).
- [141] Shang, J. S., "Solving Schemes for Computational Magneto-Aerodynamics," *Journal of Scientific Computing*, Vol. 25, No. 1, 2005, pp. 289–306. doi:[10.1007/s10915-004-4645-3](https://doi.org/10.1007/s10915-004-4645-3).
- [142] Riherd, P., Roy, S., and Visbal, M., "Numerical Investigation of Serpentine Plasma Actuators for Separation Control at Low Reynolds Number," *41st AIAA Fluid Dynamics Conference and Exhibit*, AIAA Paper No. 2011-3990, 2011. doi:[10.2514/6.2011-3990](https://doi.org/10.2514/6.2011-3990).
- [143] Post, M. L., and Corke, T. C., "Separation Control on High Angle of Attack Airfoil Using Plasma Actuators," *AIAA Journal*, Vol. 42, No. 11, 2004, pp. 2177–2184. doi:[10.2514/1.2929](https://doi.org/10.2514/1.2929).
- [144] Updike, G., Shang, J., and Gaitonde, D., "Hypersonic Separated Flow Control Using Magneto-Aerodynamic Interaction," *43rd AIAA Aerospace Sciences Meeting and Exhibit*, AIAA Paper No. 2005-164, 2005. doi:[10.2514/6.2005-164](https://doi.org/10.2514/6.2005-164).

- [145] Kosinov, A. D., Maslov, A. A., and Shevelkov, S. G., “Experiments on the Stability of Supersonic Laminar Boundary Layers,” *Journal of Fluid Mechanics*, Vol. 219, No. -1, 1990, p. 621. doi:[10.1017/s0022112090003111](https://doi.org/10.1017/s0022112090003111).
- [146] Morris, P. J., “The Instability of High Speed Jets,” *International Journal of Aeroacoustics*, Vol. 9, No. 1-2, 2010, pp. 1–50. doi:[10.1260/1475-472x.9.1-2.1](https://doi.org/10.1260/1475-472x.9.1-2.1).
- [147] Boyd, J. P., “Complex Coordinate Methods for Hydrodynamic Instabilities and Sturm-Liouville Eigenproblems with an Interior Singularity,” *Journal of Computational Physics*, Vol. 57, No. 3, 1985, pp. 454–471. doi:[10.1016/0021-9991\(85\)90190-1](https://doi.org/10.1016/0021-9991(85)90190-1).
- [148] Towne, A., Schmidt, O. T., and Colonius, T., “Spectral Proper Orthogonal Decomposition and Its Relationship to Dynamic Mode Decomposition and Resolvent Analysis,” *Journal of Fluid Mechanics*, Vol. 847, 2018, pp. 821–867. doi:[10.1017/jfm.2018.283](https://doi.org/10.1017/jfm.2018.283).
- [149] Citriniti, J. H., and George, W. K., “Reconstruction of the Global Velocity Field in the Axisymmetric Mixing Layer Utilizing the Proper Orthogonal Decomposition,” *Journal of Fluid Mechanics*, Vol. 418, 2000, p. 137–166. doi:[10.1017/S0022112000001087](https://doi.org/10.1017/S0022112000001087).
- [150] Arndt, R. E. A., Long, D. F., and Glauser, M. N., “The Proper Orthogonal Decomposition of Pressure Fluctuations Surrounding a Turbulent Jet,” *Journal of Fluid Mechanics*, Vol. 340, 1997, p. 1–33. doi:[10.1017/S0022112097005089](https://doi.org/10.1017/S0022112097005089).
- [151] Freund, J. B., “Noise Sources in a Low-Reynolds-Number Turbulent Jet at Mach 0.9,” *Journal of Fluid Mechanics*, Vol. 438, 2001, pp. 277–305. doi:[10.1017/s0022112001004414](https://doi.org/10.1017/s0022112001004414).
- [152] Shen, W., and Miller, S. A. E., “Validation of a High-Order Large Eddy Simulation Solver for Acoustic Prediction of Supersonic Jet Flow,” *Journal of Theoretical and Computational Acoustics*, 2020, p. 2050008. doi:[10.1142/s2591728519500233](https://doi.org/10.1142/s2591728519500233).
- [153] Bodony, D. J., “Aeroacoustic Prediction of Turbulent Free Shear Flows,” Ph.D. thesis, Stanford University, Dec 2005.
- [154] Williams, E. G., *Fourier Acoustics Sound Radiation and Near-Field Acoustical Holography*, Academic Press, 1991.
- [155] Hall, J. W., Pinier, J., Hall, A., and Glauser, M., “Two-Point Correlations of the Near and Far-Field Pressure in a Transonic Jet,” *Volume 2: Fora*, ASMEDC, 2006. doi:[10.1115/fedsm2006-98458](https://doi.org/10.1115/fedsm2006-98458).
- [156] Ahuja, K. K., Nance, D. K., and Carrigan, J., “On Coherence of Jet Noise,” *20th AIAA/CEAS Aeroacoustics Conference*, AIAA Paper No. 2014-2339, 2014. doi:[10.2514/6.2014-2339](https://doi.org/10.2514/6.2014-2339).
- [157] Zhou, H., “Coherent Structure Modeling and its Role in the Computation of Passive Quantity Transport in Turbulent Flows,” *JSME International Journal Series B*, Vol. 41, No. 1, 1998, pp. 137–144. doi:[10.1299/jsmeb.41.137](https://doi.org/10.1299/jsmeb.41.137).

- [158] Palacios, F., Economon, T. D., Aranake, A., Copeland, S. R., Lonkar, A. K., Lukaczyk, T. W., Manosalvas, D. E., Naik, K. R., Padron, S., Tracey, B., Variyar, A., and Alonso, J. J., “Stanford University Unstructured (SU2): Analysis and Design Technology for Turbulent Flows,” *52nd Aerospace Sciences Meeting*, AIAA Paper No. 2014-0243, 2014. doi:[10.2514/6.2014-0243](https://doi.org/10.2514/6.2014-0243).
- [159] Brown, C., and Bridges, J., “Small Hot Jet Acoustic Rig Validation,” NASA TM-2006-214234, Apr 2006.
- [160] Shen, W., “Modeling of Broadband Shock-Associated Noise in Supersonic Jets Using Large-eddy Simulation and Decomposition Methods,” Ph.D. thesis, University of Florida, 2020.
- [161] Georgiadis, N. J., Yoder, D. A., and Engblom, W. B., “Evaluation of Modified Two-Equation Turbulence Models for Jet Flow Predictions,” *AIAA Journal*, Vol. 44, No. 12, 2006, pp. 3107–3114. doi:[10.2514/1.22650](https://doi.org/10.2514/1.22650).
- [162] Cheng, J., Goldschmidt, J. D., Shen, W., Ukeiley, L., and Miller, S. A., “Two-point radiation statistics from large-scale turbulent structures within supersonic jets,” *International Journal of Aeroacoustics*, Vol. 20, No. 3-4, 2021, pp. 254–282. doi:[10.1177/1475472x211005413](https://doi.org/10.1177/1475472x211005413).
- [163] Michalke, A., “Survey on Jet Instability Theory,” *Progress in Aerospace Sciences*, Vol. 21, 1984, pp. 159–199. doi:[10.1016/0376-0421\(84\)90005-8](https://doi.org/10.1016/0376-0421(84)90005-8).
- [164] Brès, G., Nichols, J., Lele, S., and Ham, F., “Towards Best Practices for Jet Noise Predictions with Unstructured Large-Eddy Simulations,” *42nd AIAA Fluid Dynamics Conference and Exhibit*, AIAA Paper No. 2012-2965, 2012. doi:[10.2514/6.2012-2965](https://doi.org/10.2514/6.2012-2965).
- [165] Laible, A. C., “Numerical Investigation of Boundary-Layer Transition for Cones at Mach 3.5 and 6.0,” Ph.D. thesis, University of Arizona, 2011.
- [166] Mayer, C. S. J., “Numerical Investigation of the Nonlinear Transition Regime in Supersonic Boundary Layers,” Ph.D. thesis, University of Arizona, 2009.

BIOGRAPHICAL SKETCH

Jianhui Cheng was born in Yanjin, Henan, P. R. China. She entered Henan Polytechnical University in Jiaozuo, China, after graduating from high school in 2009. Jianhui obtained her Bachelor of Science degree majoring in Thermal Energy and Power Engineering at Henan Polytechnical University in June, 2013. In Sep 2013, she enrolled in the Master of Science program in mechanics at Xi'an Jiaotong University, Xi'an. In June 2016, Jianhui finished her master thesis focus on phase response curves of periodic bursting neurons and their applications under the supervision of Dr. Yong Xie. In the same year in August, Jianhui enrolled in the Master of Science program in Mechanical engineering and obtained the master degree in May, 2018. In August, she joined the Theoretical Fluid Dynamics and Turbulence Group and worked with Dr. Steven A. E. Miller to pursue her Ph.D. degree focusing on large-scale turbulent structure prediction, control, stability, high-speed flow, and transition. In August 2022, Jianhui finished her study and was awarded a Ph.D. degree in mechanical engineering by the University of Florida.